A Forward Model-Based Analysis of Cardiovascular System Identification Methods

by

Ramakrishna Mukkamala

Bachelor of Science in Engineering
Biomedical and Electrical Engineering
Duke University, 1993

Master of Science
Electrical Engineering and Computer Science
Massachusetts Institute of Technology, 1995

Submitted to the
Department of Electrical Engineering and Computer Science
in partial fulfillment of the requirements for the degree of

Doctor of Philosophy

at the

MASSACHUSETTS INSTITUTE OF TECHNOLOGY

June 2000

Author: _____
Department of Electrical Engineering and Computer Science
May 3, 2000

Certified by: _____
Richard J. Cohen
Whitaker Professor of Biomedical Engineering
Thesis Supervisor

Accepted by: _____
Arthur C. Smith
Chairman, Department Committee on Graduate Students

A Forward Model-Based Analysis of Cardiovascular System Identification Methods

by

Ramakrishna Mukkamala

Submitted to the Department of Electrical Engineering and Computer Science
on May 3, 2000, in partial fulfillment of the
requirements for the degree of
Doctor of Philosophy

Abstract

Cardiovascular system identification is a potentially powerful approach for intelligent patient monitoring of cardiovascular function. Rather than merely recording hemodynamic signals, the signals are mathematically analyzed so as to provide a dynamical characterization of the physiologic mechanisms responsible for generating them. The fundamental aim of this thesis is to develop and evaluate cardiovascular system identification methods based on a test bed of data generated from a forward model of the cardiovascular system whose dynamical properties are known.

To this end, we developed a computer model of the human cardiovascular system which includes a lumped parameter model of the heart and circulation and a model of the short-term cardiovascular regulatory system continuously disturbed by resting physiologic perturbations. The short-term regulatory system consists of arterial and cardiopulmonary baroreflex systems and a direct neural coupling mechanism between respiration and heart rate. The resting physiologic perturbations include respiratory activity and stochastic disturbances to total peripheral resistance (TPR) and heart rate representing, for example, autoregulation of local vascular beds and higher brain center activity. We demonstrated that this model emulates experimental data in terms of steady-state pulsatility, limiting static behavior, and low frequency hemodynamic variability.

We first evaluated the performance of a previously developed cardiovascular system identification method against the forward model. The method involves the analysis of fluctuations in heart rate, arterial blood pressure (ABP), and instantaneous lung volume in order to characterize quantitatively important physiologic mechanisms including, for example, the heart rate baroreflex. From this analysis, we inferred that the cardiovascular system identification results derived from experimental data are likely to reflect the actual system dynamics of underlying physiologic mechanisms. We then introduced novel identification methods for quantifying TPR baroreflex dynamics from only fluctuations in cardiac output and ABP and for monitoring steady-state changes in TPR from only the ABP waveform. We demonstrated the efficacy

of these identification methods with respect to forward model generated data and a preliminary set of experimental data. The results of this forward model-based analysis motivate the experimental validation of the cardiovascular system identification methods considered in this thesis.

Thesis Supervisor: Richard J. Cohen
Title: Whitaker Professor of Biomedical Engineering

Acknowledgments

I would like to start off by thanking my thesis advisor, Prof. Richard Cohen, for giving me the opportunity to work in his laboratory during my graduate years. I would also like to thank my thesis readers, Profs. Roger Mark and George Verghese for the contributions that they have made to this thesis. I am especially grateful to Dr. Mark for being my role model.

This thesis would not have been possible if it were not for the members of Dr. Cohen's laboratory. I would like to thank these members, both former and present, for the role that they have played. In particular, Derin Sherman has contributed to this thesis in a multitude of ways. The combination of Derin's scientific talents and helpful personality has substantially improved this thesis. Antonis Armoundas has provided me with constant support throughout my graduate studies including loyal friendship. Andy Feldman was always willing to offer an understanding ear at any time. Tom Mullen introduced me to Dr. Cohen's laboratory and is responsible for shaping my graduate studies. Richard Chen and Ming Maa provided me with some useful software utilities and experimental data. Thomas Heldt, a member of Dr. Mark's laboratory, helped me considerably in terms of forward modeling the cardiovascular system. Finally, Karin Toska, Wei Zong, and Jan Yelle were responsible for providing me with the experimental data presented in this thesis.

I would also like to express my appreciation to those individuals who have given me their friendship during my graduate years. I could not have made it through here without them. I am especially grateful to Eric Reed and Wade Wan in this regard.

I thank the Whitaker Foundation for providing me with generous fellowship support during the first five years of graduate study.

Finally, I would like to thank my parents, Durga and Mohanrao, and my sisters, Sasi and Chitra, for all their support and encouragement during my graduate studies. I dedicate this thesis to them.

Contents

List of Figures

List of Tables

Chapter 1

Introduction

When one considers modeling the cardiovascular system, one usually envisions constructing a model based on physical principles that is capable of generating realistic data (*e.g.*, pressures, volumes, and flow rates). This type of modeling approach, which we refer to as forward modeling, is a useful tool for developing an understanding of cardiovascular physiology. One may also consider an inverse modeling approach in which models are built from measured data. This type of modeling approach, in the context of the cardiovascular system (or any dynamical system for that matter), is referred to as system identification. System identification specifically deals with the mathematical estimation of dynamical transfer function models relating measured system input and output data [47,79].

1.1 Cardiovascular System Identification

Over the past two decades, our laboratory has considered modeling the cardiovascular system using the methods of system identification (see, for example, [1,4,6,8,9,16,17, 56–59,67,75,76]). We have particularly focused on the fluctuations in cardiovascular signals about their mean values at frequencies below the mean heart rate ($\sim$1 Hz) and on the time scales of seconds to minutes. These hemodynamic fluctuations reflect the

interplay between perturbations to the cardiovascular system and the dynamic, compensatory response of the regulatory system which is governed predominantly by the autonomic nervous system [4]. A system identification analysis of such fluctuations in multiple cardiovascular signals may thus provide a quantitative characterization of the autonomic regulatory mechanisms (as well as other physiologic mechanisms) responsible for the couplings between the signals. The characterization is in terms of a set of transfer functions which represents a "snapshot" of the cardiovascular state of the individual from whom the data is obtained. The number of transfer functions in the set reflects the degree of detail of the picture and is determined by the number of signals considered for analysis. That is, if n signals are analyzed, then it is possible to identify $n(n-1)$ causal transfer functions. System identification may potentially play a central role in the clinical management of patients with autonomic neuropathies (*e.g.*, diabetics and heart failure patients) by providing a powerful means for tracking these patients' cardiovascular states over time so as to guide therapy on an individualized basis.

To this end, we have previously developed a cardiovascular system identification method for the analysis of fluctuations in noninvasively measured heart rate, arterial blood pressure (ABP), and respiratory activity (in terms of instantaneous lung volume, ILV) in order to characterize quantitatively the physiologic mechanisms responsible for the couplings between these signals[1] [59]. There are six possible causal transfer functions relating the measured fluctuations; however, we consider the estimation of only those four which represent physiologic mechanisms. Two of these physiologic transfer functions represent the distinct feedforward and feedback pathways of the closed-loop relationship between heart rate and ABP. That is, the transfer function relating heart rate fluctuations to ABP fluctuations (feedforward) reflects the

[1] ABP is measured at the finger with the Finapres technique [38], while ILV is measured with a two-belt chest-abdomen inductance plethysmograph.

mechanical properties of the heart and vasculature, while the transfer function relating ABP fluctuations to heart rate fluctuations (feedback) represents the autonomically mediated heart rate baroreflex. The other two physiologic transfer functions are the open-loop couplings of ILV fluctuations to heart rate fluctuations and ILV fluctuations to ABP fluctuations. The former transfer function represents the direct autonomically mediated coupling between respiration and heart rate, while the latter transfer function reflects the mechanical effects of respiratory-induced intrathoracic pressure changes on ABP fluctuations.

As with any system identification method, our method essentially involves three steps: data collection, transfer function estimation, and model validation. In the next three paragraphs, we describe each of these steps at a conceptual level. See Section 5.1 for a more detailed presentation of the method.

In order to obtain a complete characterization of each of the above physiologic mechanisms, system identification requires that the measured input signals are "persistently exciting" of high enough order [47, 79]. This means that the input signals are sufficiently uncorrelated and contain at least as many frequency components as the number of parameters of the system to be identified. Thus, independent white inputs are ideal but are sometimes not possible to implement in practice as is the case here. However, during the data collection period, we incorporate a protocol in which subjects are instructed to breathe on cue to a sequence of randomly spaced auditory tones while controlling their own tidal volume in order to maintain normal ventilation [8]. This random-interval breathing protocol results in an ILV signal with spectral power over a significantly wider frequency range as compared to that obtained from spontaneous breathing. It is also important to recognize that the random-interval breathing protocol described here represents only a relatively small deviation from normal physiologic conditions. This is in contrast to other techniques for the quantification of autonomic regulatory mechanisms which perturb the cardiovascular system

in a highly nonphysiologic manner in order to elicit a compensatory response [51,52].

Without a doubt, the physiologic mechanisms responsible for cardiovascular regulation are highly complex, capable of exhibiting both nonlinear and time-varying phenomena. However, when a subject is following our random-interval breathing protocol and is otherwise at rest, we have found that the fluctuations in the measured signals are sufficiently small such that the transfer functions relating the fluctuations can be linearized about the mean values of the signals (operating point)[2]. We also have found that, during these stable experimental conditions, the statistical properties of the measured fluctuations do not change much over the short data collection period. Hence, we consider the estimation of linear, time-invariant (LTI) transfer function models. We particularly consider AutoRegressive Moving Average (ARMA) models, a specific class of LTI models that are completely characterized by a finite set of adjustable parameters. This type of model permits the imposition of causality which is a necessary condition to identify distinctly the feedforward and feedback transfer functions relating two signals obtained in closed-loop (*e.g.*, heart rate fluctuations and ABP fluctuations) [87]. Since ARMA models are linear in their parameters, we utilize the convenient, analytic methods of linear least squares for the estimation of the four physiologic transfer functions [47,79].

For the purposes of model validation, we have evaluated our cardiovascular system identification method during the conditions of pharmacological autonomic blockade, postural changes, and diabetic autonomic neuropathy [57,59]. We found that these three conditions altered the transfer function estimates in a manner consistent with known physiologic mechanisms. This suggests that the transfer function estimates may reflect actual physiologic mechanisms.

[2]In a previous study [17], our laboratory found that second-order nonlinear models only provide a modest improvement in accounting for the heart rate fluctuations observed during these stable experimental conditions with respect to linear models.

1.2 Motivation

The validity of the precise dynamical properties of the physiologic transfer function estimates from our cardiovascular system identification method may be addressed through experimentation. To this end, it is necessary to establish, in a manner independent of system identification, gold standard transfer functions against which the estimates may be evaluated. For example, let us consider the experimental validation of the transfer function representing the heart rate baroreflex coupling ABP fluctuations to heart rate fluctuations. In order to measure experimentally this transfer function, the closed-loop relationship between ABP and heart rate must be opened. This could be done by ablating the atrioventricular node of the heart and pacing the ventricle. However, this type of experiment could only be done in an animal and requires some sophistication. Hence, before proceeding with such an experiment, it would seem prudent to evaluate first the estimated transfer functions with a forward model of the cardiovascular system whose dynamical properties are known. Provided that this theoretical evaluation is a success, animal experimentation would then be further justified. It is also possible that validation through such an animal experiment is not feasible, because it is based on the assumption that the cardiovascular state and/or operating point do not change from the stable experimental conditions of system identification data collection to the open-loop conditions of the experimental preparation. That is, demonstrating the validity of the estimated transfer function dynamics may only be possible on theoretical grounds.

A forward model of the cardiovascular system would also provide a means to analyze the sensitivity or resolving power of our cardiovascular system identification method. That is, we would be able to determine how much the dynamical properties of the forward model would have to be altered before we would see a corresponding change in the transfer function estimates. Since precise control of the dynamical properties of an animal preparation is not possible, this protocol could not be as

effectively carried out in an experiment.

Certainly, the major limitation of such an analysis is that the results are only as meaningful as the extent to which the forward model coincides with the actual cardiovascular system. This limitation can be attenuated, at least to some extent, by determining the robustness of the results over a set of forward models. This set may naturally arise from a nominal forward model either through the inclusion of additional parameters (increased complexity) or simply through the variation of its parameters. For example, the identification of the heart rate baroreflex could be analyzed as a function of a parameter reflecting the degree of nonlinear system dynamics.

A forward model of the cardiovascular system would also provide a convenient test bed of data which would facilitate the development of new identification methods that could be incorporated with the cardiovascular system identification method so as to provide a more detailed picture of cardiovascular state. We are particularly interested in the development of a practical identification method for the quantitative characterization of the total peripheral resistance (TPR) baroreflex which requires only the additional measurement of beat-to-beat left ventricular flow rate (cardiac output, CO). This signal may be obtained noninvasively in humans via a Doppler ultrasound technique[3] [29]. The TPR baroreflex is mediated by the α-sympathetic branch of the autonomic nervous system [51, 52] and is believed to be significantly involved in the orthostatic intolerance commonly seen in patients with autonomic neuropathies [6, 19]. The characterization of this regulatory mechanism would nicely complement the characterization of the heart rate baroreflex, which is mediated by both the β-sympathetic and parasympathetic branches of the autonomic nervous system [2]. Hence, the expanded cardiovascular system identification method would

[3]It is also possible to measure CO on a beat by beat basis in humans with a thoracic impedance technique [70]; however, the accuracy of this method is suspect.

provide a more comprehensive, clinically useful picture of the integrity of the autonomic nervous system. Of course, the additional CO measurement would also provide a convenient means for monitoring steady-state changes in TPR through the ratio of mean ABP to mean CO. However, the Doppler ultrasound measurement requires an expert operator and consequently, may not always be available. Hence, we are also interested in the development of an identification method for tracking steady-state changes in TPR from only the ABP waveform.

It should be noted that the general notion of analyzing inverse modeling methods based on physical models of the cardiovascular system is not novel to the cardiovascular research community. For example, investigators have previously utilized complex, forward models of the systemic circulation in order to evaluate the estimation of lumped parameters representing TPR and systemic arterial compliance [15, 26].

1.3 Specific Aims

There are four specific aims of the research presented in this thesis. They are listed as follows:

1. To build a computer model of the human cardiovascular system for the purposes of analyzing practical system identification methods.

2. To evaluate the cardiovascular system identification method described in Section 1.1 with respect to this forward model in terms of accuracy, robustness, and sensitivity.

3. To develop and evaluate a practical identification method for the quantitative characterization of the TPR baroreflex which requires only CO and ABP measurements based on the forward model and to consider a complementary analysis with experimental data.

4. To analyze an identification method for tracking steady-state changes in TPR which requires only the ABP waveform against the forward model as well as a preliminary set of experimental data.

1.4 Thesis Organization

This thesis is divided into two parts. Part I deals with the development of a forward model of the cardiovascular system, while Part II deals with the analysis of cardiovascular system identification methods based on data generated from the forward model. Part I specifically includes Chapters 2 and 3. In Chapter 2, we present a set of forward models of the heart and circulation and demonstrate that the nominal model in the set behaves reasonably in terms of pulsatile and limiting static behaviors. In Chapter 3, we describe the regulatory system model along with a model of physiologic perturbations which are incorporated with the heart and circulation model and demonstrate that this overall model of the cardiovascular system is capable of generating realistic short-term, low frequency hemodynamic fluctuations in signals that may be measured noninvasively. Part II encompasses Chapters 4-7. In Chapter 4, we describe the system identification data analysis tools, which are based on the analytic methods of linear least squares estimation (see Section 1.1), that are utilized in the following three chapters. In Chapter 5, we evaluate the cardiovascular system identification method introduced in Section 1.1 in terms of its accuracy, robustness, and sensitivity against data generated from the forward model. In Chapter 6, we present the development and evaluation of identification methods for the quantitative characterization of the TPR baroreflex which require only CO and ABP measurements based on the forward model. This chapter also includes a complementary analysis of experimental data. In Chapter 7, we analyze an identification method for monitoring steady-state changes in TPR from only the ABP waveform based on forward model

generated data and a preliminary set of experimental data. Finally, in Chapter 8, we summarize the major results of this thesis work and present potential future studies.

Part I

Forward Modeling

Chapter 2

Heart and Circulation

It would be virtually impossible to construct a model of the heart and circulation which could account for its complete spectrum of dynamical behaviors. One must settle to build a model which can provide only a simplified picture of the heart and circulation. Our general philosophy in modeling the cardiovascular system is one of minimal modeling. That is, we seek a model that is capable of accounting for the particular behaviors that we are interested in with minimal complexity.

In modeling the heart and circulation, the major simplifying assumption that we make is that it can be represented by a lumped parameter model. This type of model is not capable of exhibiting distributed behaviors, such as pulse reflections in the arterial system, but rather only what one might think of as the average behavior of each lump. Since we are primarily interested in accurately accounting for hemodynamic behavior at frequencies below the mean heart rate, this type of average behavior seems to be adequate for our purposes. Fortunately, numerous lumped parameter models of the heart and circulation have been developed (see, for example, [5,11,23,31,84]), ranging in complexity from extremely simple consisting of a few parameters (*e.g.*, RC circuit model in Figure 6-3) to highly complex containing hundreds of parameters.

In this chapter, we present a set of lumped parameter models of the heart and

circulation of increasing complexity. The data generated from this set in concert with the models of the short-term regulatory system and resting physiologic perturbations described in Chapter 3 represent the test bed against which the identification methods in Part II are assessed. We begin here by describing a relatively simple lumped parameter model that has been previously developed which serves as the basis for the least complex model in the set, the nominal model (Section 2.1). Then, we present our modifications to this previously developed model which are geared towards improving the model in terms of the behaviors in which we are specifically interested (Section 2.2). Next, we present the parameter values and describe the computer implementation of the resulting nominal model (Section 2.3) and demonstrate that this model is capable of behaving reasonably in terms of both pulsatile and static behaviors (Section 2.4). We conclude the chapter by presenting a set of more complex models which are derived through modification of the nominal model and motivated particularly by a robustness analysis of the identification methods considered in Chapters 6 and 7 (Section 2.5).

2.1 Nominal Model: CVSIM

Our nominal model of the heart and circulation is based on CVSIM which was originally developed at MIT as an aid in teaching cardiovascular physiology [23]. CVSIM is shown in Figure 2-1 in terms of its electrical circuit analog. Here, charge is analogous to blood volume (Q, ml), current, to blood flow rate ($\dot{q}$, ml/s), and voltage, to pressure (P, mmHg). Thus, the capacitors may be interpreted as blood volume containers with compliances (C), while the resistors may be thought of as conduits for viscous blood flow with resistances (R). CVSIM consists of six compartments which represent the left and right ventricles (l, r), systemic arteries and veins (a, v), and pulmonary arteries and veins (pa, pv). Each compartment consists of a linear capaci-

tor and a linear resistor which share a single node. Each capacitor is parametrized by a dead volume (Q^0, a nonzero volume at zero pressure) as well as a compliance. That is, the static constitutive relationship for each of the capacitors is given as follows:

$$Q_i = C_i\,(P_i - P_i^{ref}) + Q_i^0, \tag{2.1}$$

where the subscript i denotes any of the six compartments (l, r, a, v, pa, pv). The reference pressure is ground for the systemic circulation compartments and intrathoracic (th) pressure for the ventricle and pulmonary circulation compartments since they reside in the thorax. The compliances of the ventricles vary periodically over time (t) according to the ventricle model of Suga and Sagawa [80, 81] (see Section 2.3.1) and are responsible for driving the flow of blood. The model is linear with the exception of four ideal diodes which represent the ventricular inflow and outflow valves and ensure uni-directional blood flow.

Figure 2-1 Electrical circuit analog of CVSIM [23].

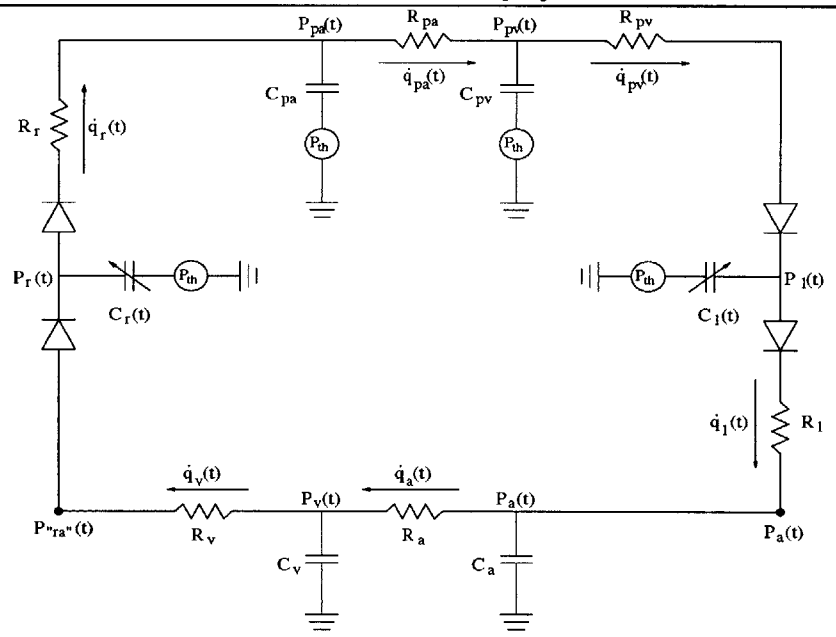

CVSIM was built for the purpose of teaching, which requires a simple, readily understandable model. It is remarkable that the simple model in Figure 2-1 is capable of accounting for a substantial amount of the dynamical behaviors exhibited by the

cardiovascular system. We choose CVSIM as the basis of our heart and circulatory model, because its level of simplicity, in terms of its number of compartments, seems to be about right for the particular cardiovascular system identification methods that we analyze in Part II. However, several of its other simplifying assumptions are acceptable for our modeling purposes as well.

For example, the CVSIM heart and circulatory model does not include compartments representing the atria. The atria only play a significant role in hemodynamics during high heart rates, such as those obtained during exercise [23]. Moreover, the effect of the atria can be partially accounted for by adjusting some of the compliance and resistance values of the other compartments. Another example is that CVSIM neglects the inertial effects of blood flow[1] which play a role in, for example, producing the dicrotic notch of the central arterial blood pressure (ABP) wavelet. Inertial effects are most important in the low resistance pulmonary circuit and even here, it is probably only a second-order effect [23]. Furthermore, the system identification methods that we analyze in Part II do not consider measurements in the pulmonary circulation and so error here is probably more acceptable. Yet another example is that CVSIM assumes that all of the compartmental elements are linear. In reality, none of these elements are perfectly linear over their entire dynamical range. However, when considering dynamical behaviors over only the limited physiologic range as is the case here, this simplification becomes quite reasonable for most but not all of the elements.

[1] However, in Section 2.5.2, we do consider modeling inertial effects in the arterial system in order to assess the robustness of the identification method introduced in Chapter 7 against peripheral arterial pressure waveforms.

2.2 Nominal Model: Nonlinear Elements

The systemic venous and pulmonary arterial resistances are believed to be significantly nonlinear even over their more limited physiologic range. In Sections 2.2.1 and 2.2.2, we describe more accurate, nonlinear models of these elements which are incorporated in CVSIM. We also include, in Sections 2.2.3, the motivation for and description of a nonlinear model of the time-varying ventricular compliances.

2.2.1 Systemic Venous Resistance

The large systemic veins entering the thoracic compartment are collapsible vessels. That is, these vessels are completely closed when their reference (external) pressure is larger than their internal pressure, while they are fully open when their internal pressure is larger than their external pressure. Systemic venous collapse may occur under normal physiologic conditions, probably during the early diastolic filling phase of the right heart. The pressure-flow rate properties of the collapsible veins can be well modeled with a Starling resistor, which is a thin-walled, nonelastic, collapsible tube in a pressure chamber. A complete, dynamical analysis of the properties of a Starling resistor is quite involved. However, a simple, steady-state analysis of its pressure-flow rate relationship has proven to be quite useful [66]. Consider that the pressure in the chamber is $P_c(t)$, and the inflow and outflow pressures of the collapsible tube (both defined just outside the pressure chamber) are $P_{in}(t)$ and $P_{out}(t)$, respectively. Then, the following three quantitative statements summarize the results of the simple steady-state analysis:

$$\dot{q}(t) = 0 \qquad P_c(t) \geq P_{in}(t) \geq P_{out}(t) \tag{2.2}$$

$$\dot{q}(t) = \frac{P_{in}(t) - P_c(t)}{R} \qquad P_{in}(t) > P_c(t) > P_{out}(t) \tag{2.3}$$

$$\dot{q}(t) = \frac{P_{in}(t) - P_{out}(t)}{R} \qquad P_{in}(t) > P_{out}(t) \geq P_c(t), \tag{2.4}$$

where $\dot{q}(t)$ is the flow rate through the collapsible tube with resistance R. The first and third statements are very intuitive. They respectively indicate that there is no blood flow when the tube is completely closed and that blood flow is governed by Poiseuille's law when the tube is fully open. However, the second statement, which is referred to as the vascular waterfall effect, is most interesting. In this case, the pressure near the outflow end of the collapsible tube cannot be greater than the chamber pressure, because this pressure would then be transmitted to the lower outflow pressure. On the other hand, the pressure cannot be less than the chamber pressure, because the larger inflow pressure would be transmitted to this pressure. So the pressure near the outflow end of the tube can be considered to be equal to the chamber pressure[2]. Thus, the flow rate through the outflow end of the collapsible tube is independent of the pressure gradient $(P_c(t) - P_{out}(t))$ analogous to the waterfall effect. Rather, the flow rate is controlled by modification of the outflow area of the tube (Torricelli's principle), with larger areas providing for greater flow rates.

It is important to note that the flow rate in this model cannot be arbitrarily increased by decreasing outflow pressure. Since the chamber pressure of the collapsible veins is about 0 mmHg, this model accurately accounts for the experimental finding that blood flow to the right heart cannot be increased by suctioning (negative heart pressures; see Section 2.4.2). We incorporate a Starling resistor with a chamber pressure of 0 mmHg in place of the linear systemic venous resistor (R_v in Figure 2-1) of CVSIM to account for the collapsible systemic veins.

2.2.2 Pulmonary Arterial Resistance

The pulmonary capillaries are collapsible vessels as well with alveolar pressure considered to be their external pressure. However, the simple Starling resistor model is

[2] A more complete, dynamical analysis would certainly demonstrate fluttering around the chamber pressure.

not sufficient to account for the pressure-flow rate characteristics here, because hydrostatic effects contribute significantly in the low pressure pulmonary circuit and must be taken into account as well. We can better understand these effects by conceptualizing the lungs as a large number of parallel Starling resistors, arranged vertically, one on top of the other as in Figure 2-2. Let us consider that these parallel resistors extend to about 10 cm below and 20 cm above the pulmonary artery and vein[3], the respective reservoirs from which each of the resistors receive and empty blood. Hence, the inflow and outflow pressures of each Starling resistor is dependent on its vertical position relative to the pulmonary artery and vein which are respectively at pressures $P_{pa}(t)$ and $P_{pv}(t)$. For example, the inflow and outflow pressures of the Starling resistors at the top of the lungs are considerably lower than $P_{pa}(t)$ and $P_{pv}(t)$, the inflow and outflow pressures of the Starling resistors located at the level of the pulmonary artery and vein. On the other hand, the inflow and outflow pressures of the Starling resistors located at the bottom of the lungs are considerably higher than $P_{pa}(t)$ and $P_{pv}(t)$. However, the alveolar pressure ($P_{alv}(t)$), the chamber pressure of each Starling resistor, is hardly influenced by hydrostatic factors and can be considered to be essentially constant regardless of vertical position. This conceptual picture leads to the notion of three zones of blood flow in the lungs [32] which correspond to the three quantitative statements characterizing blood flow in Starling resistors presented in Section 2.2.1. That is, at the top of the lungs, there may be no blood flow (zone 1), in the middle of the lungs, the blood flow is governed by the vascular waterfall effect (zone 2), and at the bottom of the lungs, the blood flow is governed by Poiseuille's law (zone 3).

The conceptual picture here also leads to a simple but accurate pressure-flow rate relationship characterizing blood flow in the lungs. To this end, let us assume that each of the Starling resistors are of equal resistance and are equidistant with vertical

[3]These are typical values for an adult human [32].

Figure 2-2 Conceptual picture of the pulmonary arterial resistance model where each of the boxed resistors represent Starling resistors with chamber pressure $P_{alv}(t)$.

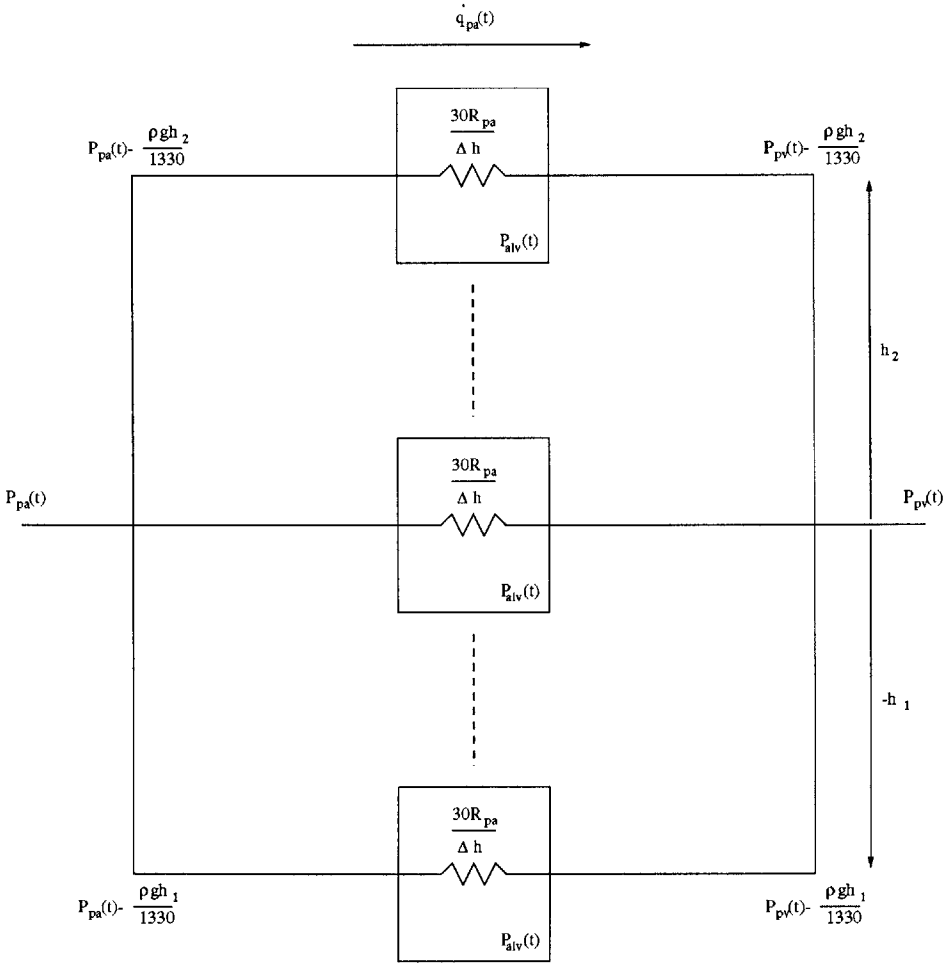

distance Δh between each resistor. Then, given that the lumped resistance of the entire lung is R_{pa}, the resistance of each resistor may be given by $\frac{30}{\Delta h}R_{pa}$, where the 30 represents the entire vertical height of the lungs in cm. Let us further assume the lungs to be an infinite number of parallel Starling resistors, that is, $\Delta h \to 0$. Then, the differential flow rate $(d\dot{q}_{pa}(t,h))$ as a function of vertical distance with respect to the pulmonary artery and vein (h) in the lungs may be given as follows:

$$d\dot{q}_{pa}(t,h) = \begin{cases} 0 & P_{alv}(t) \geq P_{pa}(t) - \frac{\rho gh}{1330} \geq P_{pv}(t) - \frac{\rho gh}{1330} \\ \frac{P_{pa}(t) - \frac{\rho gh}{1330} - P_{alv}(t)}{30R_{pa}} dh & P_{pa}(t) - \frac{\rho gh}{1330} > P_{alv}(t) > P_{pv}(t) - \frac{\rho gh}{1330} \\ \frac{P_{pa}(t) - P_{pv}(t)}{30R_{pa}} dh & P_{pa}(t) - \frac{\rho gh}{1330} > P_{pv}(t) - \frac{\rho gh}{1330} \geq P_{alv}(t), \end{cases} \tag{2.5}$$

where dh is the differential vertical distance between Starling resistors, ρ, the density

of blood, is equal to 1.06 g/cm^3, and g gravity is equal to 980 cm/s^2. Now, we may integrate the differential flow rate over the entire vertical height of the lungs as follows:

$$\dot{q}_{pa}(t) = \int_{-10}^{20} d\dot{q}_{pa}(t,h) = \int_{-10}^{h_1} \frac{P_{pa}(t) - P_{pv}(t)}{30R_{pa}} dh + \int_{h_1}^{h_2} \frac{P_{pa}(t) - \frac{\rho g h}{1330} - P_{alv}(t)}{30R_{pa}} dh \tag{2.6}$$

which results in the following nonlinear, lumped pressure-flow rate relationship:

$$\dot{q}_{pa}(t) = \frac{P_{pa}(t) - P_{pv}(t)}{30R_{pa}}(h_1 + 10) + \frac{P_{pa}(t) - P_{alv}(t)}{30R_{pa}}(h_2 - h_1) - \frac{\rho g}{79800R_{pa}}(h_2^2 - h_1^2), \tag{2.7}$$

where

$$h_1 = \frac{1330}{\rho g}(P_{pv}(t) - P_{alv}(t)), \tag{2.8}$$

$$h_2 = \frac{1330}{\rho g}(P_{pa}(t) - P_{lav}(t)), \tag{2.9}$$

with the restriction that $-10 \leq h_1 \leq h_2 \leq 20$. Note that h_1 and h_2 denote the vertical boundaries of the three zones of blood flow, with h_1 being the boundary between zones 2 and 3 and h_2, between zones 1 and 2. These boundaries are determined from the flow rate conditions in Equation (2.5).

This model is essentially the same as that presented by Permutt et al. [65]. These investigators demonstrated that this simple model was capable of explaining experimental data reported in the literature. For example, they showed that the model was able to account for the experimental finding that the pulmonary artery pressure is relatively constant over a large range of flow rates. We incorporate this nonlinear model in place of the linear pulmonary arterial resistor (R_{pa} in Figure 2-1) of CVSIM.

2.2.3 Time-Varying Ventricular Compliance

Although the pressure-volume relationship of the ventricle changes continuously throughout systole and isovolumic relaxation, ventricular performance is determined by only

the pressure-volume relationships at the end of systole and during diastolic filling. These two pressure-volume relationships have a fairly wide linear range, but nonlinearities in these relationships have been reported in the literature as well. In particular, it has been shown that the isolated dog ventricle becomes stiffer with increasing volume during diastolic filling in such a manner that measured diastolic pressure-volume pairs have been fitted with growing exponential curves convex to the volume axis [27,82]. Certainly, these findings confirm our intuition that the ventricle cannot possibly fill to arbitrarily large volumes during diastole. That is, it must have a maximum volume. On the other hand, the end-systolic pressure-volume relationship has been generally considered to be linear ever since the pioneering experiments of Suga and Sagawa in isolated dog left ventricles [54,80,81]. These investigators particularly found this pressure-volume relationship to be linear up to about 180 mmHg. They were not able to explore the relationship at higher pressures because these conditions led to frequent arrhythmias. Certainly, this relationship must eventually saturate, since the ventricle could not possibly generate arbitrarily large pressures. However, it is not necessarily clear whether the saturation begins at volumes less than the diastolic volume limit in isolated dog left ventricles. Studies in smaller, puppy left ventricles, which are less susceptible to arrhythmias, have demonstrated saturation in the end-systolic pressure-volume relationship at high pressures and that the saturation does indeed begin at volumes within the diastolic volume limit [22,82]. Furthermore, several studies have recently demonstrated a contractility-dependent curvilinearity in this relationship over smaller volume ranges [14,41,54].

The exclusion of the ventricular nonlinearities results in gross inaccuracies when considering the cardiac pumping capacity at the limits of its operating range; however, only the limiting behavior of the ventricles plays an important role in this regard with the precise curvature of these relationships contributing little[4]. Furthermore, the

[4]The pressure-volume relationships of the remaining circulatory compartments undoubtedly in-

end-systolic and diastolic pressure-volume relationships are, at least to first approximation, linear over the physiologic volume range. Although it was not necessary for our purposes, we incorporate simple, essentially piece-wise linear pressure-volume relationships as in Figure 2-3 in place of the perfectly linear ventricular compliances of CVSIM. The upper curve in each plot is the end-systolic pressure-volume relationship, while the bottom curve is the diastolic pressure-volume relationship. The curves in between represent the remaining ventricular pressure-volume relationships during the systole and isovolumic relaxation. Similar end-systolic and diastolic pressure-volume relationships have been previously implemented in a model of the dog heart [73]. In the context of our original purpose, these relationships will clearly indicate the importance for consideration of changes in operating point during the interpretation of linear system identification results.

Figure 2-3 Models of the nonlinear, time-varying pressure-volume relationships for the (a) left ventricle and (b) right ventricle. The parameters characterizing these models are largely from [32].

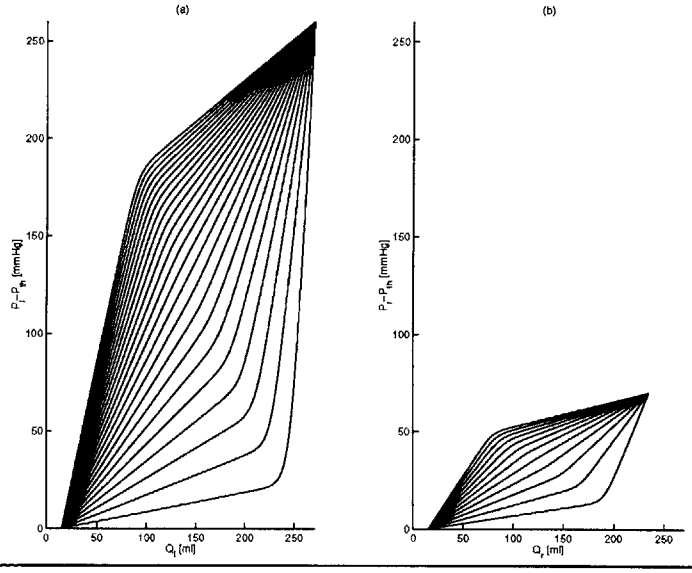

In order to implement the models of the ventricles in Figure 2-3, the pressure-volume relationships must be differential with respect to time and thus cannot be

clude nonlinear limits as well; however, their role in limiting hemodynamic behavior is small with respect to the nonlinear ventricular limits.

perfectly piece-wise linear. As mentioned above, the curves in between the end-systolic and diastolic pressure-volume curves are irrelevant in determining ventricular output and are chosen only to satisfy this implementation requirement. In particular, each member of the family of ventricular (both right and left) pressure-volume curves is mathematically represented by the sum of a linear term and the integral of a shifted and scaled hyperbolic tangent function as follows:

$$y_{l,r}(t) = \alpha_{l,r}(t)x(t) + \beta_{l,r}(t)\int_0^{x(t)} \frac{dx(t)}{1+\mathrm{e}^{-k(x(t)-x^0_{l,r}(t))}}, \quad 0 \le x(t) \le 1, \tag{2.10}$$

where k=50 and characterizes the transition rate of the hyperbolic tangent function and $x^0_{l,r}(t)$ and $\beta_{l,r}(t)$ respectively denote the shift and scale factor of the hyperbolic tangent and are defined as follows:

$$x^0_{l,r}(t) = \frac{1}{1+\alpha_{l,r}(t)}, \tag{2.11}$$

$$\beta_{l,r}(t) = \frac{1-\alpha_{l,r}(t)}{\int_0^1 \frac{dx(t)}{1+\mathrm{e}^{-k(x(t)-x^0_{l,r}(t))}}}. \tag{2.12}$$

The solution to the above integrals is given as follows:

$$\int_0^{x(t)} \frac{dx(t)}{1+\mathrm{e}^{-k(x(t)-x^0_{l,r}(t))}} = x(t) + \frac{1}{k}\ln\left\{\frac{1+\mathrm{e}^{-k(x(t)-x^0_{l,r}(t))}}{1+\mathrm{e}^{kx^0_{l,r}(t)}}\right\}. \tag{2.13}$$

In these equations, $y_{l,r}(t)$ and $x(t)$ respectively represent normalized ventricular transmural pressure and volume. That is, we may obtain the actual, unnormalized ventricular pressure and volume with the following relationships:

$$P_{l,r}(t) = \Delta P^{max}_{l,r} y_{l,r}(t) + P_{th}(t), \tag{2.14}$$

and

$$Q_{l,r}(t) = (Q^{max}_{l,r} - Q^0_{l,r})x(t) + Q^0_{l,r}, \tag{2.15}$$

where $\Delta P_{l,r}^{max}$ and $Q_{l,r}^{max}$ are respectively the maximum ventricular end-systolic pressure and diastolic volume[5]. Note that each pressure-volume curve (at a fixed time) is parametrized by only a single parameter $\alpha_{l,r}(t)$. This parameter is responsible for determining the breakpoint, the concavity or convexity, and the slope of the initial linear portion of each curve and is given as follows:

$$\alpha_{l,r}(t) = \frac{Q_{l,r}^{max} - Q_{l,r}^{0}}{C_{l,r}(t)\Delta P_{l,r}^{max}}, \tag{2.16}$$

where $C_{l,r}(t)$ represents the linear, time-varying ventricular compliance (see Section 2.3.1). Thus, the initial slope and breakpoint cannot be independently set. However, this is not a problem as we see in Figure 2-3 that the choice of the initial slope of the end-systolic pressure-volume relationship does not compromise the location of the breakpoint which is at a pressure of about 180 mmHg for the left ventricle.

It should be noted that volume cannot be analytically expressed as a function of pressure here. Hence, we must resort to implementing a numerical search method to find the volume associated with a given pressure. However, this is not much of an encumbrance for the following reasons: each of the pressure-volume curves is a one-to-one function over the interval of interest (see Equation 2.10); the interval is small; and a good initial guess of the volume is available from the previous ventricular volume (see Section 2.3). The final reason allows us to utilize effectively the extremely fast Newton's method which has quadratic convergence properties [69].

The pressure-flow rate relationship of nonlinear ventricular element presented here may be determined by simply taking the derivative of the above pressure-volume relationship with respect to time. However, since the resulting relationship is quite involved, we include it in Appendix A.

[5]Although intrathoracic pressure is considered in this chapter to be a fixed constant (see Section 2.3.1), we treat it in Equation (2.14) and in subsequent equations more generally as a function of time. The rationale for this is made clear in the following chapters

Since we are interested in minimal modeling and the presence of a systolic pressure limit over the relevant volume range in large ventricles is questionable, it is interesting to consider whether the diastolic volume limit alone could reasonably account for limiting cardiac pumping behavior. In fact, this has been previously shown to be possible from a qualitative standpoint [20]. However, we have found that, in order to obtain quantitatively reasonable behaviors (see Section 2.4.3), the end-systolic pressure limit is necessary as well. One may also deduce this by the following "back of the envelope" calculation. The pressure and volume of the normal adult human left ventricle at the end of systole are respectively about 100 mmHg and 40 ml [32]. Hence, assuming a perfectly linear end-systolic pressure-volume relationship and neglecting the dead volume, the slope of this relationship is about 2.5 mmHg/ml. If we assume that a typical human is able to double his/her normal stroke volume (80 ml) through just the Frank-Starling mechanism (without enhancement in contractility), then the maximum end-diastolic volume would be about 200 ml. An isovolumic contraction at this volume would thus generate a systolic pressure of about 500 mmHg. However, peak systolic pressures usually range from only about 250 to 300 mmHg [32]. Hence, in order to obtain quantitatively reasonable behaviors, an end-systolic pressure limit must be included.

2.3 Nominal Model Implementation

The first step towards the computer implementation of the nominal heart and circulatory model described in Sections 2.1 and 2.2 is to formulate the dynamical equations that govern the model. The equations may be conveniently formulated in terms of a state-space description, a set of coupled, first-order differential equations whose known quantities are considered to be the model parameter values and unknown quantities, the pressures, volumes, and flow rates of the model as functions of time. The time

evolution of these unknown quantities may be determined by using well established numerical integration techniques for solving state-space equations. These algorithms require as an input the initial conditions of the unknown quantities (initial state). In Sections 2.3.2-2.3.4, we present the formulation of the state-space equations, the determination of initial conditions, and a description of the employed numerical integration method. But first, in Section 2.3.1, we present the numerical values that are assigned to the parameters characterizing the nominal model.

2.3.1 Parameter Values

The parameter values of the original CVSIM model are based on solid experimental evidence and permit reasonable steady-state pulsatile behavior [23]. However, we reconsider the assignment of a numerical value to R_v which, due to the omission of the right atrium, simultaneously represents the small right ventricular inflow resistance and the relatively large systemic venous resistance[6]. Hence, the choice of R_v amounts to a trade-off between accurately modeling right ventricular filling dynamics and systemic venous return dynamics. In the original CVSIM model, R_v was chosen such that the systemic venous return dynamics were modeled accurately at the complete expense of the right ventricular filling dynamics. As a consequence, the original CVSIM model is grossly inaccurate in terms of dynamical behavior over the range of heart rates considered by the identification methods in Part II. We therefore modify the original value assigned to R_v so as to improve the dynamical performance of the model over this heart rate range without completely compromising the systemic venous return dynamics (see Section 2.4.5). We also adjust the original values assigned to $C_r(t)$ and Q_v^0 in order to permit reasonable steady-state pulsatile and static behaviors (see Section 2.4). Table 2.1 summarizes the modified version of the

[6] Although R_{pv} similarly represents both the left ventricular inflow resistance and the pulmonary venous resistance, these resistances are nearly the same.

original CVSIM model parameter values that are assigned to the nominal heart and circulatory model. The numerical values representing the ventricular pressure and volume limits are determined largely from [32].

Compartment	C, $\frac{\text{ml}}{\text{mmHg}}$	Q^0, ml	Q^{max}, ml	ΔP^{max}, mmHg	R, $\frac{\text{mmHg-s}}{\text{ml}}$ (P_c)
l	0.4-10	15	270	260	0.006
a	1.6	715	—	—	1.0
v	100.0	2600	—	—	0.02 (0)
r	1.2-12.5	15	235	70	0.003
pa	4.3	90	—	—	0.09 ($P_{alv}(t) = 0$)
pv	8.4	490	—	—	0.01
System Parameters:		$T = 5/6$ s			
		$P_{th}(t) =$ -4 mmHg			
		$Q_{total} = 5000$ ml			

Table 2.1: Summary of the nominal heart and circulation model parameters. A chamber pressure (P_c) accompanies resistance in the case of Starling resistors. For the original CVSIM model, C_r=1.2-20 ml/mmHg, Q_v^0=2500 ml, R_v=0.05 mmHg-s/ml, and R_{pa}=0.08 mmHg-s/ml.

Table 2.1 includes the range of compliance values that the ventricles assume over their initial linear range during the cardiac cycle. The equation reflecting the precise time evolution of these values during the cardiac cycle that is incorporated in our model is similar to that of the original CVSIM model. In particular, this equation is completely parametrized by the minimum and maximum compliance values (end-systolic (es) and end-diastolic (ed) compliances, respectively) and the cardiac cycle

duration (T) and is given in terms of elastance (E, reciprocal of compliance) as follows:

$$E_{l,r}(t) = \begin{cases} \frac{1}{2}\left(\frac{1}{C_{l,r}^{es}} - \frac{1}{C_{l,r}^{ed}}\right)\left(1 - \cos(\frac{\pi(t-t_i)}{T_s})\right) + \frac{1}{C_{l,r}^{ed}} & t_i \leq t < t_i + T_s \\ \frac{1}{2}\left(\frac{1}{C_{l,r}^{es}} - \frac{1}{C_{l,r}^{ed}}\right)\left(1 + \cos(\frac{2\pi(t-(t_i+T_s))}{T_s})\right) + \frac{1}{C_{l,r}^{ed}} & t_i + T_s \leq t < t_i + T_{ir} \\ \frac{1}{C_{l,r}^{ed}} & t_i + T_{ir} \leq t < t_{i+1} \end{cases}, \tag{2.17}$$

where the subscript i denotes the beginning of the i^{th} cardiac cycle which starts with systole, $C_{l,r}^{es,ed} = C_{l,r}(t_{es,ed})$, and T_s and T_{ir} respectively represent the time period of systole and isovolumic relaxation for a given cardiac contraction. These latter two parameters may be determined from T through the following two relationships: $T_s = 0.3\sqrt{T}$ and $T_{ir} = T_s/2$. Hence, the time period of diastolic filling (T_d) is given as follows: $T_d = T - 0.45\sqrt{T}$. Figure 2-4 illustrates the time evolution of $E_{l,r}(t)$ based on this equation for one cardiac cycle.

Figure 2-4 Time evolution of the elastance values that the left (red) and right (blue) ventricles assume over their initial linear range during a cardiac cycle.

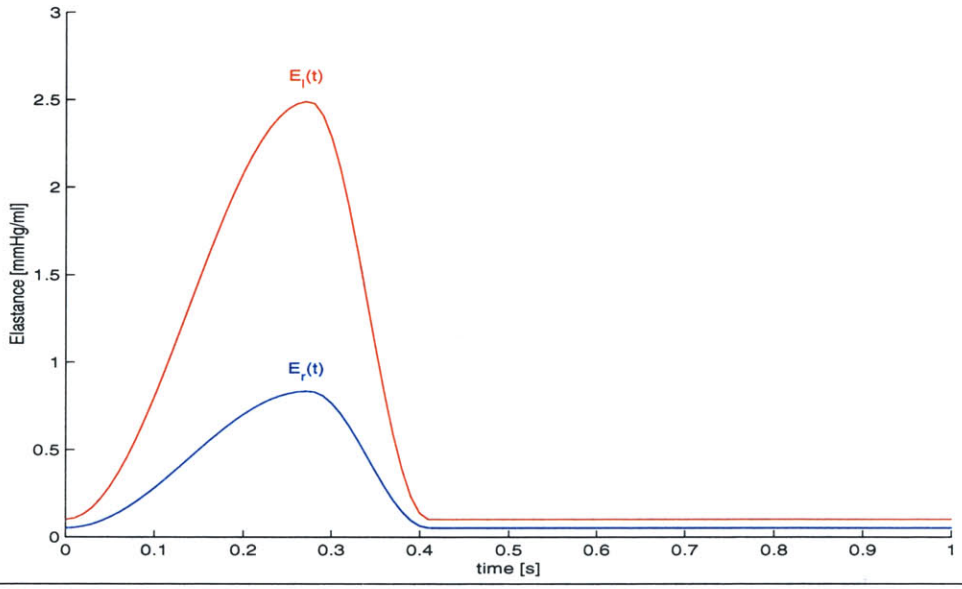

We finally provide the derivative of $E_{l,r}(t)$ with respect to time, which is necessary

for model implementation (see Appendix A), as follows:

$$\frac{dE_{l,r}(t)}{dt} = \begin{cases} \frac{1}{2T_s}\left(\frac{\pi}{C_{l,r}^{es}} - \frac{\pi}{C_{l,r}^{ed}}\right)\sin(\frac{\pi(t-t_i)}{T_s}) & t_i \le t < t_i + T_s \\ \frac{1}{T_s}\left(\frac{\pi}{C_{l,r}^{ed}} - \frac{\pi}{C_{l,r}^{es}}\right)\sin(\frac{2\pi(t-(t_i+T_s))}{T_s}) & t_i + T_s \le t < t_i + T_{ir} \\ 0 & t_i + T_{ir} \le t < t_{i+1} \end{cases} . \quad (2.18)$$

2.3.2 State-Space Description

We call upon basic circuit theory to formulate the governing equations of the nominal model. In particular, we apply Kirchoff's Current Law (KCL) to each of the six nodes of the model and utilize the constitutive relationships for a resistor, capacitor, and the nonlinear elements presented in Section 2.2 to obtain the following state-space description:

$$\frac{dP_l(t)}{dt} = f(Q_l(t) - Q_l^0, \dot{q}_{pv}(t) - \dot{q}_l(t), C_l(t), \dots) + \frac{dP_{th}(t)}{dt} \quad (2.19)$$

$$\frac{dP_a(t)}{dt} = \frac{\dot{q}_l(t) - \dot{q}_a(t)}{C_a} \quad (2.20)$$

$$\frac{dP_v(t)}{dt} = \frac{\dot{q}_a(t) - \dot{q}_v(t)}{C_v} \quad (2.21)$$

$$\frac{dP_r(t)}{dt} = f(Q_r(t) - Q_r^0, \dot{q}_v(t) - \dot{q}_r(t), C_r(t), \dots) + \frac{dP_{th}(t)}{dt} \quad (2.22)$$

$$\frac{dP_{pa}(t)}{dt} = \frac{\dot{q}_r(t) - \dot{q}_{pa}(t)}{C_{pa}} + \frac{dP_{th}(t)}{dt} \quad (2.23)$$

$$\frac{dP_{pv}(t)}{dt} = \frac{\dot{q}_{pa}(t) - \dot{q}_{pv}(t)}{C_{pv}} + \frac{dP_{th}(t)}{dt}, \quad (2.24)$$

where $f(\cdot)$ is given in Appendix A, and

$$\dot{q}_l(t) = \begin{cases} \frac{P_l(t)-P_a(t)}{R_l} & P_l(t) > P_a(t) \\ 0 & \text{otherwise} \end{cases} \tag{2.25}$$

$$\dot{q}_a(t) = \frac{P_a(t) - P_v(t)}{R_a} \tag{2.26}$$

$$\dot{q}_v(t) = \begin{cases} \frac{P_v(t)-P_r(t)}{R_v} & P_v(t) > P_r(t) \geq 0 \\ \frac{P_v(t)}{R_v} & P_v(t) > 0 > P_r(t) \\ 0 & \text{otherwise} \end{cases} \tag{2.27}$$

$$\dot{q}_r(t) = \begin{cases} \frac{P_r(t)-P_{pa}(t)}{R_r} & P_r(t) > P_{pa}(t) \\ 0 & \text{otherwise} \end{cases} \tag{2.28}$$

$$\dot{q}_{pv}(t) = \begin{cases} \frac{P_{pv}(t)-P_l(t)}{R_{pv}} & P_{pv}(t) > P_l(t) \\ 0 & \text{otherwise} \end{cases} \tag{2.29}$$

with $\dot{q}_{pa}(t)$ given in Equations (2.7)-(2.9).

The six compartmental pressures are state variables which succinctly summarize all the past dynamical information necessary for determining future time evolution. That is, if we know what the six pressures are at time t^0, then we may determine the time evolution of these pressures, as well as the volumes (through Equation (2.1) and a numerical search for the ventricular volumes) and flow rates (through Equations (2.25)-(2.29) and Equations (2.7)-(2.9)) of the model, for all $t > t^0$. This may be realized with a computer by discretizing Equations (2.19)-(2.24) and integrating these equations at each ensuing discrete time step in an iterative fashion. But, before we present the precise numerical integration technique that we employ, we first describe a method for determining an initial set of pressures.

2.3.3 Initial Conditions

The six initial pressures are determined from the approach implemented by the original CVSIM model [23]. This approach considers the average pressures in the systemic

and pulmonary compartments and the end-diastolic pressures in the ventricular compartments, for a given set of model parameters, to be a reasonable choice for the initial pressures. These pressures, as well as the end-systolic pressures in the ventricular compartments, are determined from the solution of a system of linear equations which are formulated based on conservation laws during static model conditions (*e.g.*, static linear capacitors are considered to be open-circuits). The system of linear equations are given as follows:

$$\begin{aligned} & C_l^{ed}(P_l^{ed}-P_{th}) - C_l^{es}(P_l^{es} - P_{th}) \\ & \quad = C_r^{ed}(P_r^{ed} - P_{th}) - C_r^{es}(P_r^{es} - P_{th}) && (2.30) \\ & \quad = T_s\frac{P_l^{es} - P_a}{R_l} && (2.31) \\ & \quad = T\frac{P_a - P_v}{R_a} && (2.32) \\ & \quad = T_d\frac{P_v - P_r^{ed}}{R_v} && (2.33) \\ & \quad = T_s\frac{P_r^{es} - P_{pa}}{R_r} && (2.34) \\ & \quad = T\frac{P_{pa} - P_{pv}}{R_{pa}} && (2.35) \\ & \quad = T_d\frac{P_{pv} - P_l^{ed}}{R_{pv}} && (2.36) \end{aligned}$$

$$\begin{aligned} Q_{total} - Q_{total}^0 = {} & C_l^{ed}(P_l^{ed} - P_{th}) + C_a(P_a - \frac{1}{3}P_{th}) + C_vP_v \\ & + C_r^{ed}(P_r^{ed} - P_{th}) + C_{pa}(P_{pa} - P_{th}) + C_{pv}(P_{pv} - P_{th}). \end{aligned} \quad (2.37)$$

Equations (2.30)-(2.36) may be thought of as representing the conservation of flow rate in which the average stroke volume generated by each ventricle (as determined by the difference in end-diastolic volume and end-systolic volume; Equation (2.30)) is set equal to each other as well as the average volume of blood that passes through each of the six resistors during a cardiac cycle (as determined by the product of the average flow rate with the time period of flow in the cardiac cycle; Equations (2.31)-(2.36)). Equation (2.37) may be thought of as a conservation of volume equation in which the sum of the compartmental volumes responsible for generating pressure (stressed

volume) must equal the total stressed blood volume[7].

Since our modified CVSIM model incorporates nonlinear elements, this system of linear equations is no longer strictly applicable. However, these equations are a reasonable approximation to our modified model, especially with regard to the equations reflecting the static performance of the ventricles which are essentially linear for most sets of considered model parameters. Hence, we utilize this relatively simple approach to obtain a reasonable set of initial pressures.

2.3.4 Numerical Integration

The numerical integration technique that we employ is the same fifth-order Runge-Kutta method with adaptive step size that is implemented by the original CVSIM model (see [23, 69] for a detailed description of the algorithm). The adaptive step size feature implies that the pressures, flow rates, and volumes determined from integration are nonuniformly sampled in time with fine sampling during systole in which the system dynamics are fast (especially ventricular outflow which is characterized by short time constants of 0.002 s) and coarse sampling during diastole when the system dynamics are slower (ventricular outflow diodes are open). This type of almost optimal sampling scheme has proven to perform well in terms of accuracy and speed. We utilize this numerical integration technique for the computer implementation of all the variants of the nominal model considered in this thesis. Hence, in order to describe the computer implementation of each of these variants, we need only to specify the governing state-space equations and a linear system of equations whose solution provides an initial set of pressures.

[7]Since one-third of the the systemic arteries reside in the thoracic compartment, the reference pressure of the systemic arterial compartment is given here as $\frac{1}{3}P_{th}$.

2.4 Nominal Model Validation

We now demonstrate that the nominal model of the heart and circulation presented in Sections 2.1-2.3 is capable of exhibiting reasonable hemodynamic behaviors. We begin, in Section 2.4.1, by illustrating the steady-state, pulsatile waveforms generated by the model. Then, in Sections 2.4.2 and 2.4.3, we describe a static analysis of the systemic circulation model and the heart-lung unit model and show that the results of these analyses compare well with experimental data. Next, in Section 2.4.4, we discuss how the static analyses may also be useful for the purposes of teaching. Finally, in Section 2.4.5, we present an analysis of the effect of heart rate changes on steady-state left ventricular flow rate (cardiac output, CO) in order to demonstrate the validity of model dynamics particularly over the range of heart rates considered by the identification methods in Part II.

2.4.1 Pulsatile Analysis

The original CVSIM model generates three pulsatile waveforms (pressure, volume, and flow rate) for each of its six compartments. These waveforms, in the steady-state, were shown to be similar to catheterization data published in the literature [23]. We reiterate that by similar, we mean that the gross or average waveforms are about the same, while details from, for example, distributed or inertial effects are neglected. The nominal heart and circulatory model presented here also generates pulsatile pressure, volume, and flow rate waveforms for each of its six compartments. These waveforms (Figures 2-5 and 2-6), despite the modifications made in Sections 2.3.1 and 2.2, appear to be essentially the same as the waveforms generated by the original CVSIM model. The most significant difference is that the right ventricular waveforms here more accurately reflect rapid diastolic filling due to the modification of the original CVSIM parameter values. However, these modifications would substantially alter the pulsatile

waveforms if we were to consider a set of parameter values that would move the model operating point to the limits of its dynamical range. The modifications also have a pronounced effect on low frequency changes in the pulsatile waveforms. For example, the low frequency changes in $P_{pa}(t)$ would be damped due to the incorporation of the nonlinear pulmonary arterial resistor.

Figure 2-5 Time evolution of pressures, volumes, and flow rates generated by the nominal heart and circulatory model.

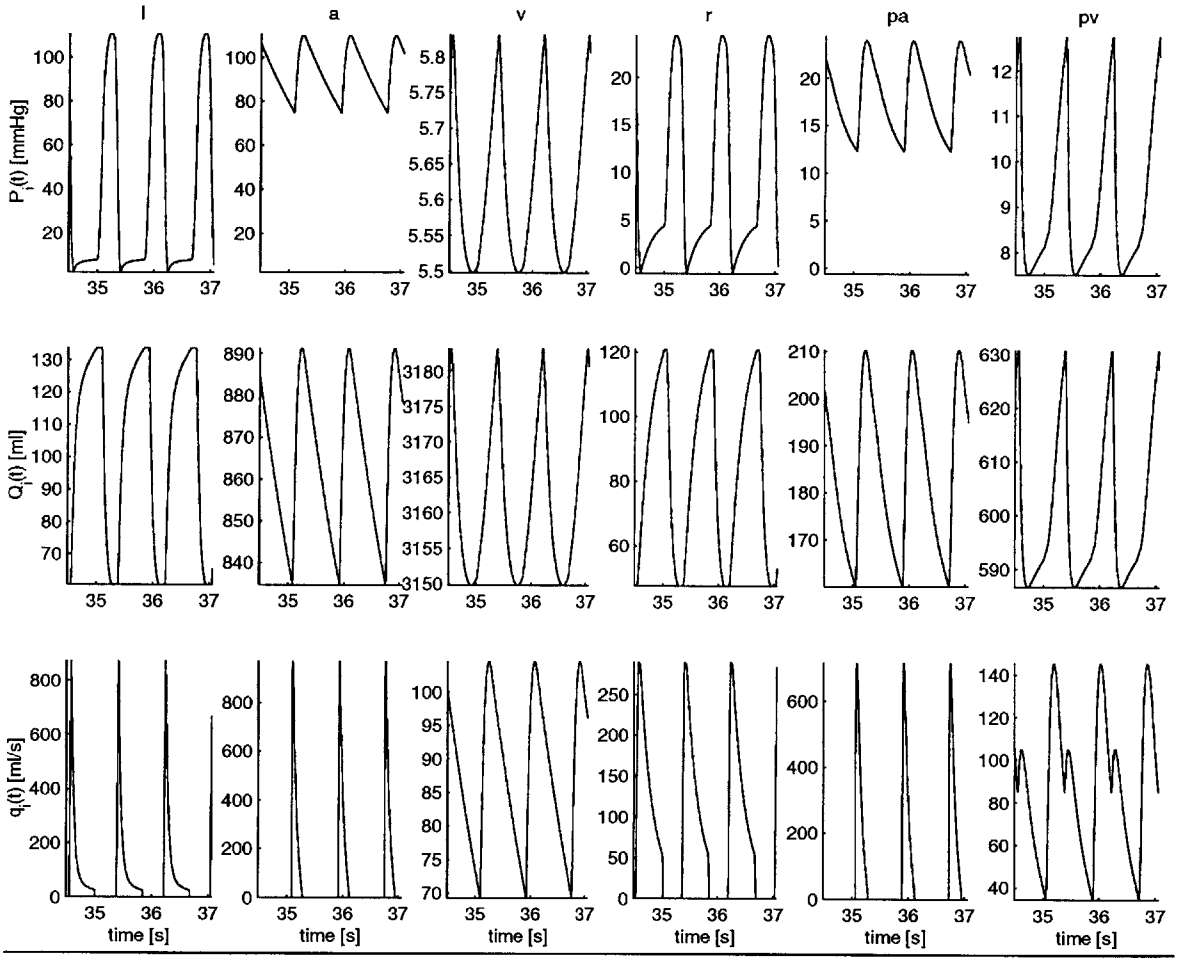

2.4.2 Static Analysis of the Systemic Circulation Model

The systemic circulation may be considered in electrical terms as a two-terminal device in which one terminal is represented by the right atrium and the other, by the aorta. A meaningful static analysis of the systemic circulation may then amount to the

Figure 2-6 (a) Left ventricular and (b) right ventricular pressure-volume loops generated by the nominal heart and circulatory model.

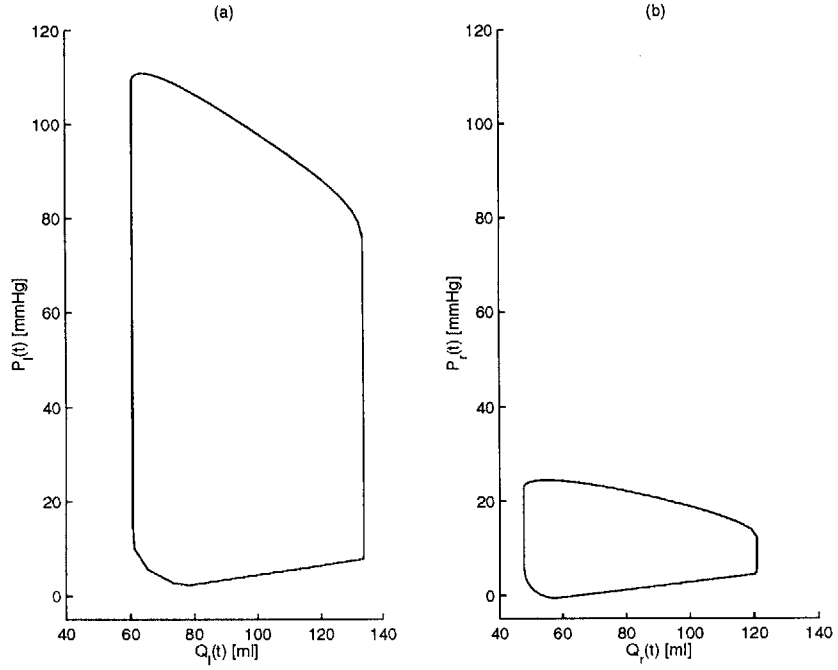

determination of its static "i-v" characteristics at these terminals. In hemodynamic terms, this involves determining the effects of the mean aortic pressure and mean right atrial pressure on the mean flow rate, while the parameters of the systemic circulation are held constant. We specifically consider the static, two-terminal analysis of Guyton of which experimental results are readily available in the literature [32, 33].

Guyton's analysis essentially involves the determination of the influence of mean right atrial pressure on mean flow rate to the right heart (venous return), while the parameters of the systemic circulation are maintained. Since one of the maintained parameters is the mean systemic pressure (P_{ms}, total stressed blood volume of the systemic circulation normalized by the total systemic compliance), mean aortic pressure is completely specified from mean venous return and mean right atrial pressure. Hence, a plot of mean venous return as a function of mean right atrial pressure, which is referred to as Guyton's venous return curve, completely characterizes the systemic circulation for a given circulatory state. Figure 2-7a illustrates averaged, experimen-

tal venous return curves from 12 control dogs and 14 dogs in which the circulatory state was maintained by total spinal anesthesia and continuous epinephrine drip [33]. The curves show that as the mean right atrial pressure decreases, the mean venous return increases. This is expected, since the mean right atrial pressure acts as a backward force on the veins impeding blood flow into the right heart. However, the mean venous return eventually plateaus as mean right atrial pressure decreases to zero due to systemic venous collapse (see Section 2.2.1).

Figure 2-7 (a) Averaged venous return curves obtained from dog preparations during control conditions and total spinal anesthesia with continuous epinephrine drip [33]. (b) Model venous return curve obtained from the model preparation in Figure 2-8.

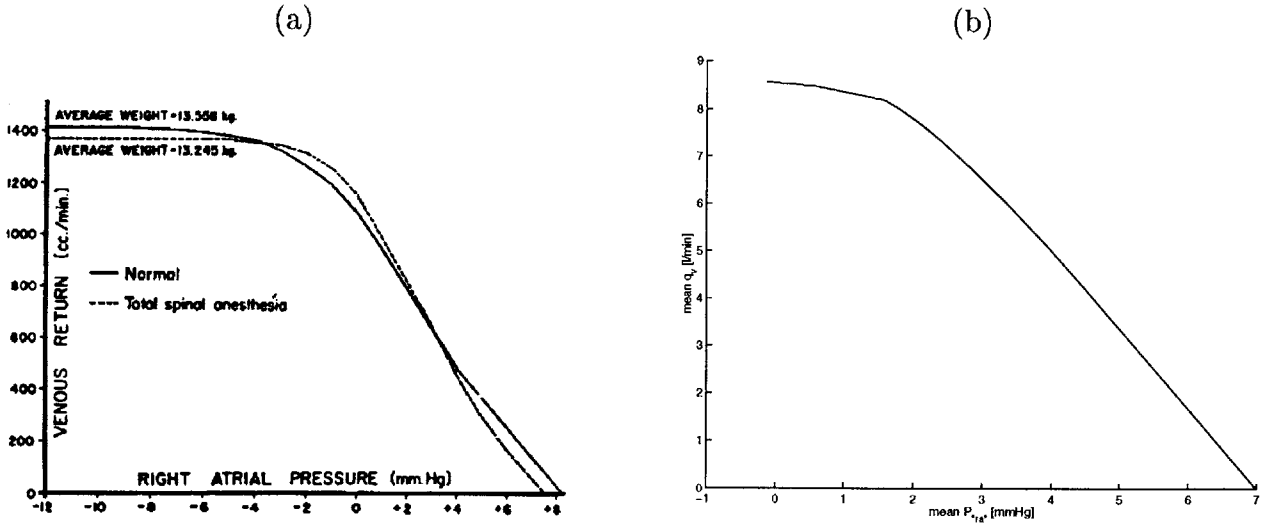

In order to perform Guyton's analysis on the model, we must first define suitable terminals as the model does not have a right atrium. We choose the two bold nodes in Figure 2-1 as these terminals. The bold node labelled $P_{\text{“}ra\text{”}}(t)$ is the location of where the right atrium would be if we had included it in the model. The pressure at this node is defined as follows:

$$P_{\text{“}ra\text{”}}(t) = \begin{cases} P_v(t) & P_v(t) \leq P_r(t) \\ P_r(t) & P_r(t) > P_v(t) \end{cases} . \tag{2.38}$$

Analogous to actual right atrial pressure, this pressure reflects the backward force impeding blood flow into right heart; however, it overestimates actual right atrial pressure with the extent of overestimation increasing with heart rate. With the two terminals defined, we are now left with the design of the model experiment.

We are interested in a meaningful analysis of the static terminal characteristics of the systemic circulation which would permit the determination of the mean venous return in the intact circulation from the mean right atrial pressure. However, since Guyton's analysis involves maintaining P_{ms}, this precludes the possibility of performing a model experiment on the intact circulation. We must instead consider a model experiment in which a controllable load is applied to the terminals of the systemic circulatory model. Since the systemic circulatory model is nonlinear, it is important to realize that the venous return curve that we obtain will be dependent on the type of load that is chosen. Hence, we consider a load that closely resembles the load seen by the systemic circulation in the intact circulation. The model in Figure 2-8 depicts our model preparation for performing Guyton's analysis. Since pulmonary ABP is fairly constant (Section 2.2.2), the load here is quite close to that seen in the intact circulation. Note that the independent current source here serves to keep P_{ms} precisely constant by pumping into the systemic circulation what ever is pumped out.

The state equations governing the model in Figure 2-8 are given by Equations (2.20)-(2.22) and Equations (2.26)-(2.28) with $\dot{q}_r(t)$ and constant P_{pa} substituted for $\dot{q}_l(t)$ and $P_{pa}(t)$, respectively. Here, P_{pa} is specifically chosen to be the nominal end-systolic pulmonary ABP of the intact circulation. The initial set of pressures are determined

Figure 2-8 Model systemic circulation preparation for determining Guyton's venous return curve where a box indicates a nonlinear element (Sections 2.2.1 and 2.2.3).

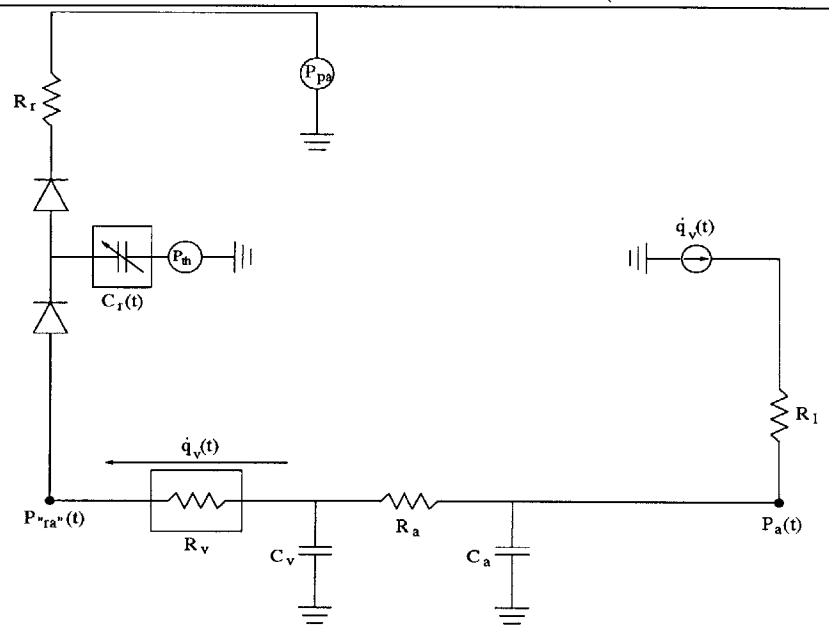

through solution of the following linear system of equations:

$$C_r^{ed}(P_r^{ed} - P_{th}) - C_r^{es}(P_r^{es} - P_{th}) = T_s \frac{P_r^{es} - P_{pa}}{R_r} \tag{2.39}$$

$$= T_d \frac{P_v - P_r^{ed}}{R_v} \tag{2.40}$$

$$= T \frac{P_a - P_v}{R_a} \tag{2.41}$$

$$C_a P_a + C_v P_v = (C_a + C_v) P_{ms}, \tag{2.42}$$

where P_{pa} and P_{ms} are known parameters and P_r^{ed}, as opposed to P_r^{es}, is again considered to be the initial right ventricular pressure. Equations (2.39)-(2.41) reflect conservation of flow rate analogous to Equations (2.30)-(2.36), while Equation (2.42) ensures that the mean systemic pressure is initially set to P_{ms}. The experiment may then be performed by simply adjusting C_r^{ed} in order to vary $P_{\text{“}ra\text{”}}(t)$ and measuring the mean $\dot{q}_v(t)$.

Figure 2-7b shows that the resulting venous return curve from the model experiment qualitatively matches the actual experimental result in Figure 2-7a. From a quantitative point of view, aside from the mean right atrial pressure being overesti-

mated, the venous return curve appears to be somewhat enhanced with respect to extrapolated human values from animal experimentation [32]. It turns out that if we assigned the original CVSIM parameter values to the nominal heart and circulatory model, we would have a more quantitatively accurate venous return curve. However, the small sacrifice made here permits more realistic dynamical behavior (see Section 2.4.5).

Although we have incorporated a piece-wise linear model of the collapsible veins (Section 2.2.1), we obtain a smoothed venous return curve from our model. This smoothing is due to the monotonically increasing fraction of time that the collapsible vein model spends in the waterfall condition as the mean right atrial pressure decreases (Section 2.2.1). However, the smoothing in the venous return curve of Figure 2-7a is probably also due to the monotonically increasing number of collapsible veins in the waterfall condition as mean right atrial pressure decreases as well as smooth pressure-flow rate curves characterizing each of the collapsible veins.

2.4.3 Static Analysis of the Heart-Lung Unit Model

The heart and pulmonary circulation may be considered to be a single pumping unit responsible for providing oxygenated blood to the systemic circulation. This pumping unit, which is referred to as the heart-lung unit, may also be thought of in electrical terms as a two terminal device with the terminals again being the right atrium and aorta. The pressure in the right atrium is considered to be the input pressure (preload) to the heart-lung unit, while the pressure in the aorta is the output pressure (afterload) against which the unit pumps. A static pressure-flow rate analysis of this pumping unit would amount to determining the simultaneous effects of mean aortic pressure and mean right atrial pressure on mean CO (aortic flow rate), while the parameters of the heart-lung unit are held constant.

Figure 2-9a illustrates the averaged, experimental result from 25 dogs in which the

parameters of the heart-lung unit were held constant by surgical elimination of reflex control [36]. This result clearly shows the limiting behavior of the heart-lung unit in terms of a maximum aortic flow rate and a maximum aortic pressure against which the unit can pump blood. The plot also indicates that the mean aortic flow rate is essentially independent of mean aortic pressures up to about 180 mmHg. Within this aortic pressure limit, the plot of mean aortic flow rate as a function of mean right atrial pressure, which is referred to as Guyton's CO curve, completely characterizes static terminal flow rate behavior of the heart-lung unit [32].

Figure 2-9 (a) Averaged family of CO curves obtained from 25 dog heart-lung preparations in which reflex control was eliminated surgically [36]. MAP and MRAP respectively denote mean aortic and right atrial pressures. (b) Model result obtained from model preparation in Figure 2-10.

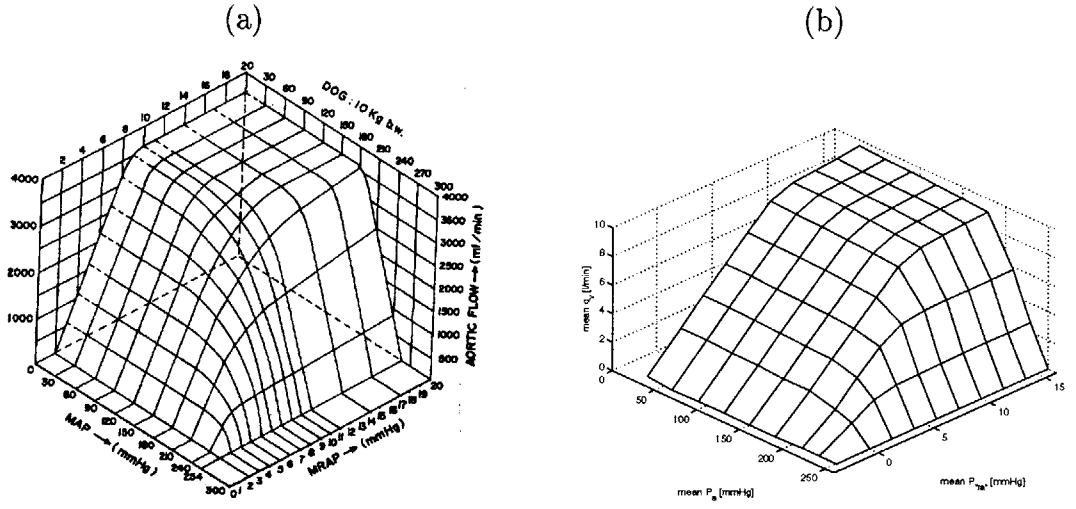

In order to perform this analysis on our model, we again consider the two bold nodes in Figure 2-1 as the two terminals of the heart-lung unit. We obtain complete control of the pressures at these terminals, by removing the systemic arterial and venous capacitors from our model and replacing them with independent voltage sources as in Figure 2-10[8]. The state equations characterizing the model here

[8]The choice of this preparation was again based on obtaining a load which nearly resembles that

are given by Equations (2.19), (2.22)-(2.24) and Equations (2.7)-(2.9),(2.25), (2.28)-(2.29) with constant P_a and P_v in place of $P_a(t)$ and $P_v(t)$, respectively. The initial set of pressures are determined through solution of the system of linear equations given by Equations (2.30)-(2.31), (2.33)-(2.36) in which P_a and P_v are assumed to be known and the end-diastolic ventricular pressures are again considered to be the initial ventricular pressures.

Figure 2-10 Model heart-lung preparation where a box indicates a nonlinear element (Sections 2.2.1 - 2.2.3).

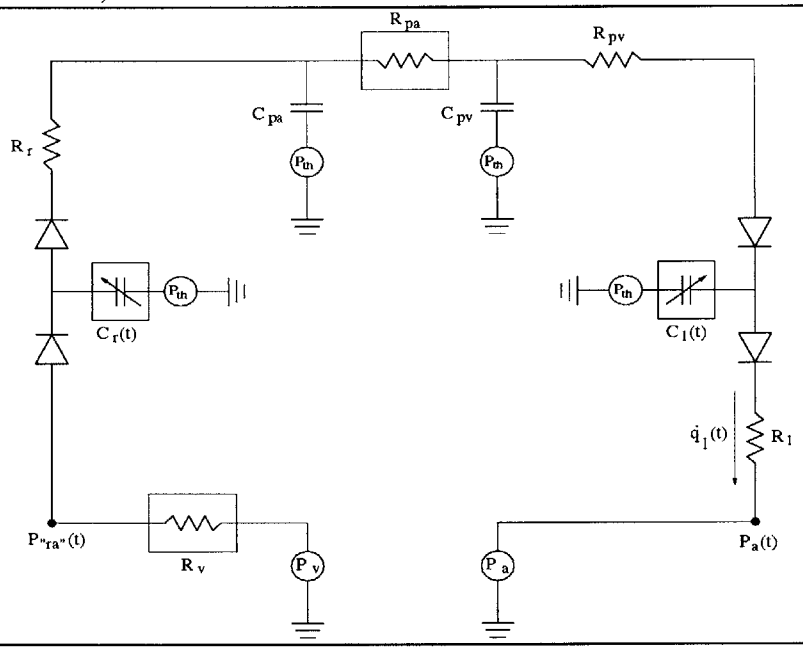

The static analysis may then be performed by varying the two independent voltage sources and calculating the resulting mean $\dot{q}_l(t)$. These voltage sources permit precise control of P_a but not $P_{\text{“}ra\text{”}}$. However, it is possible to set this latter pressure to a desired value with arbitrary accuracy by simply adjusting P_v according to the well-known bisection method [69]. This method essentially involves first choosing two values of P_v which bracket the P_v that produces the desired mean "right atrial" pressure and then halving the bracket in an iterative fashion until the desired accuracy is reached.

seen in the intact circulation.

Figure 2-9b shows the results of this model experiment. From a qualitative point of view, this result matches fairly well with the experimental result in Figure 2-9a. From a quantitative point of view, aside from the mean right atrial pressure being overestimated, the results appear to be somewhat depressed with respect to extrapolated human values from animal experimentation [32]. This slight depression offsets the somewhat enhanced venous return curve in Section 2.4.2 so as to provide reasonable hemodynamic values during normal operating conditions (see Section 2.4.4).

2.4.4 Guyton's Analysis

Guyton's CO and venous return curves provide a complete static characterization of the state of the heart and circulation, and their intersection provides the mean CO and right atrial pressure that would result at this state. These curves provide a useful tool for understanding the factors controlling CO. [32]. For example, if one knows how a particular factor (*e.g.*, heart rate) alters the curves, then one can easily understand how this factor influences CO as well as mean right atrial pressure. Figure 2-11 illustrates that the intersection of the model CO and venous return curves obtained from the heart-lung unit and systemic circulation at their nominal states indeed predicts the actual mean CO and mean "right atrial" pressure resulting from the intact circulation at this nominal state. Figure 2-11 also illustrates how a decrease in heart rate from its nominal value of 72 bpm to 50 bpm would change the mean CO and "right atrial" pressure. Although these model curves slightly deviate from human curves extrapolated from animal experimentation [32], importantly, the alterations in the model curves in response to changes in cardiovascular state, such as that illustrated in the figure, are reasonable (see Section 2.4.5). Thus, the nominal heart and circulatory model may also serve as an improved tool for teaching hemodynamics.

Figure 2-11 Model examples of Guyton's CO and venous return curve analysis [32]. The blue curves represent the nominal cardiovascular state, while the red curve reflects how the CO curve would change in response to a decrease in heart rate from 72 bpm to 50 bpm. The intersections of these curves represent what $< \dot{q}_l >$ and $< P_{\text{“}ra\text{”}} >$ would have been in the intact circulation of the same state. For example, from the nominal, intact circulation, mean $\dot{q}_l = 5.25$ l/min and mean $P_{\text{“}ra\text{”}} = 3.82$ mmHg.

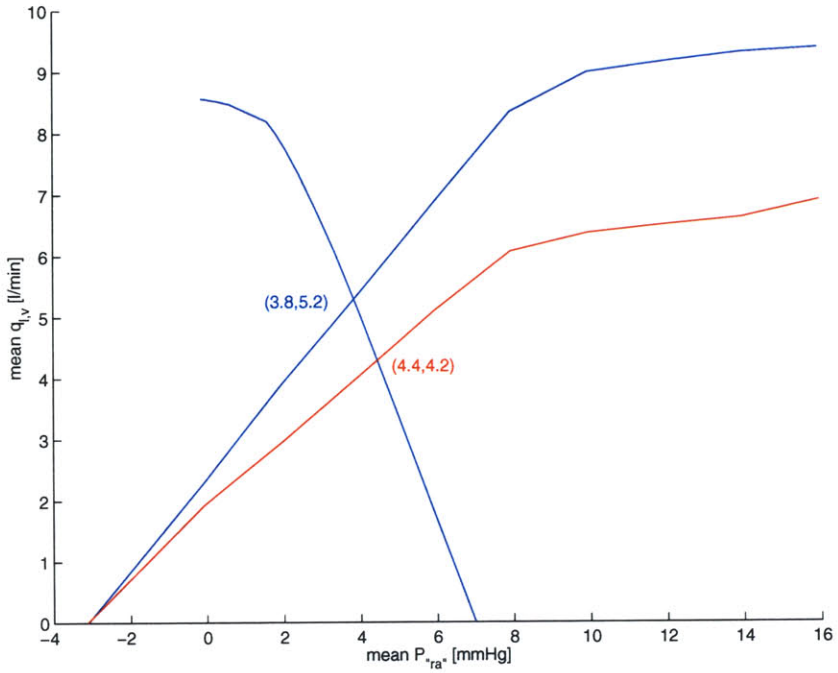

2.4.5 Analysis of Heart Rate Effects on CO

We now demonstrate the validity of the dynamical properties of the model through an analysis of the effect of heart rate changes on steady-state CO. Figure 2-12a illustrates experimental data obtained from an anesthetized dog preparation in which mean CO is plotted as a function of heart rate. These data demonstrate that CO increases with heart rate until the heart rate is sufficiently fast such that the diastolic filling time compromises stroke volume. From Guyton's point of view, the data demonstrate that heart rate is able to increase CO through enhancement of the CO curve until the venous return curve is saturated. Figure 2-12b illustrates that the corresponding data, which is obtained from the nominal model (blue trace) through the variation of T, emulates the experimental data particularly at heart rates less

than ~100 bpm. At higher heart rates, the model is not as accurate with respect to experimental data due to its enhanced venous return curve. In Figure 2-12b, we also include the corresponding data obtained from the model with the original CVSIM parameter values (red trace). Since these parameter values were geared towards the accurate representation of the venous return curve, the red trace emulates the experimental data at heart rates greater than ~100 bpm. However, the red trace is grossly inaccurate for heart rates less than ~100 bpm, because the parameter values completely sacrifice the performance of the heart-lung unit. Although it is not possible to emulate perfectly the experimental data in Figure 2-12a over the entire heart rate range without a right atrium, the nominal heart and circulatory model appears to be quite adequate particularly over the range of heart rates considered by the identification methods in Part II.

Figure 2-12 (a) Experimental data reflecting the effects of heart rate on steady-state CO. The data are obtained from an anesthetized dog preparation during atrial pacing [10]. (b) Forward model data reflecting the effects of heart rate on steady-state CO for the nominal parameter values of Table 2.1 (blue trace) and the original CVSIM parameter values (red trace). These data are obtained through variation of T only up to heart rates of 150 bpm, since the forward model is not expected to behave appropriately at very high heart rates due to the omission of atria.

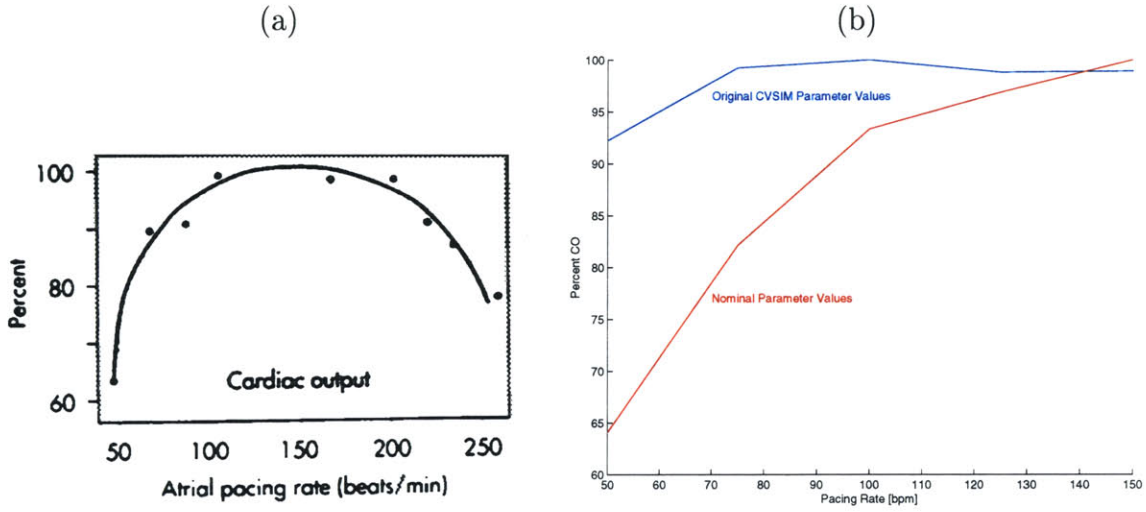

2.5 Set of Robustness Models

In this section, we present a set of more complex heart and circulatory models which are derived through modification of the nominal model. The modifications that we specifically consider are geared towards more accurately representing the systemic arterial compartment which invariably involves increasing its complexity. The performance of the cardiovascular system identification method analyzed in Chapter 5 is relatively insensitive to the forward modeling of the systemic arterial compartment; however, this may not necessarily be the case for the identification methods considered in Chapters 6 and 7. Hence, the specific purpose of this set of more complex models is to assess the robustness of the latter identification methods against more realistic systemic arterial compartments. In Section 2.5.1, we first present a nonlinear systemic arterial compliance model. Then, in Section 2.5.2, we describe a linear, third-order model of the systemic arterial compartment which may also incorporate the nonlinear model.

2.5.1 Nonlinear Systemic Arterial Compliance

The nonlinearity of the lumped systemic arterial compliance has been extensively investigated (see, for example, [13, 30, 34, 46]). These studies have generally demonstrated that the systemic arterial compliance decreases significantly with large increases in ABP. For example, consider Figure 2-13 which illustrates the pressure-volume relationships characterizing human aortas obtained at autopsy [34]. The data here not only implies the consideration for differential compliances but also leads to the intuitive notion of a maximum volume that the systemic arterial compartment can hold. The data in the figure further demonstrate the well known concept that the systemic arterial compliance decreases with age. However, we are primarily interested in these pressure-volume relationships only over the more limited range considered

in cardiovascular system identification, in which case, a linear systemic arterial compliance seems to be a reasonable first-order approximation. In fact, an identification method that we present in Section 6.2.4 is based on this very assumption of linearity. Hence, we consider here a nonlinear systemic arterial compliance model against which the robustness of this identification method may be assessed.

Figure 2-13 Pressure-volume relationships of aortas obtained from humans of varying ages at autopsy [34].

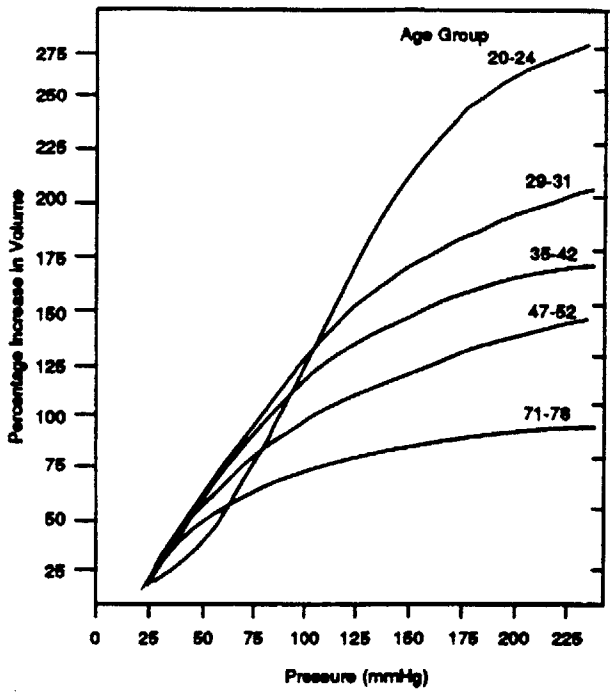

The nonlinear model of the systemic arterial compliance that we implement for our robustness analysis is mathematically represented in terms of its pressure-volume relationship as follows:

$$Q_a(t) = (Q_a^{max} - Q_a^0)(1 - \mathrm{e}^{-\delta P_a(t)}) + Q_a^0, \tag{2.43}$$

where Q_a^{max} represents the maximum possible systemic arterial volume and δ is a positive constant. We may determine the differential compliance as a function of

ABP by taking the derivative of this equation with respect to $P_a(t)$, which results in the following equation:

$$C_a(P_a(t)) = \delta(Q_a^{max} - Q_a^0)\mathrm{e}^{-\delta P_a(t)}. \tag{2.44}$$

Note that the compliance in this model does indeed decrease with increasing ABP. In fact, the functional form of this equation has been previously considered to characterize the lumped systemic arterial compliance [30, 46]. The extent of nonlinearity is reflected in the curvature ($K(P_a(t))$) of the pressure-volume relationship which may be determined by taking the second derivative of Equation (2.43) with respect to $P_a(t)$ and is given as follows:

$$K(P_a(t)) = -\delta^2(Q_a^{max} - Q_a^0)\mathrm{e}^{-\delta P_a(t)}. \tag{2.45}$$

The model here is parametrized by three variables (Q_a^{max}, Q_a^o, and δ) which provide the minimum degrees of freedom necessary to set the volume, differential compliance, and differential curvature of the pressure-volume relationship at a given operating point ABP to desired values. This may be specifically accomplished by simply inverting Equations (2.43)-(2.45), which results in the following set of equations:

$$\delta = -\frac{K_d}{C_d} \tag{2.46}$$

$$Q_a^{max} = Q_d - \frac{C_d^2}{K_d} \tag{2.47}$$

$$Q_a^0 = Q_d + \frac{C_d^2}{K_d}\mathrm{e}^{-\frac{K_d P_a^{sp}}{C_d}}(1 - \mathrm{e}^{\frac{K_d P_a^{sp}}{C_d}}), \tag{2.48}$$

where the subscript d denotes the desired values and the superscript sp is an abbreviation for setpoint (operating point). Hence, the model here may provide a useful tool for assessing the independent influences of variations in volume, compliance, or curvature on the identification method.

As we have stated, the primary motivation for the model here is to investigate the robustness of the identification method presented in Section 6.2.4 against nonlinearity which may be characterized by the curvature. Curvature has been experimentally investigated in open-chest anesthetized dog preparations in terms of the percentage change in systemic arterial compliance over the cardiac cycle (with respect to the maximum compliance during the cardiac cycle) which was estimated to be about 5-15% [46]. In the model, this percentage change in compliance may be expressed mathematically as $1 - e^{\frac{K_d}{C_d}PP}$, where PP represents the pulse pressure of the cardiac cycle. Hence, we now have a simple prescription for performing a robustness analysis against realistic curvatures. In particular, we consider the percentage change from 5% to 25% (assuming error in the experimental estimates) in increments of 10%. The expression representing the percentage change is altered by only adjusting K_d while holding $Q_d = C_a P_a^{sp} + Q_a^0$ and $C_d = C_a$, where C_a and Q_a^0 represent the linear parameter values provided in Table 2.1 and P_a^{sp} represents the setpoint ABP given in Table 3.1[9]. Figure 2-14 illustrates the resulting pressure-volume and differential compliance curves which are utilized for the well controlled robustness analysis in Section 6.4. Note that the form of the curves in Figure 2-14a resemble that in Figure 2-13.

The state equations governing the heart and circulatory model with the nonlinear systemic arterial compliance here are given by Equations (2.19)-(2.24) in which Equation (2.20) is replaced by the following equation:

$$\frac{dP_a(t)}{dt} = \frac{\dot{q}_l(t) - \dot{q}_a(t)}{\delta(Q_a^{max} - Q_a^0)e^{-\delta P_a(t)}}. \tag{2.49}$$

This equation is determined from the derivative of Equation (2.43) with respect to t and KCL. The initial set of pressures may also be determined from solution of Equations (2.30)-(2.37) in which the systemic arterial compliance is considered to be

[9] PP may be approximated from the average pulse pressure generated by the linear systemic arterial compliance model.

Figure 2-14 (a) Nonlinear pressure-volume relationships of the systemic arteries along with (b) their corresponding differential compliance curves against which the identification method presented in Section 6.2.4 is assessed.

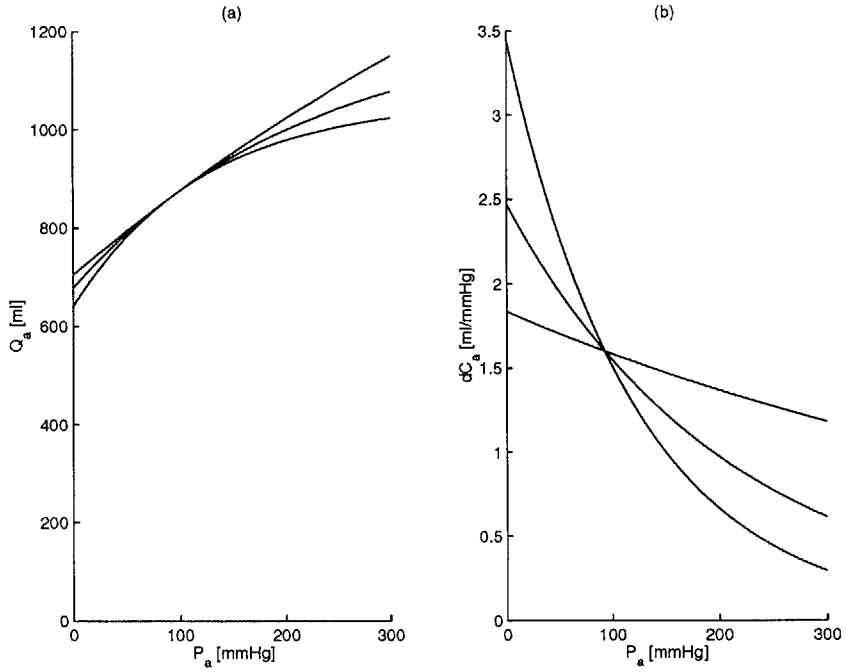

perfectly linear and set equal to $\delta(Q_a^{max} - Q_a^0)\mathrm{e}^{-\delta P_a^{sp}}$.

2.5.2 Third-Order Systemic Arterial Compartment Model

The arterial pulse contour changes significantly as we consider it at different points in the arterial system. In particular, as we move further away from the heart, the systolic upstroke becomes steeper, more narrow, and achieves a greater maximum pressure, while a hump in the diastolic downstroke becomes more prominent[10]. These changes are due to wave phenomena supported by the distributed nature of the arterial system. Despite this fact, our nominal, lumped parameter model of the systemic arterial compartment provides an accurate representation of the pulse contour at the aorta (with the exception of the high frequency dicrotic notch). This may be explained by

[10]The high frequency components of the pulse contour also diminish (*e.g.*, dicrotic notch) as we move further away from the heart due to viscous effects. However, these effects are generally considered to be relatively small in the arterial system.

arguments made by Noordergraaf [60] as follows. The arterial system is a branching collection of tapered vessels with varying elastic properties. A wave reflection can occur not only at its point of termination (systemic microcirculation which represents a high impedance load responsible for positive wave reflections) but also at any point within the arterial system where its properties change (*e.g.*, change in vessel compliance or vessel bifurcation). The complexity of the reflection sites as well as their varying distances from the aorta result in reflected waves with large phasic differences which generally tend to mitigate the cumulative effects of these waves (destructive interference). However, the large phasic differences become less significant when considering reflected waves with long wavelengths (manifested as low frequency temporal changes in the ABP waveform). Thus, these waves add constructively and are actually felt by the aorta. The important point is that these wavelengths are long with respect to the dimension of the arterial system such that the arterial system behaves as a single blood reservoir (capacitor). Noordergraaf's arguments also allow us to conclude that our lumped parameter model provides an accurate representation of the low frequency components of peripheral arterial pressures, even though it is not valid for the high frequency pulsatile components.

Since the identification methods in Part II primarily consider only low frequency fluctuations, our nominal model of the systemic arterial compartment seems to be adequate for any particular site in the arterial system. However, we present an identification method in Chapter 7 that considers the pulsatile components as well. In order to evaluate the application of this method to peripheral ABP waveforms (which are more readily available from measurement), we include here a model of the systemic arterial compartment that is capable of emulating these waveforms. Since the construction of distributed models is beyond the scope of this thesis, we must resort to a more complex, lumped parameter model. Fortunately, such models have proven to be able to account for much of the peripheral arterial pulse contour,

especially their diastolic portions [18,60]. As will be implied in Chapter 7, accurate representation of the diastolic portion of the peripheral ABP waveform is most critical for our purposes.

As we have discussed, from the perspective of the aorta, the systemic arterial compartment appears to consist of a single, lumped capacitor. However, from the perspective of a peripheral artery, the blood is stored throughout the arterial system, from the large, elastic arteries to the smaller, muscular arteries. Hence, we particularly consider the lumped parameter model in Figure 2-15 which consists of two capacitors reflecting the central, elastic (e) and peripheral, muscular (m) arteries separated by an inductor (L) representing the inertial effects of moving blood between these compartments. This model has previously been demonstrated to represent accurately the diastolic portions of the radial arterial pulse [18]. Furthermore, the model here is intuitively pleasing in terms of its limiting behaviors. The model exhibits sustained oscillations when $R_a \to \infty$. Theoretically, this is what one might expect in the actual distributed arterial system, because the wave at its terminal point would be reflected back perfectly with an infinite impedance load. This theory is supported by experimental studies in which the magnitude of the diastolic hump was found to increase with peripheral resistance [18]. Additionally, the model behaves like a single lumped capacitor with compliance $(C_e + C_m)$ in parallel with a resistor as the considered frequencies tend to zero.

The precise dynamics of the model may be determined from its characteristic equation which is given as follows:

$$\lambda^3 + \frac{1}{R_a C_m}\lambda^2 + \frac{C_e + C_m}{C_e C_m L_e}\lambda + \frac{1}{R_a C_e C_m L_e} = 0. \tag{2.50}$$

Hence, the impulse response ($h(t)$) characterizing this model as well as the diastolic decay may take on three different forms depending on the roots of the characteristic equation. However, only one of these three forms has proven to reflect accurately the

Figure 2-15 Third-order model of the systemic arterial compartment for the purposes of emulating peripheral ABP waveforms.

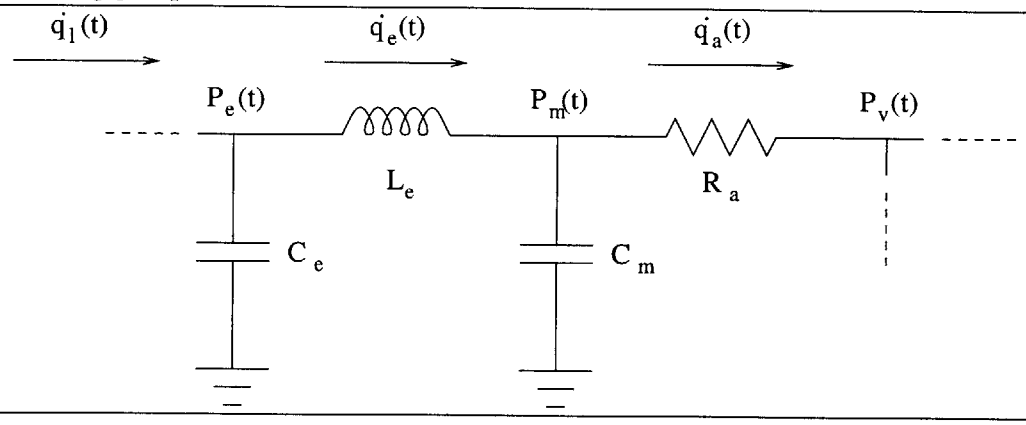

diastolic decay [18] and this form is given as follows:

$$h(t) = A_1 e^{\frac{-t}{\tau_1}} + 2|A_2| e^{\frac{-t}{\tau_2}} \cos(\omega_1 t + \angle A_2), \tag{2.51}$$

where the unknown terms here may be determined from the model parameters [18].

The governing state equations of the model in Figure 2-15 are given as follows:

$$\frac{dP_e(t)}{dt} = \frac{\dot{q}_l(t) - \dot{q}_e(t)}{C_e} \tag{2.52}$$

$$\frac{dP_m(t)}{dt} = \frac{\dot{q}_e(t) - \dot{q}_a(t)}{C_m} \tag{2.53}$$

$$\frac{d\dot{q}_e(t)}{dt} = \frac{P_e(t) - P_m(t)}{L_e} \tag{2.54}$$

where

$$\dot{q}_l(t) = \begin{cases} \frac{P_l(t) - P_e(t)}{R_l} & P_l(t) > P_e(t) \\ 0 & \text{otherwise} \end{cases} \tag{2.55}$$

$$\dot{q}_a(t) = \frac{P_m(t) - P_v(t)}{R_a}. \tag{2.56}$$

By substituting Equations (2.52)-(2.54) for Equation (2.20) and Equations (2.55)-(2.56) for Equation (2.25)-(2.26), we have the complete set of state equations characterizing the entire heart and circulation which incorporates the model here. Since an inductor is equivalent to a short-circuit under static conditions, we may utilize Equations (2.30)-(2.37) to determine the initial set of pressure with $C_a = C_e + C_m$.

We particularly consider the following parameter values: C_e=1.45 ml/mmHg, C_m=0.15 ml/mmHg, L_e=0.025 mmHg/(ms $-$ s^2), $Q_e^0 = \frac{C_e}{C_e+C_m} Q_a^0$, and $Q_m^0 = Q_a^0 - Q_e^0$. These parameters are chosen to emulate the reflections in the diastolic portion of the Finapres ABP waveform (Figure 2-16). As can be seen from this figure, the transformation from central arterial pulse contour ($P_e(t)$) to peripheral arterial pulse contour ($P_m(t)$) resembles that seen in the actual distributed system. We finally note that the nonlinear arterial compliance model in Section 2.5.1 may be incorporated in the linear model here particularly in place of the large, central arterial compartment in order to model simultaneously the nonlinear arterial compliance and peripheral ABP waveform.

Figure 2-16 (a) Finger artery pressure obtained with the Finapres from a human subject. (b) Model-generated central arterial pressure $P_e(t)$ and peripheral arterial pressure $P_m(t)$. Note that the model heart rate was set to 50 bpm here in order to match the human data.

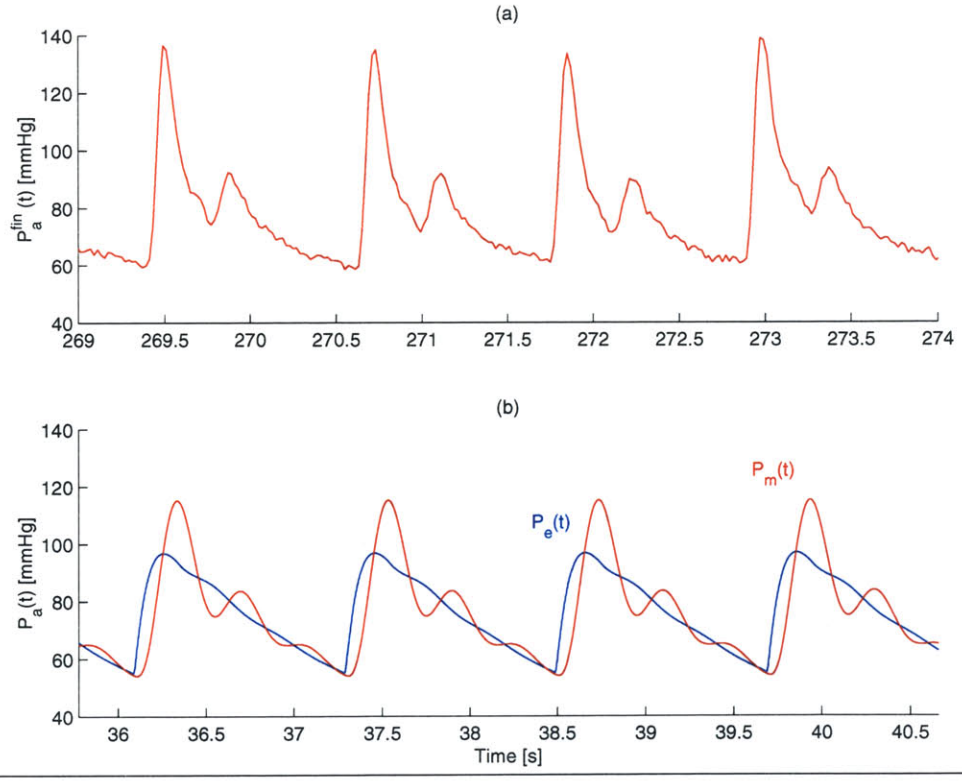

Chapter 3

Cardiovascular Regulatory System and Perturbations

The identification methods that we consider in Part II largely involve the analysis of resting hemodynamic fluctuations at frequencies below the mean heart rate using the techniques of linear least squares estimation. Since these techniques only consider the second-order statistics of the measured system input-output data [47,79] (see Section 4.2), we require a model that is capable of exhibiting reasonable low frequency hemodynamic variability in terms of power spectra, the frequency domain characterization of second-order statistics. However, by itself, the nominal model of the heart and circulation presented in Chapter 2 cannot at all account for hemodynamic fluctuations below the mean heart rate. These fluctuations are due to ongoing physiologic perturbations to the cardiovascular system disrupting homeostasis and the dynamic, compensatory response of the regulatory system. In this chapter, we consider modeling the cardiovascular regulatory system and resting physiologic perturbations such that the power spectra of the hemodynamic fluctuations at frequencies below the mean heart rate are reasonably represented. However, little is generally known about the precise nature of these power spectra with the exception being the spectra of

those few signals which are readily available from measurement (see Section 3.1.2). Hence, we must resort to constructing a model with the specific aim of reasonably representing the low frequency spectral content of readily available signals and with the assumption that the low frequency spectral content of the remaining model signals will also be reasonably accounted for as a consequence. The extent to which the assumption actually holds may not be so critical, since we are interested in practical identification methods in Part II which require only readily available signals. As discussed in Chapter 1, these signals include arterial blood pressure (ABP), heart rate, instantaneous lung volume (ILV), and left ventricular flow rate (cardiac output, CO).

We begin this chapter by providing relevant background material concerning cardiovascular regulation and low frequency hemodynamic variability (Section 3.1). We then present our model of the short-term cardiovascular regulatory system (Section 3.2) followed by our model of the ongoing physiologic perturbations that occur during resting conditions (Section 3.3). We next summarize the major properties of our complete, nominal model of the cardiovascular system which consists of these two models together with the nominal heart and circulatory model of Chapter 2 (Section 3.4). We conclude this chapter by demonstrating that the forward model generated power spectra indeed resembles experimental human data (Section 3.5).

3.1 Background

We present here background material concerning cardiovascular regulation and low frequency hemodynamic variability which essentially provide the rationale for the models of the short-term regulatory system and resting physiologic perturbations presented in Sections 3.2 and 3.3. In particular, we first provide a brief description of the relatively well understood cardiovascular regulatory system (Section 3.1.1). We then summarize some of the relevant findings in the literature related to less

understood low frequency hemodynamic variability which reveal some insight into the nature of resting physiologic perturbations as well as regulatory system dynamics (Section 3.1.2).

3.1.1 Cardiovascular Regulation

Cardiovascular regulation is a highly complex process aimed at maintaining homeostasis largely through multiple feedback and control systems. Regulation occurs at both local (intrinsic control) and global (extrinsic control) levels. Intrinsic control involves the regulation of local vascular resistance by each individual tissue bed in order to match local blood flow rate to metabolic demand. This autoregulatory scheme would not be realizable if ABP, which may be considered to be the pressure gradient across each tissue bed, were not held constant. Extrinsic control, in fact, involves the regulation of ABP as well right atrial pressure (and/or volume). The mechanisms responsible for extrinsic control depend on the specific time scales considered. In the short-term (seconds to minutes), negative feedback mechanisms mediated by the autonomic nervous system play the principal role[1]. These feedback systems include the arterial and cardiopulmonary baroreflex arcs which regulate ABP and right atrial pressure through the modulation of, for example, total peripheral resistance (TPR) and heart rate (see Section 3.2.1 and 3.2.2). Another of these feedback systems is the arterial chemoreflex arc which is also responsible for regulating ABP; however, it only plays a significant role during periods of hemodynamic stress (*e.g.*, ABP below 80 mmHg). The baroreflex systems contribute little to cardiovascular regulation in the long-term (hours to days), because they will eventually adapt to the pressure levels to which they are exposed. Rather, on these longer time scales, extrinsic control

[1]There are also negative feedback mechanisms mediated by fast acting hormonal systems; however, we assume their contribution to short-term regulation is small as compared to the autonomic nervous system.

is mediated by negative feedback hormonal systems which regulate pressures mainly through modulation of extracellular fluid volume. The renin-angiotensin-aldosterone system is the principal hormonal system involved over these longer time scales. As will be discussed in Section 3.1.2, this system seems to play some role in short-term regulation as well. For a complete treatment of cardiovascular regulation, see, for example, [10,32].

3.1.2 Low Frequency Hemodynamic Variability

Power spectral analysis of resting heart rate and ABP has been extensively investigated over the past 25 years (see, for example, [1,2,4,37,40,61,68]) and has provided much of the current knowledge on the dynamical nature of resting physiologic perturbations to the cardiovascular system as well as the regulatory system[2]. Three prominent peaks (centered at frequencies of ~0.02 Hz, ~0.1 Hz, and ~0.2 Hz) have been identified in the power spectrum of short-term, resting heart rate and ABP (below the mean heart rate frequency), but one or more of these peaks may not be present in a given spectrum [2,37]. As will be discussed below, the mechanisms responsible for eliciting these peaks, particularly the two lower frequency peaks, have not been fully elucidated. However, the dynamical roles of the parasympathetic and β-sympathetic

[2]By itself, power spectral analysis cannot distinguish between the physiologic perturbations and the regulatory system dynamics. Hence, it is rather limited in terms of providing an understanding of the mechanisms responsible for generating low frequency hemodynamic fluctuations. However, when utilized in conjunction with experimental interventions (*e.g.*, pharmacological autonomic blockade and pacing) as is the case in most of the investigations described in this section, power spectral analysis can provide such an understanding. As discussed in Section 1.1, system identification is the preferred approach for understanding the mechanisms responsible for eliciting low frequency hemodynamic variability, because it can distinguish regulatory system dynamics from physiologic perturbations during nearly normal physiologic conditions. In fact, system identification methods are now beginning to receive increased recognition in this regard [61].

nervous systems in eliciting the heart rate peaks have been explained to some extent through an experiment conducted in our laboratory which utilized pharmacologic autonomic blockade in conscious dogs [2]. In this experiment, administration of a parasympathetic blocker (glycopyrrolate) completely abolished the highest frequency peak and partially diminished the two lower frequency peaks. The additional administration of a β-sympathetic blocker (propranolol) completely abolished the two lower frequency peaks. The administration of propranolol alone partially diminished only the two lower frequency peaks. Hence, as mentioned in Section 1.2, the parasympathetic and β-sympathetic nervous systems are exclusively responsible for governing heart rate. These two systems may be thought of as lowpass filters with the sympathetic filter having a lower cutoff frequency ($<\sim$0.15 Hz versus $\sim$0.5 Hz). That is, the parasympathetic system is able to respond more quickly to its inputs than the relatively sluggish sympathetic system.

The highest frequency peak, which is relatively well understood, is elicited by respiratory activity whose rate is normally high enough such that only the parasympathetic nervous system is excited [2]. This peak is centered at the respiratory frequency and has been found to move with shifts in the respiratory rate [37]. Of course, during random interval breathing, respiratory activity excites both parasympathetic and β-sympathetic nervous systems eliciting fluctuations in heart rate and ABP over a significantly wider frequency range [8,59]. In a study conducted in our laboratory in atrially paced conscious dogs, it was found that ABP fluctuations at the respiratory frequency were substantially diminished suggesting that ABP fluctuations due only to respiratory induced intrathoracic pressure variations are relatively small [1]. Several distinct physiologic mechanisms are believed to be responsible for mediating the heart rate fluctuations at the respiratory frequency. These fluctuations are referred to as respiratory sinus arrhythmia, the phenomenon in which heart rate increases with inspiration and decreases with expiration. The mechanisms include the baroreflex

systems which are excited by the intrathoracic pressure changes and a direct neural coupling mechanism between respiration and heart rate. Our laboratory has found, through cardiovascular system identification, that this latter mechanism plays a significant role in short-term cardiovascular regulation in humans (see Section 3.2.3) [59].

The two lower frequency peaks are less understood but are generally considered to be due to vasomoter activity perturbing TPR and thus exciting the autonomically mediated baroreflex systems [1, 2, 43]. This belief is supported, but not proven by, numerous studies, some of which are described below.

Several studies have implicated these low frequency peaks to thermoregulatory mechanisms inducing fluctuations in vasomoter tone [43, 48]. For example, fluctuations in skin blood flow, heart rate, and ABP were found to be diminished in humans in a cool environment [48]. In the study described above in atrially paced conscious dogs, low frequency ABP fluctuations were not attenuated indicating that these fluctuations are not caused by heart rate fluctuations [1]. This study also demonstrated that, with pharmacologic blockade of the renin-angiotensin system in addition to the atrial pacing, low frequency fluctuations in ABP substantially increased. Although the dynamics of the renin-angiotensin system are relatively slow, it still appears to play a role in short-term regulation through possibly contributing to the establishment of the system operating point. Perhaps because it is quite conceivable that the relatively sluggish thermoregulatory system may play a similar role in short-term regulation, the investigators of this study hypothesized a different mechanism for the generation of low frequency fluctuations : "Local vascular beds regulate local resistance to match flow to demand. The renin-angiotensin system plays a role in controlling the resultant variability in peripheral resistance, whereas residual variability is compensated for by the heart rate variation through the baroreceptor reflex."

Studies in conscious dogs and cats under conditions of hemodynamic stress, such as hemorrhage, have revealed prominent 0.05 Hz oscillations in ABP and heart rate

which are referred to as Mayer waves [6, 50]. In a study conducted in our laboratory in conscious, hemorrhaged dogs, Mayer waves were concluded to be dependent on sympathetic activation, because these oscillations were not elicited during baseline conditions and were present during hemorrhage with and without pharmacologic parasympathetic blockade [50]. In this study, heart rate variations at 0.05 Hz were considered to be due to the arterial baroreflex system as heart rate was found to lag ABP, a result that is corroborated by a simple computer study [49]. This latter study also demonstrated that system resonance in the TPR baroreflex feedback loop could be responsible for these oscillations. However, it has been hypothesized that a central oscillator or rhythmic smooth muscle contraction in systemic arteries could be responsible as well [6]. In perhaps a similar vein, the mid-frequency peak in humans is usually only seen upon standing in which prominent $\sim$0.1 Hz oscillations in heart rate and ABP are elicited [68]. It has been demonstrated through computer simulation that this "posture" peak could also reflect the resonance in feedback loop between ABP and TPR [24]. A common mechanism responsible for both the 0.05 Hz fluctuations in hemorrhaged dogs and the $\sim$0.1 Hz oscillations in standing humans seems quite possible, but may not be probable [50], through increased sympathetic activity.

These studies demonstrate that low frequency ABP fluctuations are not due to heart rate; however, they do not necessarily imply that low frequency heart rate fluctuations are due exclusively to ABP. In fact, we have recently found, through cardiovascular system identification (see, for example, Figure 5-3), significant low frequency fluctuations in heart rate which are not attributable to (linearly independent of) ABP as well as random-interval respiratory activity [3, 59]. It is possible that these fluctuations may be due to the cardiopulmonary baroreflex system; however, since respiratory activity is strongly linearly correlated with right atrial pressure, this is probably not entirely the case. Hence, we hypothesized that these fluctuations

may also be due to other factors such as higher brain center activity. It should be noted that none of these studies preclude stroke volume variations as a potential mechanism for inducing low frequency ABP fluctuations. Such variations could, for example, occur through fluctuations in systemic venous dead volume.

Power spectral analysis of long-term fluctuations in heart rate and ABP have revealed fractal behavior ($1/f^{\alpha}$, α near 1) on a log-log scale [40,44,58,77]. For example, the power spectra of 24 hour heart rate recordings from healthy human subjects have demonstrated $1/f^{\alpha}$ ($\alpha \approx 1$) behavior over four decades of frequency ($\sim 10^{-5}$ to 10^{-1} Hz) [40,77]. It is quite possible that this behavior was not seen in higher frequency bands because of the frequency response of short-term cardiovascular regulatory mechanisms. Fractal behavior, in which small events occur more frequently than large events, implies scale invariance. That is, heart rate and ABP (at frequencies below the mean heart rate) signals appear the same regardless of the time scale considered. This type of behavior is exhibited by a wide variety of physical systems, ranging from electrical resistors to earthquakes [58]. The mechanisms responsible for the fractal behavior of most of these systems, including the long-term cardiovascular regulatory system, are unknown which may lead one to consider the possibility of a single unifying mechanism linking these seemingly different systems. In a recent study from our laboratory, potential mechanisms responsible for fractal behavior in long-term cardiovascular regulation were investigated [58]. In particular, linear regulatory mechanisms coupling ABP, heart rate, cardiac output, and ILV in conscious sheep were not found to be responsible for $1/f$ behavior. The investigators of this study hypothesized that diffusive mechanisms associated with neural or local hormonal regulatory processes may be responsible.

3.2 Short-Term Regulatory System

Since we are interested here in accurately accounting for low frequency hemodynamic fluctuations on the time scale of second to minutes, we need only to consider modeling the short-term regulatory system. Fortunately, modeling the short-term extrinsic control system has been extensively investigated as well (see, for example, [23,55,84]). We particularly choose the short-term extrinsic regulatory system of CVSIM as the basis for our model here [23]. The CVSIM regulatory model provides for negative feedback regulation of ABP via a simple dynamical arterial baroreflex system which behaves essentially linearly when excited by small perturbations. Although this model, which is based on experimental data from our laboratory [9], has been shown to generate reasonable hemodynamic behaviors in terms of steady-state closed-loop gain, dynamical response to step inputs, and stability, the simple model cannot possibly account for all the dynamical behaviors of the actual arterial baroreflex arc. This highly sophisticated system has been shown to exhibit complicated nonlinear behaviors including, for example, hysteresis [51]. However, such complex behaviors are usually elicited during extreme experimental conditions as opposed to the stable experimental conditions of cardiovascular system identification data collection. Furthermore, nonlinear models have been shown to only provide a modest improvement with respect to linear models in accounting for heart rate fluctuations observed from such stable conditions [17]. Hence, this largely linear dynamical model seems to be adequate for our purposes.

The CVSIM regulatory model also provides a convenient framework for the incorporation of models of the cardiopulmonary baroreflex arc and the direct neural coupling mechanism between respiration and heart rate. These three models together constitute our model of the short-term extrinsic regulatory system. In Sections 3.2.1-3.2.3, we present each of these models with the nominal values of the parameters that characterize them and describe their implementation. Although our heart and

circulatory model lumps each of the individual tissue beds of the systemic circulation into a single resistor (R_a), we also present a zeroth-order model of intrinsic control in Section 3.3.2.

3.2.1 CVSIM Arterial Baroreflex

The CVSIM regulatory model is based on the conceptualization of the arterial (Ar) baroreflex arc as the feedback system illustrated in the block diagram of Figure 3-1. The feedback system is aimed at tracking a setpoint ABP (P_a^{sp}) through the following sequence of events. The baroreceptors (pressure sensors located in the aortic arch and carotid arteries) sense ABP and then relay this information via autonomic afferent fibers to the autonomic centers in the brain. Here, the autonomic nervous system (ANS) compares the deviation between the sensed pressure and P_a^{sp} (error signal) with zero and then sends commands via autonomic efferent fibers to the heart and systemic circulation to adjust cardiac output (CO) and TPR such that the resulting ABP will keep the error signal near zero. CO and TPR are specifically adjusted through the control of the following four heart and circulatory parameters: heart rate ($F(t)$), ventricular contractility (in terms of $C_{l,r}^{es}(t)$)[3], $Q_v^0(t)$ (which alters ventricular preload), and $R_a(t)$ (TPR). These four model parameters are no longer considered to be constant, so we write them here and henceforth with the argument t.

We now describe the contents of each of the three blocks of the feedback system in Figure 3-1 and include a description of model implementation which involves filtering signals at higher sampling rates than that of the filter. It is important that no or little effective aliasing results from this filtering process, because the effective system dynamics responsible for data generation would be difficult to determine which would

[3] Although the maximum systolic pressure may increase with contractility, for simplicity, we only consider autonomic control of $C_{l,r}^{es}(t)$ which will vary the ventricular end-systolic pressure-volume relationships in terms of the slope of its linear portion as well as its shape (see Section 2.2.3).

Figure 3-1 Block diagram of the feedback system representing the CVSIM arterial baroreflex arc [23].

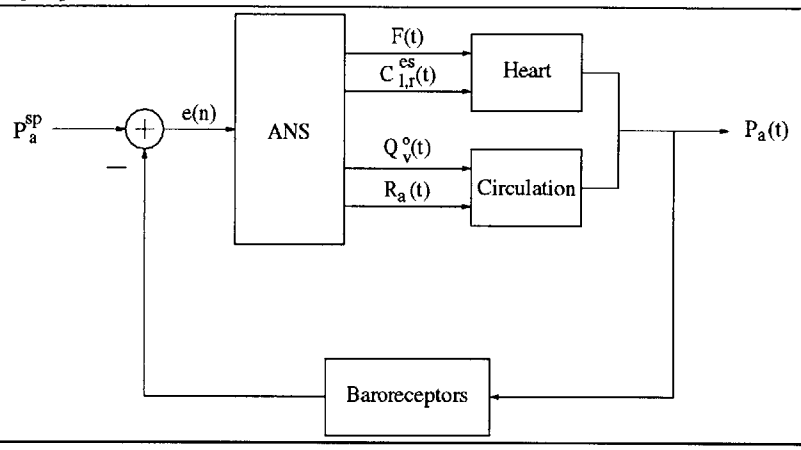

impede our identification analysis in Part II [62]. Although the CVSIM arterial baroreflex implementation performs reasonably in this regard, we describe a modified version of this implementation below which further reduces aliasing effects.

The frequency response of autonomically mediated cardiovascular regulatory mechanisms is bandlimited at frequencies less than the mean heart rate [23], while pulsatile ABP is bandlimited at frequencies about ten times the mean heart rate. This implies that it would be computationally inefficient for the model baroreceptors to sense ABP at each and every integration step (see Section 2.3.4). The model instead senses average $P_a(t)$ over the most recent 0.25 s interval every 0.0625 s ($P_a(n)$, where n here and henceforth denotes discrete-time at a sampling period of 0.0625 s). The anti-alias filtering here (averaging) is implemented via Backward Euler integration and delays the output by 0.125 s. It should be noted that the average integration step is $\sim$0.005 s which results in about a magnitude reduction in computation for the chosen sampling period here. We could have considered an even larger sampling period which could still satisfy our implementation goals here, but this would require a more sophisticated anti-aliasing filter which would be more difficult to implement. Hence, the baroreceptor block in Figure 3-1 may be viewed as a type of decimator.

The block representing the autonomic nervous system is a nonlinear, dynamical

mapping between the coarsely sampled error signal ($e(n) = P_a(n) - P_a^{sp}$) and the four more finely sampled controllable parameters of the heart and circulatory model. This block specifically consists of four analogous, parallel branches each of which are responsible for controlling one of these parameters. Each of these branches includes three sub-blocks arranged in series as in Figure 3-2.

Figure 3-2 Block diagram of one of the four parallel branches comprising the ANS block in Figure 3-1.

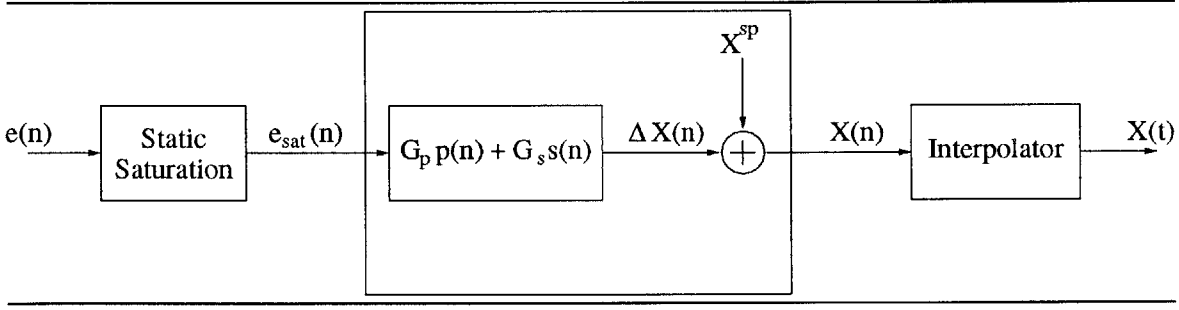

The first sub-block is a static, nonlinear mapping which represents the ubiquitously reported arterial baroreflex saturation characteristic [51]. The precise mapping employed is given as follows:

$$e_{sat}(n) = 18 \operatorname{atan}\left(\frac{e(n)}{18}\right). \tag{3.1}$$

This mapping indicates the limiting behavior of autonomic nervous control. That is, the controllable parameters cannot be adjusted to arbitrarily large or small values.

The middle sub-block consists of a dynamical, LTI filter followed by a summer. In particular, the filter represents an autonomically mediated effector mechanism which indicates how the model decides to adjust each of the controllable parameters based on the history of $e_{sat}(n)$. The filter is specifically defined by a linear combination of two unit area impulse responses, one ($p(n)$) of which characterizes the fast, parasympathetic limb of the autonomic nervous system and the other ($s(n)$), the slower, sympathetic limb (both α- and β-sympathetic sublimbs). Figure 3-3 illustrates $p(n)$ and $s(n)$ along with their magnitude squared Fourier transforms. The sum of the weighting constants (G_p, G_s) represents the static gain of the LTI filter. The output

of the filter, which is the mandated change in the controllable parameter ($\Delta X(n)$, where X denotes any of the four parameters and Δ henceforth denotes "change in"), is subsequently summed with a predefined, setpoint value (X^{sp}) in order to obtain the value of the controllable parameter ($X(n)$) at the ensuing coarse time step. The nominal static gain values of each of the filters as well as all the setpoint values are provided in Table 3.1. Although the $\alpha-$ and β-sympathetic sublimbs are both characterized by $s(n)$, we indicate in the table which particular sublimb is considered to be associated with each sympathetic effector mechanism. This allows us to model, for example, the effects of propranolol which selectively blocks the β-sympathetic sublimb by simply setting the appropriated gain values to zero.

It follows then that the last sub-block must be a type of interpolator. In particular, in this sub-block, the controllable parameter values at each integration step ($X(t)$) are determined from $X(n)$ through linear interpolation. However, linear interpolation is a noncausal filtering operation which requires the next sample, that is, $X(n+1)$. Hence, we may implement this filter by introducing a delay of 0.0625 s. In order for the effective filter delay to mimic that of the impulse responses in Figure 3-3, the 0.0625 s delay together with the delay of 0.125 s from the baroreceptor block must be nullified. This may be taken care of by implementing these impulse responses advanced in time by 0.1875 s.

Of course, the heart and circulation block in Figure 3-1 may consist of any of the set of models presented in Chapter 2. However, since these models are only capable of handling a fixed heart rate, the block also includes an integral pulse frequency modulation (IPFM) model of the sinoatrial node [7]. This intuitive model provides a simple, nonlinear mapping from heart rate to the times of onset of ventricular contraction. In particular, the IPFM model here uses the Backward Euler method to integrate $F(t)$ (in units of bps) over time until the integral is equal to one. At this point, the ventricle initiates contraction through Equations (2.17)-(2.18) (in which

Figure 3-3 (a) Parasympathetic effector mechanism impulse response $p(n)$. (b) Parasympathetic effector mechanism magnitude squared Fourier transform $|P(f)|^2$. (c) Sympathetic effector mechanism impulse response $s(n)$. (d) Sympathetic effector mechanism magnitude squared Fourier transform $|S(f)|^2$. These impulse responses are derived from experimental dog data obtained from a study conducted in our laboratory [9]. The estimated impulse responses from the experimental data actually characterized the influence of autonomic input (both vagal and β-sympathetic) to the sinoatrial node on heart rate. The investigators of this study argued that the α-sympathetic effector mechanism probably has similar system dynamics to $s(n)$.

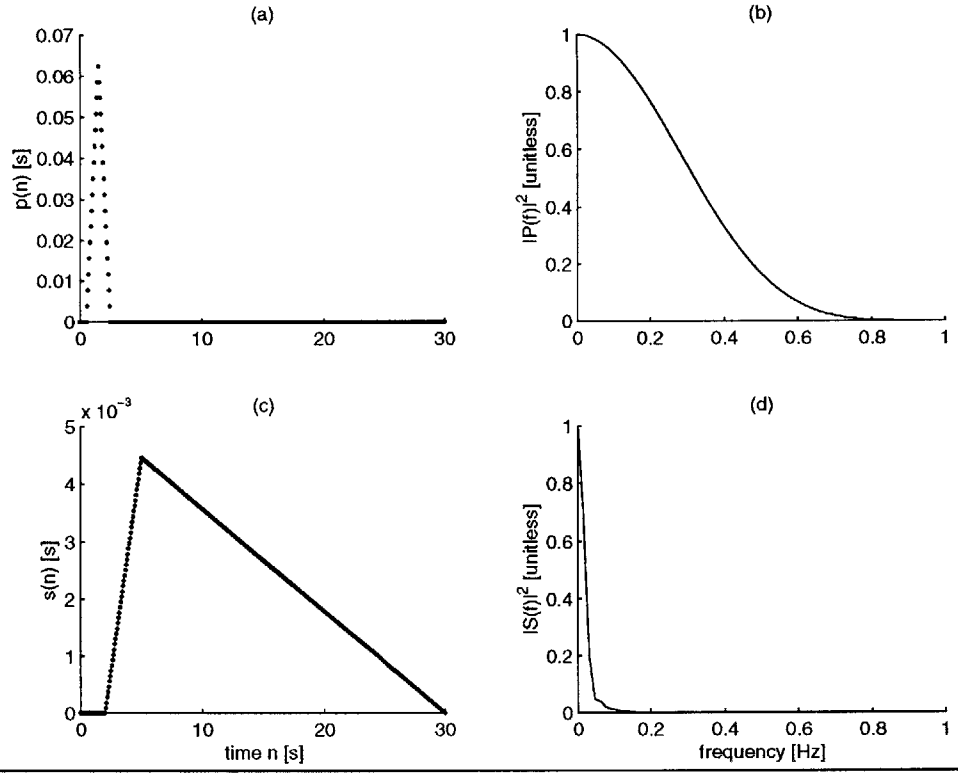

$T_{s,i} = 0.3\sqrt{T_{i-1}}$, where the subscript i denotes the i^{th} beat), the integral is set to zero, and the integration is repeated.

In order to demonstrate that the effective system dynamics resulting from the above implementation are largely known (aliasing is negligible), we performed the following simple test. We first generated $P_a(t)$ and $F(t)$ from our nominal heart and circulatory model in conjunction with a perfectly linear version of the arterial baroreflex model in which the static saturation mapping (first sub-block in Fig-

$X(t)$	X^{sp}	G_s^{Ar}	G_p^{Ar}	G_s^{CP}	G_p^{CP}
$F(t)$, bps	1.2	-0.017	-0.017 (β)	0 (β)	0
$C_{l,r}^{es}(t)$, $\frac{\text{ml}}{\text{mmHg}}$	0.4,1.2	0.009,0.028 (β)	0	0 (β)	0
$R_a(t)$, $\frac{\text{mmHg-s}}{\text{ml}}$	1.0	-0.011 (α)	0	-0.065 (α)	0
$Q_v^0(t)$, ml	2600	26.5 (α)	0	90.0 (α)	0
Pressure setpoints: $P_a^{sp} = 94$ mmHg $P_{\text{“}ra\text{”}}^{tr,sp} = 7.8$ mmHg					

Table 3.1: Summary of the nominal parameters values characterizing the arterial (Ar) and cardiopulmonary (CP) baroreflex models. For a given row, the units of the gain values are the ratio of the units of the corresponding $X(t)$ to mmHg. The specific sympathetic sublimb (α or β) corresponding to each weighting value of $s(n)$ is provided in parentheses. These values are taken from CVSIM [23] with the following exceptions. The setpoint pressures are determined from the average pressures in the uncontrolled model (see Figure 2-5), while the gain values of $F(t)$ and $C_{l,r}^{es}(t)$ are increased by 33% as explained in Section 3.3.3.

ure 3-2) was removed[4]. We then estimated the nonuniformly sampled $F(t)$ through the continuous-time convolution of linearly interpolated $P_a(t) - P_a^{sp}$ with $h(t) = -0.017s(t) - 0.017p(t)$, where $s(t)$ and $p(t)$ are linearly interpolated, scaled versions of the impulse responses in Figure 3-3 with the scale factor being 16 (uniform sampling frequency) and their weightings are from Table 3.1. Since the resulting predicted heart rate ($F_{pre}(t)$) and the actual heart rate ($F_{act}(t)$) are nearly identical (see Figure 3-4), the effective system dynamics from model implementation are characterized by the impulse response defined above.

[4] $F(t)$ varies here due to the transient set up by the initial conditions.

Figure 3-4 The blue trace, $F_{act}(t)$, is generated by the model, while the red trace, $F_{pre}(t)$, is predicted as described in the text. The fact that these two signals are nearly identical suggests that the baroreflex implementation results in minimal aliasing and the effective system dynamics are essentially known.

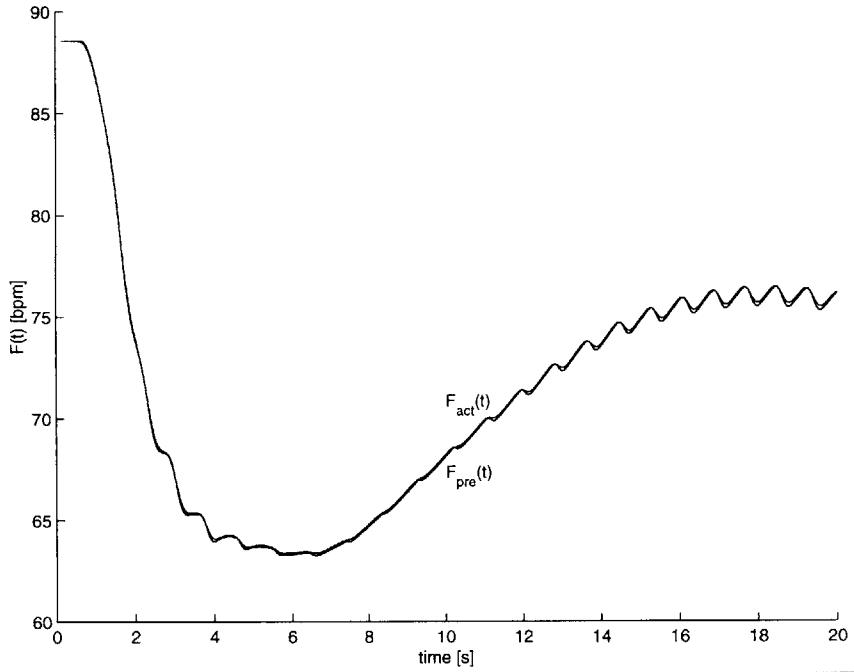

3.2.2 Cardiopulmonary Baroreflex

The less understood cardiopulmonary (CP) baroreflex arc can also be conceptualized with a feedback diagram similar to that in Figure 3-1 except the sensed pressure here is generally considered to be the transmural pressure in the right atrium. Hence, our model implementation of this baroreflex system is essentially the same as that of the arterial baroreflex system presented in the previous section. The major difference in implementation is that the model pressure that is sensed is specifically $P_{\text{“}ra\text{”}}(t) - P_{th}(t)$, which we henceforth refer to as "right atrial" transmural pressure ($P^{tr}_{\text{“}ra\text{”}}(t)$, RATP). We also implement the following static saturation mapping for this baroreflex system:

$$e_{sat}(n) = 5 \operatorname{atan}\left(\frac{e(n)}{5}\right). \tag{3.2}$$

This mapping as well as the nominal static gain values, which are also provided in Table 3.1, are from [35].

The table indicates that the cardiopulmonary baroreflex control of contractility and heart rate are both omitted in the nominal model. Contractility control is neglected simply due to a lack of available data. On the other hand, data addressing the issue of heart rate control in humans do exist but are controversial [52]. In dogs, the nature of the cardiopulmonary baroreflex control of heart rate is generally agreed upon. That is, heart rate increases with right atrial pressure (positive static gain), the so called Bainbridge reflex [10, 52]. For example, in one study in which the relative roles of the cardiopulmonary and arterial heart rate baroreflex systems in dogs were examined, the static gain of the former reflex system was found to be about -3 times that of the latter reflex system with no nonlinear interaction reported between the two systems [72]. However, the Bainbridge reflex has yet to be found in humans. Consequently, some investigators believe it to be absent in humans [52], while others think that confounding influences on heart rate due to other reflex systems render it difficult to measure. In contrast to the Bainbridge reflex, in a recent study in humans, investigators reported heart rate to decrease with increasing right atrial pressure (negative static gain) as well as increasing ABP [25]. These investigators specifically found the static gain of the cardiopulmonary heart rate baroreflex to be approximately +2 times that of the arterial heart rate baroreflex with no nonlinear interaction between the two systems. However, the investigators of another study in humans interpreted similar data through a nonlinear coupling argument. In particular, these investigators reported that reductions in right atrial pressure and/or volume augment the arterial heart rate baroreflex [64]. Given that it is not even clear whether the static gain of cardiopulmonary baroreflex control of heart rate is positive or negative, we choose to set it to zero in our nominal model[5]. From Table 3.1, we finally note that if $P^{tr}_{\text{“}ra\text{”}}(t)$

[5]It should be noted that presence or absence of cardiopulmonary baroreflex control of heart rate may play a critical role in the performance of the cardiovascular identification method. In Section 5.4.1, we analyze the robustness of this method over a range of static gain values of the cardiopulmonary heart rate baroreflex..

increases, the reflex model will cause $R_a(t)$ to decrease (negative gain value) which will in turn result in a further increase in $P^{tr}_{\text{“}ra\text{”}}(t)$. Hence, unlike the arterial baroreflex model, the model here is not solely geared to track $P^{tr}_{\text{“}ra\text{”}}(t)$. Rather, since an increase in $P^{tr}_{\text{“}ra\text{”}}(t)$ will increase $P_a(t)$ within a few beats through CO, the cardiopulmonary baroreflex model here is also aimed at contributing to $P_a(t)$ regulation.

In addition to the conclusions in [64] described above, other experimental studies (*e.g.*, [51]) have found the arterial and cardiopulmonary baroreflex systems to be nonlinearly coupled. These studies have particularly demonstrated that a substantial drop in right atrial pressure leads to an increase in the static gain of the arterial baroreflex system (see Section 6.1). Since this pressure does not vary over such wide ranges during the relatively stable experimental conditions of cardiovascular system identification data collection, we neglect modeling nonlinear interactions here. Furthermore, other studies, as described above, have not reported any nonlinear interactions between the two reflex systems.

3.2.3 Neural Coupling Between Respiration and Heart Rate

Our laboratory has been interested in the quantitative characterization of the direct neural coupling mechanism between respiration and heart rate [59, 76, 83]. As discussed in Section 1.1, our approach has been based on a system identification analysis of fluctuations in physiologic signals which include instantaneous lung volume (ILV) and heart rate. Our characterization of this mechanism is in terms of an LTI impulse response relating ILV fluctuations (independent of ABP fluctuations) to heart rate fluctuations. There are two important features of the estimated dynamics of this impulse response. The first feature is that the impulse response is noncausal [59, 83] indicating that heart rate changes actually anticipate changes in ILV. The second feature is that the impulse response may be well represented by a linear combination of two other estimated impulse responses, one of which represents the effects of

parasympathetic activity on heart rate and the other, sympathetic activity on heart rate [83].

Our model of the direct neural coupling mechanism, which contributes to the respiratory sinus arrhythmia phenomenon, is now readily apparent. In particular, we define an impulse response relating ILV fluctuations to heart rate fluctuations as a linear combination of $s(n)$ and $p(n)$ in Figure 3-3, each of which are advanced in time by 1.5 s to account for the noncausality. The weighting values are taken from [59] and are -0.0002 bps/ml for $s(n)$ and 0.00012 bps/ml for $p(n)$. These values indicate that upon inspiration there is a withdrawal of parasympathetic activity followed by a withdrawal of β-sympathetic activity. In order to implement this model, we must develop a model of an ILV signal ($Q_{lu}(t)$). In Section 3.3.1, we describe such a model in terms of continuous-time functions. Thus, for the purposes of implementation, which may be achieved prior to the determination of the pressures, volumes, and flow rates of the cardiovascular model, we first generate $Q_{lu}(t)$ and sample it analogously to the baroreceptor block in Figure 3-1 ($Q_{lu}(n)$), and then after filtering[6], we interpolate the output $\Delta F(n)$ analogously to the last sub-block in Figure 3-2 in order to obtain $\Delta F(t)$ due to the direct neural coupling mechanism.

3.3 Resting Physiologic Perturbations

In contrast to the heart and circulation and the short-term regulatory system, a relatively small number of models of resting cardiovascular perturbations have been developed for the purposes of eliciting and analyzing low frequency hemodynamic variability (see [24, 49]). This is perhaps due to the limited understanding of these perturbations. In this section, we present models of three exogenous physiologic perturbations which are motivated by published experimental findings summarized in

[6]The filtering may be achieved by convolving $Q_{lu}(n)$ with $-0.0002s(n) + 0.00012p(n)$ and then shifting the output back in time by 1.5 s.

Section 3.1.2 and describe their implementation. In particular, in Section 3.3.1, we describe the incorporation of a model of random-interval (and fixed-rate) breathing into the forward model. Then, in Section 3.3.2, we present a simple model of TPR fluctuations reflecting the autoregulation of local vascular beds. Finally, in Section 3.3.3, we describe the inclusion of $1/f$ heart rate fluctuations into our model.

3.3.1 Respiratory Activity

In this section, we present models of $Q_{lu}(t)$ during both fixed-rate and random-interval breathing so that the direct neural coupling mechanism between respiration and heart rate in Section 3.2.3 may be implemented. However, as mentioned in Section 3.1.2, respiratory activity also perturbs the cardiovascular system through mechanically induced changes in intrathoracic pressure (see voltage sources in Figure 2-1). We thus conclude this section with a simple model of human ventilatory mechanics which maps $Q_{lu}(t)$ to $P_{th}(t)$.

During fixed-rate or metronome breathing, $Q_{lu}(t)$ strongly resembles a sinusoid. Hence, a simple, yet accurate, model for such a signal is given as follows:

$$Q_{lu}(t) = Q_{fr} + \frac{Q_t}{2}\left(1 - \cos\left(\frac{2\pi t}{T_r}\right)\right), \tag{3.3}$$

where Q_{fr}, the functional residual volume of the lungs, is set to 2200 ml, Q_t, the tidal volume, is set to 500 ml, and T_r, the respiratory period is set to 5 s [45, 85]. The model here may also be considered to represent normal, spontaneous breathing which, at least to first approximation, appears to be sinusoidal as well. The purpose of this simple model is made evident in Sections 3.3.3 and 3.5. It should be noted that sinusoidal models of respiratory activity have been previously considered [24, 49].

In our random-interval breathing protocol, the period of each respiratory cycle is determined from the outcome of an independent probability experiment governed by a modified exponential probability density function which allows the respiratory

period to range from one to 15 seconds with a mean of five seconds [8]. The subjects are allowed to control their tidal volume so that normal ventilation is not disrupted. Equation 3.3 also serves as the basis for a model of $Q_{lu}(t)$ resulting from this protocol. In particular, each respiratory cycle is defined to be one period of the sinusoid in this equation with the period determined from an experimental outcome of the probability experiment. The tidal volume of each respiratory cycle is chosen such that the alveolar ventilation rate from random breathing is identical to that from metronome (*met*) breathing. Alveolar ventilation rate, which is the flow rate of air from the atmosphere to the alveoli, may be defined as a continuous function of time as follows:

$$\dot{q}_{alv}(t) = \frac{Q_t(j) - Q_{ds}}{T_r(j)}, \quad t_j \leq t < t_j + T_r(j), \tag{3.4}$$

where Q_{ds}, the dead space (no alveoli) in the airways (*air*), is set to 150 ml [85] and the argument j denotes the j^{th} respiratory cycle while the subscript j denotes the commencement of the j^{th} respiratory cycle. That is, $\dot{q}_{alv}(t)$ is a stepwise, continuous process in which the duration of each step is given by the respiratory period. Since the tidal volume and respiratory rate are constant during fixed-rate breathing (Equation (3.3)), the alveolar ventilation rate is constant overall time ($\dot{q}_{alv}^{met} = 70$ml/s). The following model of $Q_{lu}(t)$ generated by our random-interval breathing protocol with $\dot{q}_{alv}(t) = \dot{q}_{alv}^{met}$ results:

$$Q_{lu}(t) = Q_{fr} + \frac{\dot{q}_{alv}^{met} T_r(j) + Q_{ds}}{2} \left(1 - \cos\left(\frac{2\pi(t - t_j)}{T_r(j)}\right)\right), \quad t_j \leq t < t_j + T_r(j), \tag{3.5}$$

where

$$T_r(j) = 1 - \frac{1}{0.2083} \ln(1 - x(j)(1 - \mathrm{e}^{-2.92})) \tag{3.6}$$

with $x(j)$ being the outcome of the j^{th} independent probability experiment defined by a uniform distribution ranging between zero and one [8].

The mapping from $Q_{lu}(t)$ to $P_{th}(t)$ is based on the simple model of ventilation illustrated in Figure 3-5 in terms of its electrical circuit analog. The electrical components may be interpreted similarly to those in Figure 2-1 by considering air here rather than blood (see Section 2.1). Hence, the resistor may be thought of as a conduit for airflow from the atmosphere to the lungs and vice versa, while the capacitor may be interpreted as an air volume container representing the lung compartment. This compartment is parametrized by a dead volume as well as a compliance similar to Equation (2.1). Given this constitutive relationship along with the governing differential equation characterizing the model, $P_{th}(t)$ may be determined from $Q_{lu}(t)$ through the following equation:

$$P_{th}(t) = P_{alv}(t) - \frac{1}{C_{lu}}(Q_{lu}(t) - Q_{lu}^{0}), \tag{3.7}$$

where

$$P_{alv}(t) = -R_{air}\frac{d}{dt}Q_{lu}(t) \tag{3.8}$$

with $R_{air} = 0.0026$ (mmHg-s)/ml, $C_{lu} = 252.5$ ml/mmHg, and $Q_{lu}^{0} = 1190$ ml [45]. Note, from Equations (2.7)-(2.9) and Equations (2.19)-(2.24), that $P_{alve}(t)$ and the derivative of Equation (3.7) is necessary for model implementation. The derivative of this equation is given as follows:

$$\frac{dP_{th}(t)}{dt} = -R_{air}\frac{d^2}{dt^2}Q_{lu}(t) - \frac{1}{C_{lu}}\frac{d}{dt}Q_{lu}(t). \tag{3.9}$$

3.3.2 Autoregulation of Local Vascular Beds

Autoregulatory processes controlling local vascular resistance not only influence central hemodynamic variables, such as ABP and CO, through TPR but are influenced by these hemodynamic variables as well. However, our systemic microcirculatory model is lumped into a single parameter $R_a(t)$ and little is known about the system

Figure 3-5 Model of ventilatory mechanics in terms of its electrical circuit analog. As mentioned in Section 2.2.1, $P_{atm}(t) = 0$ mmHg.

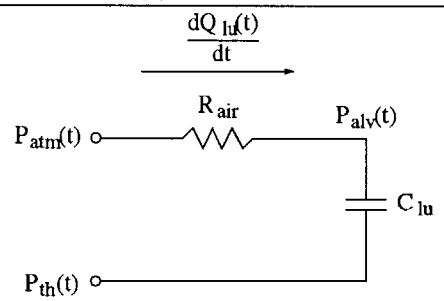

dynamics characterizing autoregulatory processes. Hence, we resort to developing a simple model representing the fluctuations in $R_a(t)$ due to the cumulative effects of the autoregulation of local vascular beds which is based on a stochastic framework and neglects input influences from all hemodynamic variables. To this end, consider all the tissue beds of the systemic microcirculation as a set of N parallel, variable resistors with N large. In terms of our heart and circulatory model, this may be thought of as decomposing or unlumping $R_a(t)$ into such a set of resistors. Let the i^{th} variable resistor in the set have conductance $G_i(t)$, which may be modeled probabilistically in terms of a density function. The mean of the probability density function for a fixed time is equal to $\frac{1}{N}$ ml/(mmHg-s) so that the mean lumped conductance is 1 ml/(mmHg-s), while the variance is set to the arbitrary value of $\frac{\sigma^2}{N}$ (ml/(mmHg-s))^2, where σ^2 is any nonzero, finite value. We assume that each variable resistor in the set may be characterized by this probability density function and that the conductance value of each resistor is independent of the conductance values of the other variable resistors. Then, by the Central Limit Theorem, $R_a(t)$, for a given time, may be essentially characterized by a Gaussian cumulative distribution function with a mean of 1 (mmHg-s)/ml and variance σ^2 ((mmHg-s)/ml)^2 [28].

Although the assumption of independence of each of the conductance values seems somewhat reasonable, the time evolution of $R_a(t)$ due to autoregulatory processes cannot be independent over time. That is, $R_a(t)$ here is not a white noise process,

but rather a highly colored process. Unfortunately, the precise frequency response characteristics of autoregulatory processes is largely unknown; however, experimental data from isolated dog skeletal muscle suggest that these processes are relatively slow with a half-power bandwidth $<\sim$0.05 Hz [10]. Furthermore, provided that the hypothesis that autoregulatory processes are responsible for the $\sim$0.1 Hz posture peak in humans (see Section 3.1) is indeed correct, then these processes must be somewhat significant near this frequency. Hence, a zeroth-order model of the fluctuations in $R_a(t)$ about its mean value due specifically to autoregulatory processes, which we henceforth refer to as $n_{R_a}(t)$, may be considered to be a Gaussian white noise process with zero mean and variance σ^2 that is bandlimited to 0.1 Hz.

We implement this simple model as follows. A vector of independent Gaussian random variables with zero mean and variance σ^2 is generated. This vector, which is considered to be a discrete-time process at a sampling period of 0.0625 s, is filtered with the following finite impulse response function:

$$h(n) = \begin{cases} 0.2\text{sinc}(0.2\pi n) & -960 \leq n \leq 960 \\ 0 & \text{otherwise} \end{cases}, \tag{3.10}$$

whose frequency response is bandlimited to 0.1 Hz. Then, the filtered signal $(n_{R_a}(n))$ is interpolated as described in the last sub-block in Figure 3-2 arriving at $n_{R_a}(t)$ which is considered to be an additive, exogenous disturbance to $R_a(t)$. Finally, we note that σ^2 is considered to be a free parameter whose value is chosen based on a set of experimental data as described in Section 3.3.3.

3.3.3 $1/f$ Heart Rate Fluctuations

As discussed in Section 3.1.2, ABP and respiratory activity (which is strongly correlated with RATP) are not the only factors responsible for perturbing heart rate. Other factors, which may include higher brain center activity impinging on the autonomic nervous system, most likely play a significant role in the generation of heart

rate fluctuations as well. Certainly, the development of a physical model of these largely unknown factors is not feasible. However, it is well known that heart rate fluctuations demonstrate fractal behavior over at least four decades of frequency in which the highest frequency decade is within the frequency band considered by the identification methods in Part II. For these reasons, we consider here the introduction of $1/f$ heart rate fluctuations as an additive, exogenous perturbation to our nominal model. Since heart rate fluctuations have been found to be almost exclusively governed by the autonomic nervous system [2], we particularly consider a $1/f$ exogenous disturbance as an input to a filter characterized by the parasympathetic and sympathetic (β-sympathetic sublimb) impulse responses in Figure 3-3.

Model implementation here is similar to that described in Section 3.3.2. A discrete-time, $1/f$ process is generated at a sampling period of 0.0625 s ($w_F(n)$). Instead of filtering $w_F(n)$ with the impulse response in Equation (3.10), it is convolved with $h(n) = 12s(n) + 12p(n)$. (The two weighting values here are arbitrarily chosen, and as will be made evident below, are not important as long as they are the same.) The filtered process ($n_F(n)$) is interpolated as described by the last sub-block in Figure 3-2 arriving at $n_F(t)$ which is considered to be the additive, exogenous disturbance to $F(t)$. All that is left is to describe the simulation of the $1/f$ process.

Several methodologies for the generation of $1/f$ processes have been developed [42,58,74]. We consider here the conceptually simple method in which a $1/f$ process is simulated by passing a white noise process through an ARMA filter whose bode plot is nearly $1/f$ over the frequency range of interest [42,74]. The filter design strategy is actually quite simple. Real-valued poles and zeros are chosen in an alternating fashion such that a $1/f$ process may be approximated as illustrated in Figure 3-6. Note that the filter design method here can achieve a $1/f$ bode plot with arbitrary accuracy simply through the inclusion of additional pole-zero pairs. We are interested here in designing a filter whose bode plot is $1/f$ over four frequency decades ranging from

10^{-4} Hz to 1 Hz. We consider the placement of one pole-zero pair per a decade (four pole-zeros pairs overall) as described in [42,74]. This pole-zero placement scheme has been demonstrated to deviate from true $1/f$ behavior by at most ~5% [42,74]. The resulting frequency location of the poles (F_p) and zeros (F_z) are given as follows:

$$F_p^i = 10^{-3.75+i} \quad 0 \leq i \leq 3 \tag{3.11}$$

$$F_z^i = 10^{-3.25+i} \quad 0 \leq i \leq 3. \tag{3.12}$$

Figure 3-6 Pole-zero placement strategy for the design of an ARMA filter with nearly $1/f$ bode plot. The blue line indicates the desired $1/f$ bode plot, while the red line indicates the approximation given one pole-zero pair per decade. Adapted from [74].

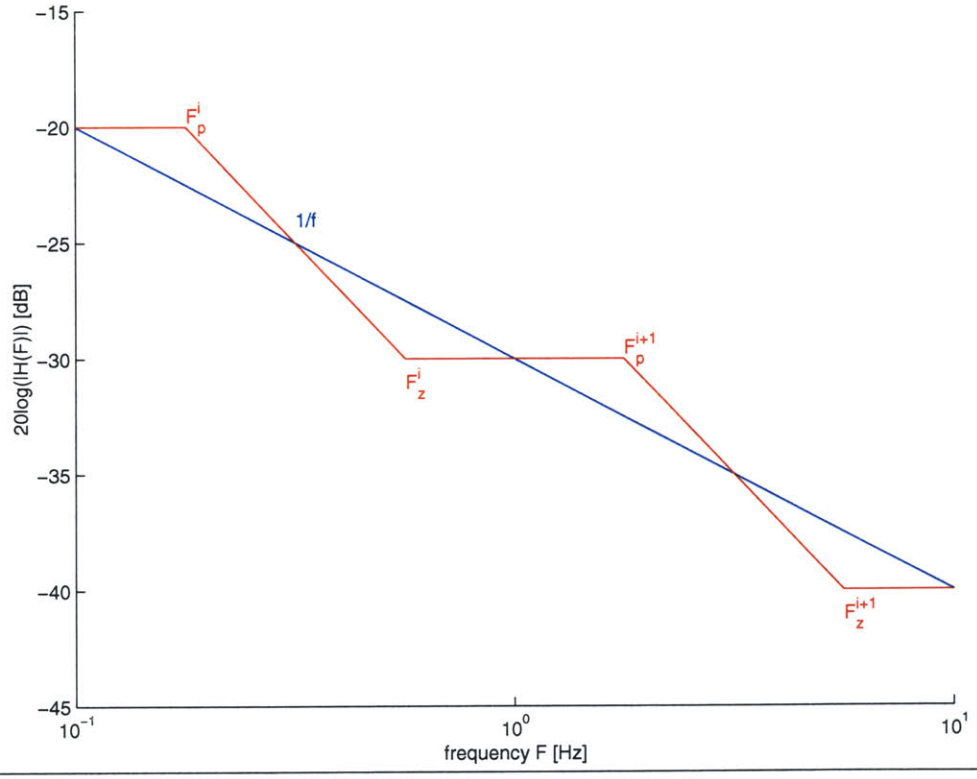

Since the amplitude of the $1/f$ process may be set to any value through the adjustment of the variance of the white noise process, we simply assign a scale factor of unity to the continuous-time filter here. In order to implement this filter, we must first discretize it as described in [21]. We particularly utilize the bilinear transformation which maps stable, continuous-time poles and zeros to stable, discrete-time poles and

zeros [62]. The bilinear transformation, which is equivalent to trapezoidal integration in the time domain, is given as follows:

$$f = \frac{1}{2\pi}\frac{1-\pi F T_s}{1+\pi F T_s}, \tag{3.13}$$

where f is the discrete-time pole or zero and T_s is the sampling period. It can be shown that the bilinear transformation warps the high frequencies [62]. That is, the high frequency content of the filter is not preserved after transformation. However, if the bandwidth of the continuous-time system is small with respect to the sampling frequency (oversampling), then the entire frequency response will be preserved. This is the case here in which the bandwidth of the frequency response is <1 Hz, while, from above, the sampling frequency is 16 Hz (T_s=0.0625 s). The discrete-time filter defined here may now be convolved with a vector of independent Gaussian random variables of zero mean and variance λ^2 in order to arrive at $w_F(n)$.

Like σ^2, λ^2 is considered to be a free parameter. The values of these two parameters are chosen such that the model power spectra match experimental power spectra determined from a set of data previously obtained from 12 NASA astronauts breathing at a fixed-rate of 0.25 Hz in the standing posture. The data set consists of continuous, noninvasive measurements of heart rate and finger ABP (Finapres) as well as ECG-derived ILV (which is uncalibrated) for each subject. The properties of this particular data set suit our purposes here quite well. The fixed-rate breathing protocol ensures that the two lower frequency peaks are not corrupted by respiratory activity. The standing posture is in accord with our model of the pulmonary arterial resistance described in Section 2.2.2. Additionally, this posture allows us to demonstrate that the model exhibits a system resonance that resembles the "posture" peak (see Section 3.5). Finally, given the tremendous inter-subject variability in spectra [2, 61], it seems more reasonable to consider a number of subjects rather than a single subject. For example, we could choose a subject who may have spectra that are unlike any other subject. This may render our identification analysis in Part II

less meaningful.

The specific procedure for choosing the parameter values based on this data set is as follows. We compute the mean of the power in three nonoverlapping frequency bands of heart rate and ABP over the group of 12 subjects (see Table 3.2). (The method for computing the spectra is described in Section 4.4.) The free parameters, σ^2 and λ^2, are then tuned such that the power in these frequency bands for $F(t)$ and $P_a(t)$ are near their respective human mean values. It should be noted that we also increased the static gain values of the arterial baroreflex impulse responses which manipulate $F(t)$ and $C_{l,r}^{es}(t)$ by 33% from their original CVSIM values in order to satisfy reasonably this matching procedure (see Table 3.2). Based on this procedure, we set $\sigma = 0.035$ (mmHg-s)/ml and $\lambda = 0.00008$ bps. It is important to realize that the values of these parameters significantly influence the results of the identification analysis in Part II. Hence, in Part II, we actually consider a range of values for these parameters which includes the nominal values determined here.

	$F(t)$ Power, bpm^2		$P_a(t)$ Power, mmHg^2	
Frequency Bands, Hz	Model	Humans	Model	Humans
0.00-0.04	7.2 ± 2.0	5.8 ± 3.5	3.9 ± 0.6	4.2 ± 3.0
0.04-0.15	4.1 ± 0.8	5.7 ± 3.3	8.4 ± 2.0	8.0 ± 4.1
0.15-0.40	1.9 ± 0.1	0.9 ± 0.5	2.9 ± 0.2	1.4 ± 0.5

Table 3.2: The mean and standard deviation of the power in three low frequency bands of heart rate and ABP as determined from experimental human data and the nominal model. The experimental values are determined from a set of 12 subjects as described in the text, while the model values are computed from 10 different model realizations with $\dot{q}_{alv}(t) = 70$ ml/s.

3.4 Nominal Model Summary

In Section 3.5, we demonstrate the validity of the nominal model of the cardiovascular system presented in Chapter 2 and Sections 3.2 and 3.3 in terms of the power spectra of the signals analyzed in Part II. But first, in this section, we summarize the major components of the nominal model as follows:

1. The heart and circulation is a lumped system consisting of six compartments representing the left and right ventricles, the systemic arteries and veins, and the pulmonary arteries and veins.

2. The short-term regulatory system includes arterial and cardiopulmonary baroreflex systems as well as a direct neural coupling between respiration and heart rate.

   (a) The arterial baroreflex system senses ABP and adjusts the following parameters: heart rate, left and right ventricular contractility, systemic arterial resistance (TPR), and systemic venous dead volume.

   (b) The cardiopulmonary baroreflex system senses the effective RATP and adjusts the following parameters: TPR and systemic venous dead volume.

   (c) The controllable heart and circulatory parameters are specifically manipulated through fast (parasympathetic) and/or slow (sympathetic) effector mechanisms as follows:

      i. Heart rate: both β-sympathetic and parasympathetic

      ii. Left and right ventricular contractility: β-sympathetic

      iii. TPR: α-sympathetic

      iv. Systemic venous dead volume: α-sympathetic

3. The resting physiologic perturbations include respiratory activity, autoregulation of local vascular beds, and a $1/f$ process.

(a) Respiratory activity impinges on the heart and circulation through intrathoracic pressure (reference pressure of the ventricle and pulmonary compartments) via a simple ventilatory system as well as the direct neural coupling mechanism.

(b) The autoregulation of local vascular beds is represented by an exogenous bandlimited white disturbance added to TPR.

(c) The $1/f$ process is introduced as an exogenous input to both β-sympathetic and parasympathetic effector mechanisms which outputs a disturbance to heart rate.

The block diagram in Figure 3-7 illustrates how these major components specifically fit together to form our nominal model of the cardiovascular system. The data generated from this model (and variants of it) are the test bed against which the identification methods in Part II are assessed.

3.5 Nominal Model Validation

We now demonstrate that the low frequency power spectral content of the signals considered in Part II indeed resemble experimental data obtained from standing humans breathing according to a fixed-rate protocol. Although we are most interested in emulating cardiovascular system identification data, we again consider a fixed-rate breathing protocol, because random-interval breathing obscures the fluctuations due to other resting physiologic perturbations. That is, we could probably account for, to a large extent, the spectra with only a respiratory perturbation; however, we know that other physiologic perturbations are also present [59]. Since there is tremendous inter-subject variability in hemodynamic spectra, we first considered demonstrating that the model spectra resembles the mean spectra of the 12 NASA astronauts (see Section 3.3.3). However, averaging may smear out the spectral peaks, as they are not

Figure 3-7 The block diagram illustrates how the three models described in Chapter 2 and Sections 3.2 and 3.3 fit together to form our nominal model of the cardiovascular system. p, α, and β, which are respectively abbreviations for parasympathetic, α-sympathetic, and β sympathetic, indicate which effector mechanisms are involved (if any) in each of the blocks.

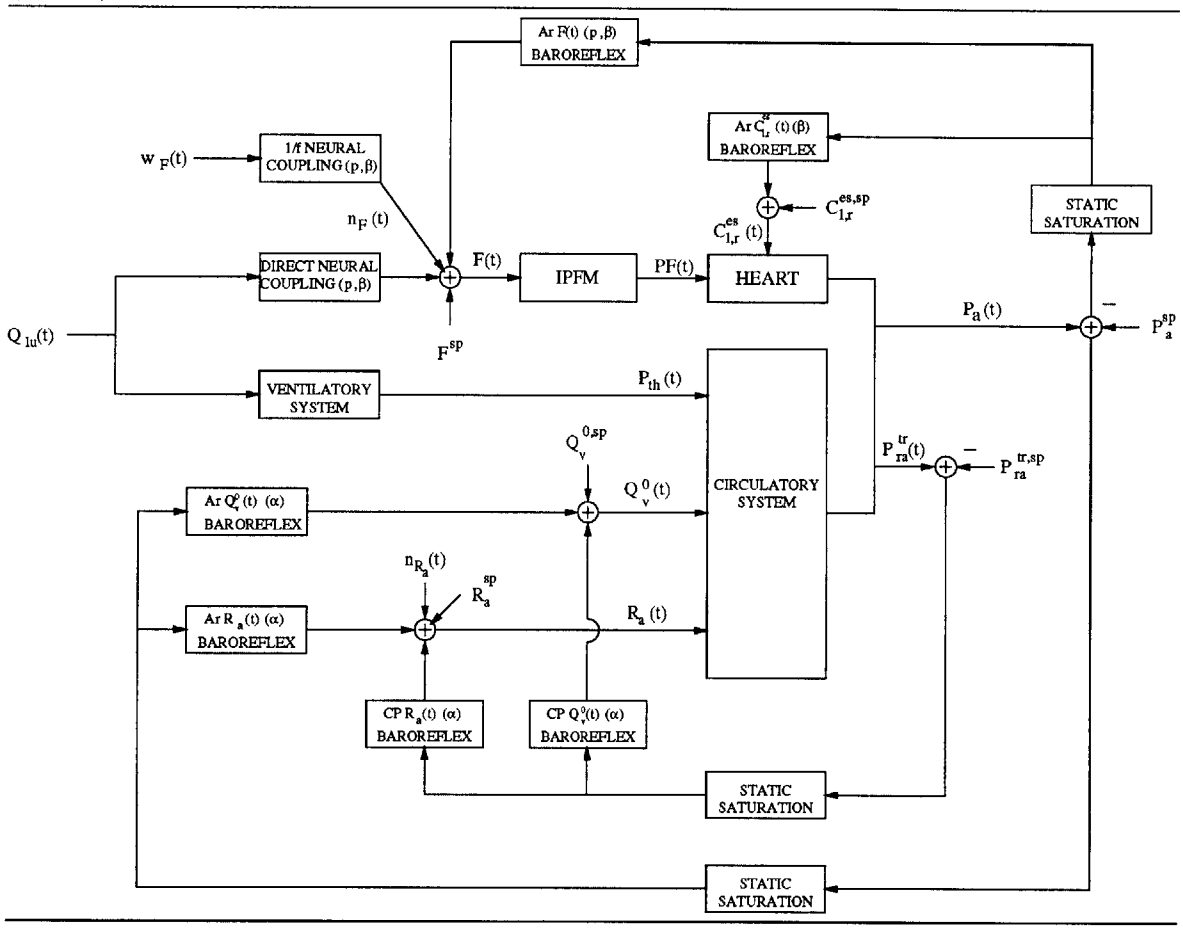

necessarily centered at the same frequencies for each subject. We instead resort to demonstrating that the model spectra resemble spectra from an individual astronaut. This does not seem so unreasonable if we keep in mind that the power in the three spectral bands reflects the average over the group of astronauts (see Section 3.3.3).

Figure 3-8 illustrates that the model power spectra of $Q_{lu}(t)$, $F(t)$, and $P_a(t)$ at frequencies below the mean heart rate indeed resemble spectra obtained from an astronaut. (As pointed out in Section 3.3.3, the methods for computing these spectra is described in Section 4.4.) Differences at the respiratory frequency in the figure and in Table 3.2 may be attributed to the fact that the astronaut(s) here did not precisely

follow the fixed-rate breathing protocol as well as discrepancies in tidal volume which was unknown in the astronauts (see Section 3.3.3). Figure 3-8 also demonstrates that the model spectra exhibits a spectral peak at $\sim$0.07 Hz which is near the center frequency of the "posture" peak in humans. Since the exogenous perturbations at this frequency were broadband, this peak indicates a system resonance in the model. This result supports the simple computer simulation of Deboer [24] which demonstrated that the "posture" peak could be due to a system resonance. Deboer specifically implicated the system resonance to the arterial baroreflex system controlling TPR. In order to elucidate fully the mechanisms responsible for the mid-frequency peak of the significantly more complicated model here, a complete analysis of the closed-loop system dynamics is necessary. This analysis is beyond the scope of the thesis. However, based on a few simple simulation experiments in which the gain values of open-loop effector mechanism were varied, we have found that the mid-frequency peak is substantially diminished in the absence of the arterial baroreflex systems controlling systemic venous dead volume as well as TPR. That is, both these mechanisms are involved in eliciting the mid-frequency peak.

Unfortunately, due to technical difficulties, the standing posture makes it very difficult to obtain the reasonably accurate Doppler ultrasound CO measurement. We instead resort to the Doppler measurement obtained while a subject is tilted upright (30^o with respect to the supine posture) for our comparison. Figure 3-9 illustrates that the model spectrum of $\dot{q}_l(t)$ (at frequencies below the mean heart rate) reasonably resembles spectra obtained from an individual subject. It is important to realize that we did not build our model or choose its parameters such that this particular spectra would match experimental data. This gives some credence to our assumption that the low frequency spectral content of the remaining model signals have been somewhat accounted for as a consequence of reasonably representing the spectra of the aforementioned signals.

Figure 3-8 Power spectra of respiratory activity (normalized to unity power), heart rate, and ABP (at frequencies below the mean heart rate) as generated from the nominal model and a single standing human breathing at a fixed rate of 0.25 Hz. The model spectra are determined from the average of 10 different model realizations with $\dot{q}_{alv}(t) = 70$ ml/s.

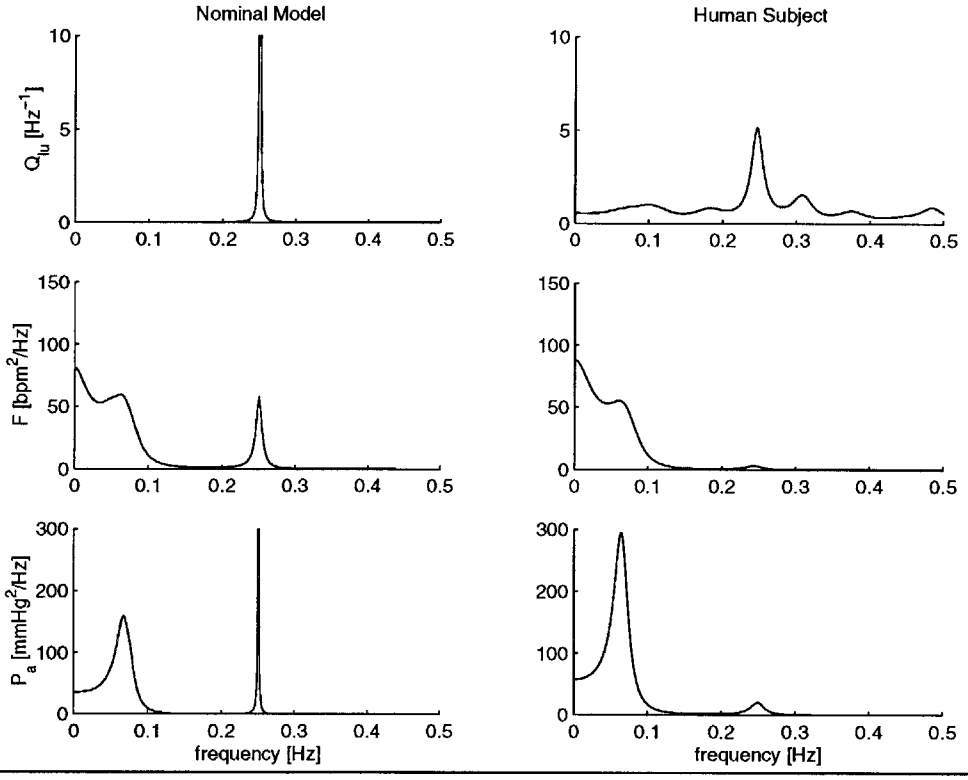

It should be noted that it is also necessary to demonstrate the validity of the cross-spectra between each of these signals. This essentially amounts to demonstrating that the transfer functions which characterize the couplings between the signals are consistent with those determined from experimental data. However, this has been virtually taken care of by the very construction of the model which was based largely on physiologic findings published in the literature.

Figure 3-9 Power spectra of CO (at frequencies below the mean heart rate) as generated from the nominal model and a single human breathing normally and tilted upright 30^o with respect to the supine posture. The model spectrum is determined from the average of 10 different model realizations with $\dot{q}_{alv}(t) = 70$ ml/.

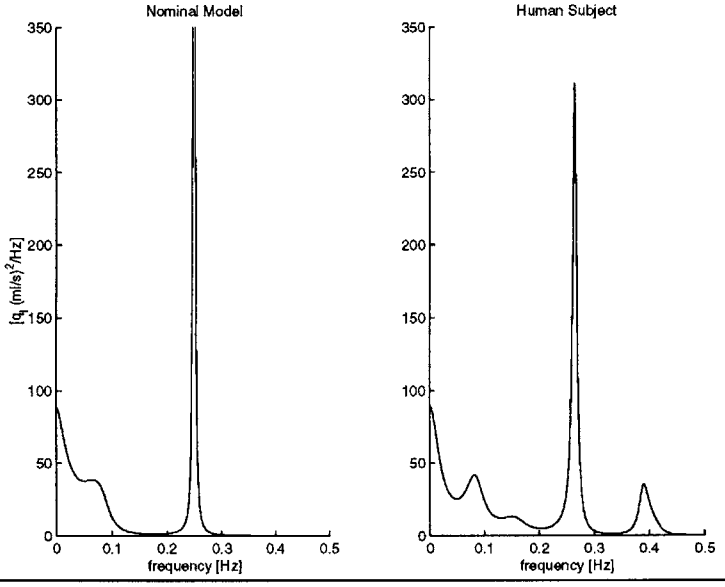

Part II

System Identification

Chapter 4

Data Analysis

In this part, we consider data generated from the forward model of Part I as a test bed for the evaluation of the cardiovascular system identification method introduced in Section 1.1 (Chapter 5) and the development and analysis of novel, practical identification methods for quantifying the total peripheral resistance (TPR) baroreflex (Chapter 6) and monitoring steady-state changes in TPR (Chapter 7). But first, in this chapter, we describe the data analysis techniques that are employed by these identification methods. We begin, in Section 4.1, by introducing the AutoRegressive Moving Average (ARMA) model which is a specific class of linear, time-invariant (LTI) input-output models that is completely characterized by a finite set of adjustable parameters. The ARMA model structure is sufficiently complex to account for the dynamics of many LTI systems yet simple enough to permit relatively straightforward parameter estimation from measured system input-output data. In Section 4.2, we describe ARMA parameter estimation based on the analytic methods of linear least squares assuming that the model order, the number of parameters necessary to characterize the system, is known. Then, in Section 4.3, we discuss model order selection and present the specific algorithm that we implement. We conclude, in Section 4.4, with a description of a method for estimating power spectra based on the

data analysis techniques described in the previous three sections.

4.1 ARMA Models

Since we consider the identification of systems with up to two inputs in Chapters 5-7, in this section, we introduce the dual-input ARMA difference equation model with output $y(t)$ and inputs $u_1(t)$ and $u_2(t)$ as follows:

$$y(t) = \sum_{i=1}^{l} a_i y(t-i) + \sum_{i=s_1}^{f_1} b_{1,i} u_1(t-i) + \sum_{i=s_2}^{f_2} b_{2,i} u_2(t-i) + e(t), \tag{4.1}$$

where $e(t)$ is an unobserved disturbance (residual error) that is assumed to be a white noise process (see Section 4.2.2) which may represent measurement noise and/or unmeasured system inputs. The a and b coefficients are respectively referred to as the autoregressive (AR) and moving average (MA) parameters, while the summation limits l, s_j, f_j $(j = 1, 2)$ encompass the model order. We point out two important features of the ARMA difference equation here. The first feature is that the difference equation is linear in its coefficients which implies that parameter estimation may be achieved analytically through linear least squares (see Section 4.2.1). The second feature is that strict causality between the system inputs and output may be imposed by virtue of setting $s_j = 1$ $(j = 1, 2)$ which is necessary for the reliable identification of open-loop systems operating in closed-loop (see Section 4.2.4).

The transfer functions characterizing the input-output relationships of Equation (4.1) may be made evident by applying the delay operator notation ($q^{-i}x(t) = x(t-i)$, where $x(t)$ is an arbitrary discrete-time signal) to this equation and rearranging terms as follows:

$$y(t) = \frac{B_1(q^{-1})}{A(q^{-1})} u_1(t) + \frac{B_2(q^{-1})}{A(q^{-1})} u_2(t) + \frac{1}{A(q^{-1})} e(t), \tag{4.2}$$

where

$$A(q^{-1}) = 1 - \sum_{i=1}^{l} a_i q^{-i} \tag{4.3}$$

$$B_j(q^{-1}) = \sum_{i=s_j}^{f_j} b_{j,i} q^{-i} \quad j = 1, 2. \tag{4.4}$$

The delay operator form here may be interpreted similarly to the z-transform and hence, the fractional quantities relating the two input signals to the output signal are referred to as transfer function operators. Equation (4.2) suggests that the AR parameters are solely responsible for representing the influence of the unobserved disturbance on the output (actual error), while both the MA and AR parameters are responsible for characterizing the transfer functions relating the system inputs to output. The fact that the actual error and the transfer functions are not represented independently is not too much of a restriction, because the MA model order may always be increased to compensate for the AR parameters. Since the transfer functions relating the system inputs to output include poles as well as zeros, ARMA models are capable of representing infinite-order impulse responses. Finally, we note that, under certain circumstances, the ARMA model is capable of approximating systems even when $e(t)$ is a colored process. In particular, let $e(t) = \frac{C(q^{-1})}{D(q^{-1})} w(t)$, where $w(t)$ is a white noise process. Then, by substituting this relationship into Equation (4.2) and rearranging terms, the following system results:

$$A'(q^{-1})y(t) = B'_1(q^{-1})u_1(t) + B'_2(q^{-1})u_2(t) + w(t), \tag{4.5}$$

where

$$A'(q^{-1}) = \frac{D(q^{-1})}{C(q^{-1})} A(q^{-1}) \tag{4.6}$$

$$B'_j(q^{-1}) = \frac{D(q^{-1})}{C(q^{-1})} B_j(q^{-1}) \quad j = 1, 2. \tag{4.7}$$

Hence, this system may be represented by an ARMA model provided that $A'(q^{-1})$ and $B'_j(q^{-1})$ $(j = 1, 2)$ may be approximated by finite polynomials in z which is possible if $\frac{1}{C(q^{-1})}$ is strictly stable. We, in fact, consider such an approximation in Section 6.2.4.

4.2 Parameter Estimation

From Equation (4.1), we see that the identification of ARMA models from measured system input-output data requires both the selection of the model order as reflected by the summation limits as well as the estimation of the parameter values once the model order has been selected. In this section, we describe parameter estimation assuming that the model order is known based on the well established methods of linear least squares. We first present, in Section 4.2.1, the analytic linear least squares solution corresponding to the ARMA model structure. Then, in Section 4.2.2, we analyze the performance of the linear least squares solution as the measured data samples tend to infinity $(N \to \infty)$. The purpose of this asymptotic analysis, which is largely from [47], is to provide the necessary conditions for reliable estimation and a means for estimating the uncertainty in the least squares solution. Next, in Section 4.2.3, we present a frequency domain interpretation of least squares estimation that is useful for understanding the performance of the cardiovascular system identification method (see Section 5.5). The material of this section is also largely from [47]. Finally, in Section 4.2.4, we present the requirements for reliable parameter estimation when the measured system input-output data are obtained from closed-loop operation which is the case for most of the identification methods considered in the following chapters.

4.2.1 Linear Least Squares Solution

In order to present the analytic, linear least squares solution corresponding to the ARMA model of Equation (4.1), we rewrite this equation in vector-product notation as follows:

$$y(t) = \phi^T(t)\theta + e(t), \tag{4.8}$$

where

$$\phi^T(t) = [y(t-1)\cdots y(t-l)\, u_1(t-s_1)\cdots u_1(t-f_1)\, u_2(t-s_2)\cdots u_2(t-f_2)] \tag{4.9}$$

$$\theta^T = [a_1 \cdots a_l\, b_{1,s_1} \cdots b_{1,f_1}\, b_{2,s_2} \cdots b_{2,f_2}]. \tag{4.10}$$

Now, let $y(t)\,, \phi(t)$ pairs over the interval $1 \leq t \leq N$ be available from measurement. Then, the solution to the least squares problem is given by the vector θ that minimizes the mean-squared residual error $e(t)$ over this interval. This may be mathematically stated as follows:

$$\hat{\theta} = \arg\min_{\theta} \frac{1}{N} \sum_{t=1}^{N} \varepsilon^2(t,\theta), \tag{4.11}$$

where

$$\varepsilon(t,\theta) = y(t) - \phi^T(t)\,\theta \tag{4.12}$$

and is the residual error corresponding to a particular choice of θ. Note that $\phi(t)$ here may be thought of as a vector of measured input data from which the present value of the output $y(t)$ is predicted.

An analytic solution for $\hat{\theta}$ may be derived from the orthogonality principle which states that the residual error corresponding to the least squares solution is orthogonal to the input prediction data [79]. That is, there is no more information in the prediction data that can be squeezed out to reduce further the mean-squared residual

error. The theorem may be mathematically stated as follows:

$$\frac{1}{N}\sum_{t=1}^{N}\phi(t)\varepsilon(t,\hat{\theta}) = 0. \tag{4.13}$$

For the ARMA model structure, this equation specifically implies that $\varepsilon(t,\hat{\theta})$ is a white noise process that is uncorrelated to the system inputs. By substituting Equation (4.12) into Equation (4.13) and solving for $\hat{\theta}$, the linear least squares solution results as follows:

$$\hat{\theta} = \left\{\frac{1}{N}\sum_{t=1}^{N}\phi(t)\,\phi^T(t)\right\}^{-1}\frac{1}{N}\sum_{t=1}^{N}\phi(t)\,y(t), \tag{4.14}$$

that is, provided that the indicated inverse exists.

4.2.2 Asymptotic Analysis

In order to analyze the performance of the linear least squares solution of Equation (4.14), we assume that the measured $y(t)$, $\phi(t)$ pairs are actually related according to the following linear system:

$$y(t) = \phi^T(t)\theta_0 + e_0(t), \tag{4.15}$$

where θ_0 may be thought of as the actual solution which is sought by linear least squares estimation and $e_0(t) = \varepsilon(t,\theta_0)$. Then, we may substitute Equation (4.15) into Equation (4.14) and rearrange terms arriving at the following equation:

$$\hat{\theta} - \theta_0 = \left\{\frac{1}{N}\sum_{t=1}^{N}\phi(t)\,\phi^T(t)\right\}^{-1}\frac{1}{N}\sum_{t=1}^{N}\phi(t)\,e_0(t). \tag{4.16}$$

If $\hat{\theta} - \theta_0$ is regarded as a random vector, then the performance of $\hat{\theta}$ with respect to θ_0 may be characterized statistically through, for example, the mean vector and covariance matrix of $\hat{\theta} - \theta_0$. It is difficult to compute such statistics for arbitrary values of N; however, when $N \to \infty$, the computation becomes tractable. To this

end, we assume that $y(t)$ and $\phi(t)$ are jointly wide-sense stationary and ergodic with respect to second-order moments such that, as $N \to \infty$,

$$\hat{\theta} - \theta_0 \to \left\{ E\,\phi(t)\,\phi^T(t) \right\}^{-1} E\,\phi(t)\,e_0(t) \quad \text{with probability one,} \tag{4.17}$$

where $E(\cdot)$ denotes the expectation operator. If $\hat{\theta} - \theta_0 \to 0$ as $N \to \infty$, then $\hat{\theta}$ is an asymptotically unbiased estimate of θ_0. This is possible provided that the following two conditions hold:

1. $\left\{ E\,\phi(t)\,\phi^T(t) \right\}^{-1}$ exists

2. $E\,\phi(t)\,e_0(t) = 0.$

The first condition will hold if $u_1(t)$ and $u_2(t)$ are sufficiently uncorrelated and contain as many frequency components as the dimension of θ. In this case, the measured input data are said to be persistently exciting of order equal to the dimension of θ. Thus, it is ideal for $u_1(t)$ and $u_2(t)$ to be independent, white processes. The second condition will hold if the prediction data is uncorrelated with the actual residual error. This is not a surprising condition when one considers the orthogonality principle.

We may quantify how fast $\hat{\theta}$ converges to θ_0 through the covariance matrix of the random vector in Equation (4.16). Assuming that the two conditions hold, then, as $N \to \infty$,

$$E(\hat{\theta} - \theta_0)(\hat{\theta} - \theta_0)^T \to \frac{\gamma^2}{N} \left\{ E\phi(t)\phi^T(t) \right\}^{-1} \quad \text{with probability one,} \tag{4.18}$$

where γ^2 is the variance of $e_0(t)$. If the residual error is Gaussian distributed (which seems quite possible here due to Central Limit Theorem arguments), then the covariance matrix here achieves the Cramer-Rao bound which is defined to be the minimum possible error covariance for all unbiased estimators. That is, $\hat{\theta}$ converges to θ_0 as fast as is possible for unbiased estimators. We note that regardless of the distribution of the residual error, $\hat{\theta} - \theta_0$ may be shown, through Central Limit Theorem arguments,

to be asymptotically Gaussian distributed with a mean vector of zeros and covariance matrix as given above. Hence, the statistics here provide a complete characterization of the performance of $\hat{\theta}$ provided that N is sufficiently large and the two conditions above are valid.

Finally, we note that an estimate of the covariance matrix of $\hat{\theta} - \theta_0$ may be derived based on Equation (4.18) as follows:

$$E(\hat{\theta} - \theta_0)(\hat{\theta} - \theta_0)^T \approx \frac{\frac{1}{N}\sum_{t=1}^{N} \varepsilon^2(t, \hat{\theta})}{N} \left\{ \frac{1}{N} \sum_{t=1}^{N} \phi(t)\phi^T(t) \right\}^{-1}. \tag{4.19}$$

This estimate provides a measure of uncertainty in the linear least squares solution. It is also useful to have a measure of the uncertainty in the transfer functions which are completely determined from this solution. Our laboratory has developed an approximate, linear mapping between the uncertainty in $\hat{\theta}$ and the uncertainty in the resulting transfer functions in the form of impulse responses from which a covariance matrix for the impulse response estimates may be simply derived [67]. Note that, since the mapping is linear and the parameter estimates are approximately Gaussian distributed, it is possible to compute confidence intervals associated with the estimated impulse responses.

4.2.3 Frequency Domain Interpretation

We may obtain useful insight into the performance of the transfer function estimates determined from $\hat{\theta}$ by considering the least squares problem of Equation (4.11) in the frequency domain. To this end, we again assume that $N \to \infty$ such that the least squares problem may be stated as follows:

$$\hat{\theta} = \arg\min_{\theta} E\varepsilon^2(t, \theta) = \frac{1}{2\pi} \int_{-\pi}^{\pi} \Phi_\varepsilon(\omega, \theta) d\omega, \tag{4.20}$$

where $\Phi_x(\omega)$ heretofore represents the power spectrum of a discrete-time signal $x(t)$, and the second equality is from the definition of the power spectrum. We rewrite

the sequence $\varepsilon(t,\theta)$ given in vector-product form in Equation (4.12) here in delay operator notation as follows:

$$\varepsilon(t,\theta) = A(q^{-1},\theta)y(t) - B_1(q^{-1},\theta)u_1(t) - B_2(q^{-1},\theta)u_2(t). \tag{4.21}$$

In order to evaluate the performance of the transfer function estimates, we assume that the measured input-output signals are actually related according to the following system:

$$y(t) = G_{1,0}(q^{-1})u_1(t) + G_{2,0}(q^{-1})u_2(t) + v_0(t), \tag{4.22}$$

where $G_{1,0}(q^{-1})$ and $G_{2,0}(q^{-1})$ may be thought of as the actual transfer function operators and $v_0(t)$ represents the actual disturbance to $y(t)$. Note that the system here depicts a general dual-input, LTI system which may be approximated with an ARMA model. By substituting Equation (4.22) into Equation (4.21) and analytically computing $\Phi_\varepsilon(\omega,\theta)$ assuming that $u_1(t)$, $u_2(t)$, and $v_0(t)$ are orthogonal, we arrive at the following frequency domain interpretation of the least squares problem:

$$\begin{aligned}\hat{\theta} = \arg\min_{\theta} \frac{1}{2\pi}\int_{-\pi}^{\pi} |A(e^{j\omega},\theta)|^2 \Bigg[\left| G_{1,0}(e^{j\omega}) - \frac{B_1(e^{j\omega},\theta)}{A(e^{j\omega},\theta)} \right|^2 \Phi_{u_1}(\omega) \\ + \left| G_{2,0}(e^{j\omega}) - \frac{B_2(e^{j\omega},\theta)}{A(e^{j\omega},\theta)} \right|^2 \Phi_{u_2}(\omega) + \Phi_{v_0}(\omega) \Bigg] d\omega.\end{aligned} \tag{4.23}$$

This equation suggests that, in the frequency domain, the least squares problem is weighted such that the fit between the actual and estimated transfer functions is favored at the frequencies in which the quantity $|A(e^{j\omega},\theta)|^2\Phi_{u_j}(\omega)$ $(j = 1, 2)$ is large. Since $|A(e^{j\omega},\theta)|^2$ is an estimate of the inverse power spectrum of $v_0(t)$, this quantity may be thought of as the model signal-to-noise ratio (SNR) and is useful for predicting the reliability of the transfer function estimates at a given frequency.

4.2.4 Closed-Loop Systems

We now present the requirements under which the two conditions of Section 4.2.2 will be valid when the measured system input-output data are obtained from closed-

loop operation which is the case for most of the identification methods considered in the following chapters. To this end, let us assume that the measured data are actually generated according to the following coupled, single-input ARMA difference equations:

$$y(t) = \sum_{i=1}^{l_y} a_i y(t-i) + \sum_{i=s_y}^{f_y} b_i u(t-i) + e_y(t) \tag{4.24}$$

$$u(t) = \sum_{i=1}^{l_u} c_i u(t-i) + \sum_{i=s_u}^{f_u} d_i y(t-i) + e_u(t). \tag{4.25}$$

For this data generation scheme, the second condition will hold provided that two requirements are satisfied [87]. The first requirement is that $e_y(t)$ and $e_u(t)$ are white, uncorrelated processes. The second requirement is that there is at least one delay term in the closed-loop system, that is, $s_y > 0$ and/or $s_u > 0$. Fortunately, most physical systems meet this latter requirement. It has also been demonstrated in [87] that satisfying the first requirement is sufficient for the first condition to hold as well.

We note that the frequency domain interpretation of the least squares problem in Equation (4.23) is not valid for input-output data obtained from closed-loop operation, because the inputs are no longer orthogonal to the disturbance. However, the model SNR is still useful for predicting the reliability of the transfer function estimates at a given frequency.

4.3 Model Order Selection

Although ARMA parameter estimation based on linear least squares is straightforward, model order selection is more complicated. If the model order is chosen to be too high (overparametrization), then the particular noise realization along with the system dynamics characterizing the measured input-output data will have been modeled. On the other hand, if the model order is chosen to be too low (underparametrization), then there will not be enough degrees of freedom to account for

the system dynamics coupling the measured input-output data. Model order selection involves finding an appropriate balance between overparametrization and underparametrization usually by choosing a set of candidate model orders and comparing each candidate in the set based on some criterion so as to select the best model order. In Section 4.3.1, we briefly review the popular approaches for comparing models. Then, in Section 4.3.2, we present a specific model order selection algorithm, which utilizes one of these approaches to compare an intelligently chosen set of candidate models, that is implemented by the identification methods of following chapters.

4.3.1 Approaches for Comparing Models

Model comparison may be facilitated by defining a criterion which quantifies model performance. The mean-squared residual error is a popular example of such a criterion. Ideally, models may then be compared in terms of this criterion on a fresh set of data (testing set) that is exclusive of the data considered for identification (training set). That is, the mean-squared residual error may be computed from the actual output data of the testing set and that predicted from the application of the model estimated from the training set to the input data of the testing set. This approach is referred to as cross-validation [47]. However, based on the asymptotic analysis in Section 4.2.2, it is often desirable to utilize all the available input-output data for the training set. In this case, it is not valid to compare models simply in terms of the estimated mean-squared residual error, because this criterion would favor overparametrization as the fit between the input-output data is always improved by increasing the model order. However, it is reasonable to assume that the improvement in fit is insignificant when an increase in model order results in overparametrization. Based on this assumption, two general methods have been developed for the case in which a training set of data is only available [47]. The first general method is based on statistical hypothesis testing which provides a framework for determining if

the estimated mean-squared residual error is significantly reduced by increasing the model order. The second general method is based on the establishment of information criteria (*e.g.*, Aikaike's Information Criterion and Final Prediction Error; see [47,79]) which provide a measure of model performance by combining, in some functional form, the estimated mean-squared residual error with a penalty factor for the number of parameters. An example of an information criterion, known as Rissanen's Minimum Description Length (MDL), is given as follows:

$$MDL(k) = \left\{1 + k\frac{\log(N)}{N}\right\}\frac{1}{N}\sum_{t=1}^{N}\varepsilon(t,\hat{\theta})^2, \tag{4.26}$$

where k is the number of model parameters (dimension of the vector $\hat{\theta}$). The MDL criterion may be implemented for model comparison by calculating the MDL value (which requires $\hat{\theta}$) for a set of candidate models and choosing the model in the set with the smallest MDL value. That is, the MDL criterion favors the model that best fits the data with the fewest model parameters possible. We, in fact, implement the MDL criterion in this manner as described in the next section.

4.3.2 ARMA Parameter Reduction Algorithm

In considering a set of candidate ARMA models to compare, one often defines a maximal model which is overparametrized to the extent that it is believed to contain the actual parametrization of the system in question. One may then compare all the reduced models within this initial maximal model in order to find the best model. However, if gaps are permitted between the parameters (*e.g.*, $b_{1,1} \neq 0$, $b_{2,1} = 0$, $b_{3,1} \neq 0$), then the number of comparisons that must be made becomes intractable even for modest maximal models. Such gaps have been found to be present in biological systems particularly in regards to the MA parameters. Hence, we utilize an ARMA parameter reduction algorithm which chooses, in an intelligent manner, a small set of candidate models from an initially chosen maximal model [67].

The basic idea behind the algorithm is that the relative likelihood of each parameter of the maximal model in being a member of the actual parametrization is reflected by it associated SNR value – defined here to be the ratio of the absolute value of the parameter estimate to the standard deviation of the parameter estimate as determined from Equation (4.19). For example, if the SNR is large for a particular parameter, then that parameter is likely to be within the actual parametrization. However, it is not valid to compare the relative likelihood of the AR and MA parameters in being members of the actual parametrization with the SNR as defined here. Consider, for example, a change in the static gain of the actual transfer function relating the measured system input to output. In this case, the actual parametrization is not altered; however, the SNR of the MA parameters are changed, while the SNR of the AR parameters is essentially the same. Therefore, such a comparison between AR and MA parameters would not be consistent under changes in actual static gain. Based on the description here and in Section 4.3.1, the ARMA parameter reduction algorithm may be summarized as follows:

1. Select a maximal model that is believed to include the actual parametrization.

2. Decrease the AR parameters one at a time beginning with a_l (see Equation (4.1)) in order to create a candidate set of reduced models.

3. Choose the candidate reduced model in the set with the minimum MDL value (computed from least squares solution $\hat{\theta}$) as the reduced model.

4. Compute the SNR for each MA parameter of the reduced model.

5. Remove the MA parameters one at a time beginning with the MA parameter with the lowest SNR value in order to create a candidate set of minimal models.

6. Choose the candidate minimal model in the set with the minimum MDL value (computed from least squares solution $\hat{\theta}$) as the selected model.

In order to handle signals with different units, we note that the measured data should be prescaled such that the energy of each signal is the same. Although the selected model from this algorithm is not guaranteed to achieve optimality in terms of the minimum possible MDL value, the algorithm has been demonstrated to reduce the corruption due to noise in the transfer function estimates.

4.4 AutoRegressive Spectral Estimation

The data analysis tools presented in Sections 4.1-4.3 may be utilized for power spectral estimation as well. To this end, consider a special case of the ARMA model in Equation (4.1) which includes only the AR parameters as follows:

$$y(t) = \sum_{i=1}^{l} a_i y(t-i) + e(t), \tag{4.27}$$

where $e(t)$ is again assumed to be a white noise process with variance γ^2. The power spectrum of $y(t)$ may be determined analytically from this equation as follows:

$$\Phi_y(\omega) = \frac{\gamma^2}{|1 - \sum_{i=1}^{l} a_i e^{-j\omega}|^2}. \tag{4.28}$$

Hence, we may identify the model of Equation (4.27) according to the parameter reduction algorithm described in Section 4.3.2 in order to obtain $\Phi_y(\omega)$ from Equation (4.28). This approach is referred to as AutoRegressive spectral analysis and is the preferred approach for resolving spectral peaks [53].

Chapter 5

Cardiovascular System Identification

With the data analysis tools established in Chapter 4, we are now ready to present our forward model-based analysis of the cardiovascular system identification method introduced in Section 1.1. The aim of this analysis is to make some useful inferences about the performance of the method with respect to experimental data. We begin this chapter by revisiting the cardiovascular system identification method in order to describe the details of the identified physiologic mechanisms as well as the data analysis (Section 5.1 which is adapted from [59]). We then present our procedure for evaluating this method with the forward model described in Part I (Section 5.2) and based on this procedure, assess the performance of the cardiovascular system identification method against the nominal forward model (Section 5.3). As discussed in Section 1.2, the results of this assessment are only as meaningful as the validity of the nominal forward model. Hence, we next assess the performance of the cardiovascular system identification method against a set of robustness models which reflect our uncertainty in the relevant properties of the nominal forward model (Section 5.4). The cardiovascular system identification method is appealing because it provides a

potential means to track changes in a patient's cardiovascular state over time so as to provide an individualized guidance for therapy. We thus follow the robustness analysis with an assessment of the sensitivity or resolving power of the method in detecting changes in the relevant properties of the forward model (Section 5.5). We conclude by summarizing the major results of the chapter specifically in terms of inferences made about the performance of the method with respect to experimental data (Section 5.6).

5.1 Cardiovascular System Identification Revisited

Recall that our cardiovascular system identification method involves the analysis of fluctuations in noninvasively measured heart rate, arterial blood pressure (ABP), and instantaneous lung volume (ILV) in order to characterize quantitatively the physiologic mechanisms responsible for the couplings between the signals. Figure 5-1 illustrates the model upon which the method is based. The model includes five physiologic coupling mechanisms relating these signals: CIRCULATORY MECHANICS, HR BAROREFLEX, SA NODE, ILV→HR, and ILV→ABP.

CIRCULATORY MECHANICS represents the relationship between cardiac contraction and the generation of the ABP waveform. The input to CIRCULATORY MECHANICS is the pulsatile heart rate (PHR) signal which is defined to be a train of unit-area impulses occurring at the times of contraction of the ventricles (Figure 5-2, middle trace). PHR may be constructed from the times of occurrence of the QRS complexes in the electrocardiogram (ECG). The output from CIRCULATORY MECHANICS is the pulsatile ABP signal. The CIRCULATORY MECHANICS transfer function represents the ABP wavelet generated by a single cardiac contraction. CIRCULATORY MECHANICS is determined by the contractile properties of the heart as well as the mechanical properties of the great vessels and the peripheral circula-

Figure 5-1 Cardiovascular system identification model depicting the physiologic mechanisms responsible for the couplings between fluctuations in heart rate, ABP, and ILV [59].

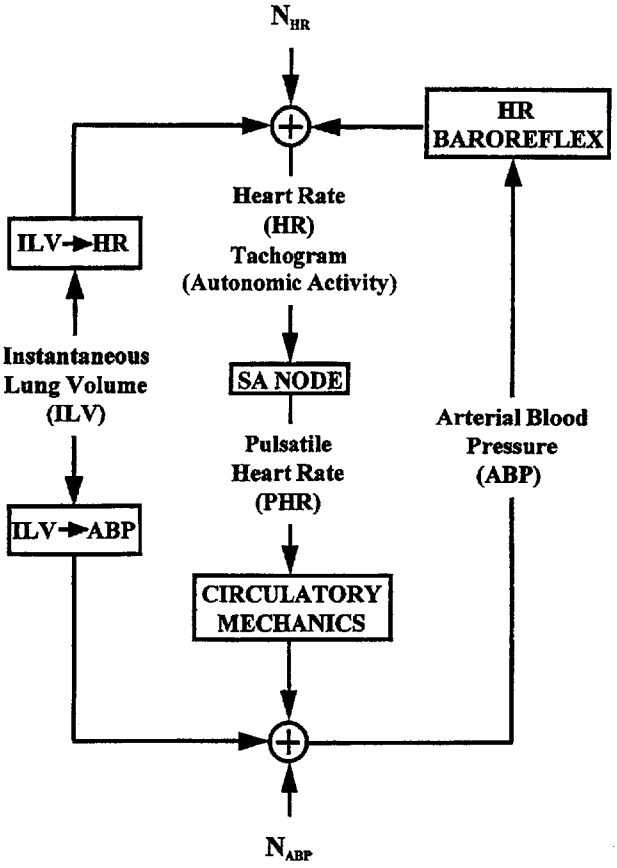

tion. CIRCULATORY MECHANICS may also encompass the reflex adjustment of vascular mechanical properties mediated by the α-sympathetic and renin-angiotensin systems (total peripheral resistance (TPR) baroreflex).

HR BAROREFLEX represents the autonomically mediated baroreflex coupling between fluctuations in ABP and fluctuations in heart rate. Here heart rate is represented by the heart rate tachogram (HR) rather than PHR. HR is defined to be a stepwise continuous process (Figure 5-2, bottom trace) whose value corresponds to the reciprocal of the current inter-beat interval for the time period corresponding to the duration of that interval. Unlike PHR, HR has no periodic component at the mean heart rate frequency and is closely related to the net autonomic input signal

Figure 5-2 Derivation of PHR and HR from the ECG [59].

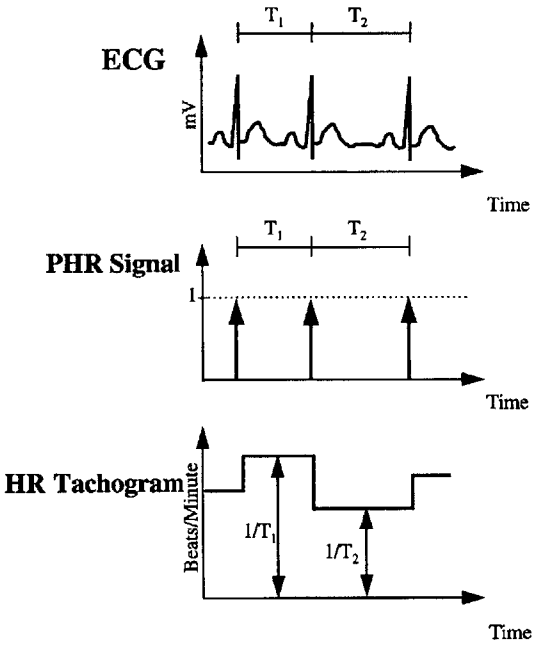

modulating sinoatrial node activity. SA NODE represents the coupling between HR and PHR. The SA NODE in this model is an "integrate and fire" device, such a device precisely relates the input HR to the output PHR. Since the dynamic characteristics of the SA NODE are predefined in this model, the SA NODE is not identified from the experimental data. However, it is important to recognize that the SA NODE is a nonlinear element of this model.

ILV→HR represents the autonomically mediated coupling between respiration and HR. ILV→HR is responsible for mediating respiratory sinus arrhythmia. ILV→ABP represents the mechanical effects of respiration on ABP due to the alterations in venous return and the filling of intrathoracic vessels and heart chambers associated with the changes in intrathoracic pressure.

In addition to the five coupling mechanisms, the model incorporates two perturbing noise sources, N_{HR} and N_{ABP}. N_{HR} represents the fluctuations in HR not caused by fluctuations in ABP or ILV. Such fluctuations may result, for example, from autonomically mediated perturbations driven by cerebral activity. N_{ABP} represents fluc-

tuations in ABP not caused by PHR or fluctuations in ILV. Such ABP fluctuations may result, for example, from fluctuations in TPR as tissue beds adjust local vascular resistance in order to match local blood flow to demand or from beat-to-beat fluctuations in stroke volume. Other physiological inputs, exclusive of baroreceptor and lung volume feedback mechanisms, could contribute to N_{ABP} through fluctuations in TPR mediated by the α-sympathetic system or possibly the renin-angiotensin system and other mediators of TPR. The perturbations represented by N_{HR} and N_{ABP} as well as the variability in ILV are responsible for driving all fluctuations in HR and ABP through the coupling mechanisms. N_{HR} and N_{ABP} are not directly measured quantities. They represent the residual variability in HR and ABP once one subtracts out the components of variability caused by the fluctuations in each case in the other two measured signals.

The model in Figure 5-1 (except for SA NODE which is a predefined, nonlinear "integrate and fire" device) is mathematically represented by a pair of dual-input, ARMA difference equations of the following form:

$$HR(t) = \sum_{i=1}^{m} a_i HR(t-i) + \sum_{i=1}^{n} b_i ABP(t-i) + \sum_{i=p'}^{p} c_i ILV(t-i) + W_{HR}(t) \quad (5.1)$$

$$ABP(t) = \sum_{i=1}^{q} d_i ABP(t-i) + \sum_{i=1}^{r} e_i PHR(t-i) + \sum_{i=s'}^{s} f_i ILV(t-i) + W_{ABP}(t), \quad (5.2)$$

where W_{HR} and W_{ABP} are noise terms referred to as residual errors[1]. The AR and MA parameters of these two equations, which completely characterize the transfer properties of the coupling mechanisms and the power spectra of the perturbing noise sources (see Section 4.1), are estimated from continuous records of ECG, ABP, and

[1]Note that Equations (5.1) and (5.2) impose causality between ABP and heart rate which are related in closed-loop. This is a necessary condition for the distinct identification of HR BAROREFLEX and CIRCULATORY MECHANICS (see Section 4.2.4).

ILV signals (initially digitized at 360 Hz to ensure accurate QRS detection) obtained during the random-interval breathing protocol described in Sections 1.1 and 3.3.1.

In particular, transfer function estimation is performed in two stages corresponding to the two equations. In the first stage, the parameters characterizing the HR BAROREFLEX and ILV→HR transfer relations in Equation (5.1) are estimated with the ARMA parameter reduction algorithm described in Section 4.3.2 (maximal model: $m = 10, n = 5, p' = -5, p = 5$) from approximately six minute segments of zero-mean HR, ABP, and ILV at a sampling frequency of 1.5 Hz[2]. However, in the second stage, the parameters characterizing the ILV→ABP and CIRCULATORY MECHANICS transfer relations are identified in a multi-step manner in order to accommodate for the different bandwidths of the two transfer relations. The ILV→ABP transfer relation may be well characterized by the use of ILV and ABP signals sampled at 1.5 Hz. However, the CIRCULATORY MECHANICS transfer relation requires a wider bandwidth to describe the relationship between PHR and the pulsatile ABP signal. Therefore, signals sampled at 90 Hz were first used to determine the CIRCULATORY MECHANICS transfer relation based on the following equation:

$$ABP_{90}(t) = \sum_{i=1}^{q} d_i ABP_{90}(t-i) + \sum_{i=1}^{r} e_i PHR(t-i) + \sum_{i=s'}^{s} f_i ILV_{90}(t-i) + W_{ABP}(t), \tag{5.3}$$

where the subscript 90 is used to differentiate these signals from their counterparts sampled at 1.5 Hz. The parameters of Equation (5.3) are estimated with the ARMA parameter reduction algorithm (maximal model: $q = 10, r = 35, s' = 0, s = 15$) from 90 second segments of data *with the means included* (see Section 7.1). Although parameters reflecting ILV→ABP are identified as well, an improved characterization

[2]The continuous-time HR, determined from the ECG as described in Figure 5-2, is effectively sampled to 1.5 Hz with an anti-aliasing filter whose impulse response is a unit-area boxcar of $\frac{4}{3}$ second duration. However, the anti-alias filtering here is performed in a manner more efficient than convolution as described in [7].

may be achieved by using a narrower bandwidth matched more closely to that of the true transfer relation as follows. First, the component of ABP due only to PHR ($\mathrm{ABP_{PHR}}$) is calculated using an approximately six minute segment of PHR[3] and the newly found parameters as follows:

$$ABP_{PHR}(t) = \sum_{i=1}^{q} d_i ABP_{PHR}(t-i) + \sum_{i=1}^{r} e_i PHR(t-i). \tag{5.4}$$

This portion is subtracted from the corresponding segment of the $\mathrm{ABP_{90}}$ signal to arrive at the component unexplained by PHR ($\mathrm{ABP_{\overline{PHR}}}$). That is,

$$ABP_{\overline{PHR}}(t) = ABP_{90}(t) - ABP_{PHR}(t). \tag{5.5}$$

$\mathrm{ABP_{\overline{PHR}}}$ and the corresponding $\mathrm{ILV_{90}}$ are decimated to 1.5 Hz and the parameters characterizing the ILV→ABP transfer relation are then determined based on the following single-input ARMA equation:

$$ABP_{\overline{PHR}}(t) = \sum_{i=1}^{u} g_i ABP_{\overline{PHR}}(t-i) + \sum_{i=v'}^{v} h_i ILV(t-i) + W'_{ABP}(t). \tag{5.6}$$

The parameters of this equation are estimated with the ARMA parameter reduction algorithm (maximal model: $u = 10\,, v' = 0\,, v = 10$) from zero-mean data.

To summarize, identification of the parameters of Equation (5.1) provides an accurate characterization of both transfer relations that it describes, because the bandwidths of the two transfer relations are closely matched. Identification of the parameters of Equation (5.2) may result in inaccurate characterizations of one of the two transfer relations it describes, because the bandwidths of the transfer relations are

[3]Since the approximately six minute segment of data includes the 90 second segment used for identification, the assumption here is that the transfer properties of CIRCULATORY MECHANICS changes little over approximately six minutes of stable experimental conditions. We could have avoided making this assumption by identifying CIRCULATORY MECHANICS with approximately six minute segments of data. However, given its relatively wide bandwidth, 90 second segments are sufficient. On the other hand, estimation of the narrower bandwidth ILV→ABP requires the longer, approximately six minute segment of data.

not closely matched. Improved characterizations of the transfer relations described by Equation (5.2) may be attained with a multi-step identification procedure as described above.

From Equation (4.2), the perturbing noise sources, N_{HR} and N_{ABP}, in the closed-loop model may be computed with the estimated AR parameters and residual errors according to the following difference equations:

$$N_{HR}(t) = \sum_{i=1}^{m} a_i N_{HR}(t-i) + W_{HR}(t) \tag{5.7}$$

$$N_{ABP}(t) = \sum_{i=1}^{u} g_i N_{ABP}(t-i) + W'_{ABP}(t). \tag{5.8}$$

Thus, N_{HR} and N_{ABP} represent the actual perturbations added to the HR and ABP signals respectively and are referred to as the actual errors. Power spectra of the perturbing noise sources are then determined according to Equation (4.28).

A typical cardiovascular system identification result for a healthy, standing subject is shown in Figure 5-3. The transfer function estimates are depicted in their time domain form of impulse responses (mean±standard deviation; see Section 4.2.2). These results represent a snapshot of the cardiovascular state of the subject. As an example, let us consider the impulse response estimate characterizing the transfer properties of HR BAROREFLEX. This impulse response represents the response of HR due to a unit-area impulse of ABP given at time zero while ILV is held constant. Here, HR immediately decreases and then returns to baseline demonstrating the expected negative feedback dynamics. A detailed discussion of each of the remaining estimates as well as the effects of posture, pharmacologic autonomic blockade, and diabetic autonomic neuropathy on each of the estimates may be found in [57, 59].

Before we move on to describing our procedure for evaluating the cardiovascular system identification method against the forward model, we first comment on three issues unique to the application of the method to forward model generated data.

Figure 5-3 Cardiovascular system identification results for a standing human subject from [71].

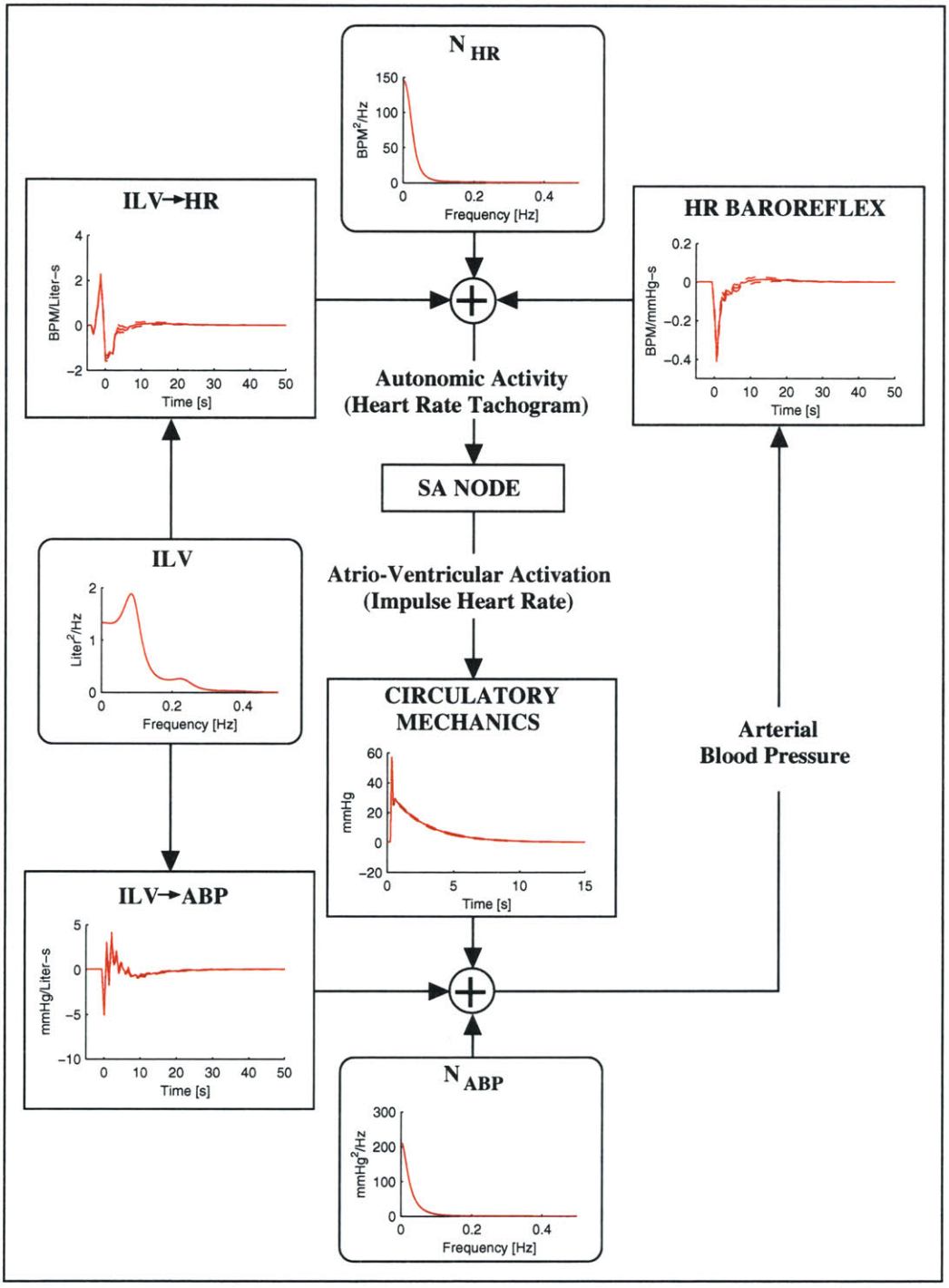

First, in deriving the heart rate signals, it is not possible to determine the times of ventricular contraction via R-wave detection, since the electrical activity of the heart is not modeled here. However, this is not necessary, because these times are precisely known by virtue of forward model implementation. Second, as described in Section 2.3.4, the forward model outputs nonuniformly sampled signals. These signals are uniformly sampled by first linearly interpolating them to form continuous-time processes and then sampling them at 90 Hz (anti-aliasing filter: boxcar of $\frac{1}{45}$ second duration and unit-area). Finally, although we do not consider measurement noise to be too important here (see Section 6.4), we add zero-mean, white noise to each of the relevant signals (effective RR intervals, 90 Hz ABP and ILV) with a standard deviation of one percent of the standard deviation of the signal that it is corrupting. The purpose here is to make the data rich enough particularly for implementation of the ARMA parameter reduction algorithm to 90 Hz data.

5.2 Evaluation Procedure

In order to assess the performance of the cardiovascular system identification method against forward model generated data, we first establish, in a manner independent of system identification, the impulse responses and power spectra in the model of Figure 5-1 which characterize the forward model. These impulse responses and power spectra may then be regarded as the gold standard or the actual cardiovascular system identification results against which the estimates may be compared. Such a comparison may be facilitated by defining a scalar quantity, or statistic, which reflects how closely each estimate (vector quantity) matches its corresponding gold standard. In this section, we describe procedures for establishing the actual cardiovascular system identification results (Section 5.2.1) and for comparing the estimates with this gold standard based on a scalar, statistical quantity (Section 5.2.2).

5.2.1 Actual Cardiovascular System Identification Results

Our general procedure for determining the actual cardiovascular system identification results characterizing the forward model is quite intuitive. Recall, from Equations (5.1) and (5.2), that each of the impulse responses reflects the output response to a unit-area impulse input at time zero while the fluctuations in the other input and perturbing noise source are set to zero. Hence, in defining each actual impulse response, we apply an impulse input to the forward model while setting the fluctuations in the other identification input and perturbing noise source to zero and measure the output response. Now recall, again from these two equations, that each of the perturbing noise sources represent the output fluctuations while the fluctuations in the two identification inputs are set to zero. So, in defining each of the actual power spectra of perturbing noise sources, we hold the identification inputs constant, measure the relevant signal, and compute its power spectrum.

This general procedure for determining the gold standard is utilized in Section 6.3 as well. It should be noted that, in some cases, the general procedure for determining the actual system identification result is not necessary, since the result is predefined by virtue of forward model implementation. However, in some other cases, determination of the gold standard by our general procedure requires altering the dynamics of the forward model from those dynamics responsible for generating the data analyzed by system identification. Consider, for example, the consequences of setting HR constant as implied above. In these cases, we should expect some deviation between the estimate and the corresponding gold standard to be artifactual as a consequence of our imperfect procedure for determining the gold standard[4]. The fact that our inde-

[4]One may argue that artifactual deviation may also occur as a consequence of the general procedure not being restricted to linear dynamics which is in contrast to the system identification methods considered in this thesis. However, we do not regard this type of deviation as an artifact of the imperfect procedure for determining the actual system identification results. Rather, we view

pendent means for determining actual system identification results sometimes requires nonphysiologic operating conditions emphasizes the power of system identification in quantifying physiologic mechanisms during near normal operating conditions.

In the next six paragraphs, we describe the specific procedure for establishing each of the actual cardiovascular system identification results in the model of Figure 5-1. This description also includes signal processing such that the actual results are sampled analogously to the corresponding estimates which is required by the comparison statistic presented in Section 5.2.2.

The actual CIRCULATORY MECHANICS impulse response, which represents the ABP wavelet that results from a single ventricular contraction, is established through the superposition principle. That is, the forward model is first executed for n ventricular contractions and then $n-1$ ventricular contractions, and the difference in the ABP waveform resulting from each of these executions is defined to be the actual CIRCULATORY MECHANICS impulse response[5]. In particular, the forward model is first executed for n ventricular contractions while $n_{R_a}(t)$ is set to zero and $Q_{lu}(t)$ and $F(t)$ are held constant. The resulting nonuniformly sampled $P_a(t)$ is resampled to 90 Hz as described at the end of Section 5.1. Then, under the same conditions, the forward model is executed for $n-1$ ventricular contractions. The resulting $P_a(t)$, which is resampled to 90 Hz, is subtracted from its corresponding waveform of the first execution to arrive at the actual CIRCULATORY MECHANICS impulse response.

The actual HR BAROREFLEX impulse response is not simply determined by the application of an impulse of ABP to the forward model due to the complications of feedback effects on ABP. Rather, we first isolate HR BAROREFLEX from closed-

this deviation as a true source of estimation error which specifically reflects the extent of validity of our linearity hypothesis (see Section 1.1).

[5]The superposition technique, as opposed to the application of a single ventricular contraction to the forward model, avoids initial condition complications provided that n is chosen to be large enough such that the initial condition effects have died out.

loop operation and then apply the impulse. In particular, HR BAROREFLEX of the forward model is defined by the cascade combination of the static saturation mapping of Equation (3.1) followed by an LTI impulse response defined by a linear combination of the parasympathetic and sympathetic filters in Figure 3-3 with weighting factors provided in Table 3.1 at a sampling frequency of 16 Hz. Since we identify the HR BAROREFLEX impulse response at a sampling frequency of 1.5 Hz, we do not apply a true 16 Hz discrete-time impulse to this cascade system. We instead apply an input that resembles an impulse whose bandwidth is approximately 0.5 Hz and area is the standard deviation of the ABP fluctuations analyzed by cardiovascular system identification (σ_{ABP}). The functional form of this "impulse" is given as follows:

$$\frac{\sigma_{ABP} e^{\frac{-n}{\tau}}}{\tau(1+e^{\frac{-n}{\tau}})^2}, \tag{5.9}$$

where n again represents discrete-time at a sampling frequency of 16 Hz, and τ, which reflects the bandwidth of the "impulse", is set to 0.25[6]. The resulting output is then normalized by σ_{ABP} and resampled from 16 Hz to 1.5 Hz arriving at the actual HR BAROREFLEX impulse response.

The actual ILV→HR impulse response of the nominal forward model is already defined by virtue of its implementation. In particular, this LTI impulse response is defined by a linear combination of the aforementioned parasympathetic and sympathetic filters with weighting factors provided in Section 3.2.3. This impulse response is simply resampled from 16 Hz to 1.5 Hz resulting in the actual ILV→HR impulse response.

The actual ILV→ABP impulse response is determined by applying an impulse of $Q_{lu}(t)$ to the forward model while $n_{R_a}(t)$ is set to zero and $F(t)$ is held constant. Due

[6]The functional form here is the first derivative of the hyperbolic tangent function. This form is chosen for all impulse inputs applied to the forward model in this thesis, because it is differentiable which is, in some cases, a necessary requirement for implementation. Although, differentiability is not an implementation requirement here.

to reasons described above, the precise input applied here is given as follows:

$$Q_{lu}(t) = \frac{\sigma_{ILV} e^{\frac{-t}{\tau}}}{\tau(1+e^{\frac{-t}{\tau}})^2} + Q_{fr}, \tag{5.10}$$

where σ_{ILV} is the standard deviation of the ILV fluctuations analyzed by cardiovascular system identification and $\tau = 0.25$. Note, from Equations (3.7) and (3.9), that implementation here requires the first and second derivatives of Equation (5.10) as well. The resulting nonuniformly sampled $P_a(t)$ from the application of the input is resampled to 90 Hz, normalized by σ_{ILV}, and then decimated to 1.5 Hz with its mean removed arriving at the actual ILV$\rightarrow$ABP impulse response.

The actual N_{HR} perturbing noise source of the nominal forward model is given simply by $n_F(t)$. The power spectrum of this signal may also be determined by virtue of its forward model implementation. In particular, the power spectrum is given by the product of the power spectra of the $1/f$ process ($w_F(t)$) and the magnitude squared frequency response of the filter again defined by a linear combination of the sympathetic and parasympathetic impulse responses with weighting factors provided in Section 3.3.3. Since the signal $w_F(t)$ is generated by passing a white noise process through an LTI filter with an approximate $1/f$ magnitude squared frequency response (see Section 3.3.3), its power spectrum is simply given by the product of the variance of the white noise process (λ^2) with this magnitude squared frequency response.

The actual N_{ABP} perturbing noise source of the forward model is determined by executing the forward model while $F(t)$ and $Q_{lu}(t)$ are held constant and only $n_{R_a}(t)$ is active. The resulting nonuniformly sampled $P_a(t)$ is resampled to 90 Hz and then decimated to 1.5 Hz with its mean removed arriving at the actual N_{ABP} perturbing noise source. Then, the power spectrum of this signal is computed by autoregressive spectral estimation (see Section 4.4). This procedure is actually repeated for 10 different realizations of forward model data, with the average power spectrum over these 10 realizations defined to be the actual power spectrum of N_{ABP}.

Figure 5-4 illustrates the actual cardiovascular system identification results characterizing the nominal forward model as determined by the procedure described here.

5.2.2 Statistic for Comparison

In this section, we define a scalar quantity statistic which reflects how closely each vector quantity estimate resulting from the application of the cardiovascular system identification method to forward model generated data resembles its corresponding gold standard as established in the previous section. The motivation for defining such a statistic is to provide a compact means for evaluating each estimate in order to facilitate the evaluation of the cardiovascular system identification method particularly when considering its performance as a function of parameters characterizing the forward model (see Section 5.4).

As discussed in Section 4.2.2, each of the impulse response estimates are actually random vector quantities. That is, each estimate is not simply a deterministic quantity but rather a stochastic quantity characterized by a mean vector and a covariance matrix reflecting its uncertainty. The corresponding gold standard, on the other hand, is a deterministic vector. Let us refer to the estimate as vector x with mean vector $\hat{x}$ and covariance matrix Λ_x and its corresponding gold standard as vector x_0. Then, our scalar comparison statistic, which we refer to as the normalized mean squared error (NMSE), is defined as follows:

$$\begin{aligned} NMSE(x, x_0) &= \sqrt{\frac{E(x - x_0)^T(x - x_0)}{E x_0^T x_0}} \cdot 100\% \\ &= \sqrt{\frac{trace(\Lambda_x)}{x_0^T x_0} + \frac{(\hat{x} - x_0)^T(\hat{x} - x_0)}{x_0^T x_0}} \cdot 100\%, \end{aligned} \tag{5.11}$$

where $E(\cdot)$ is again the expectation operator and $trace(\cdot)$ is the operator which sums the diagonal elements of its matrix argument. The NMSE may be thought of as representing the percentage error between the estimate and its respective gold standard.

Figure 5-4 Actual cardiovascular system identification results characterizing the nominal forward model. These results are determined independently of system identification.

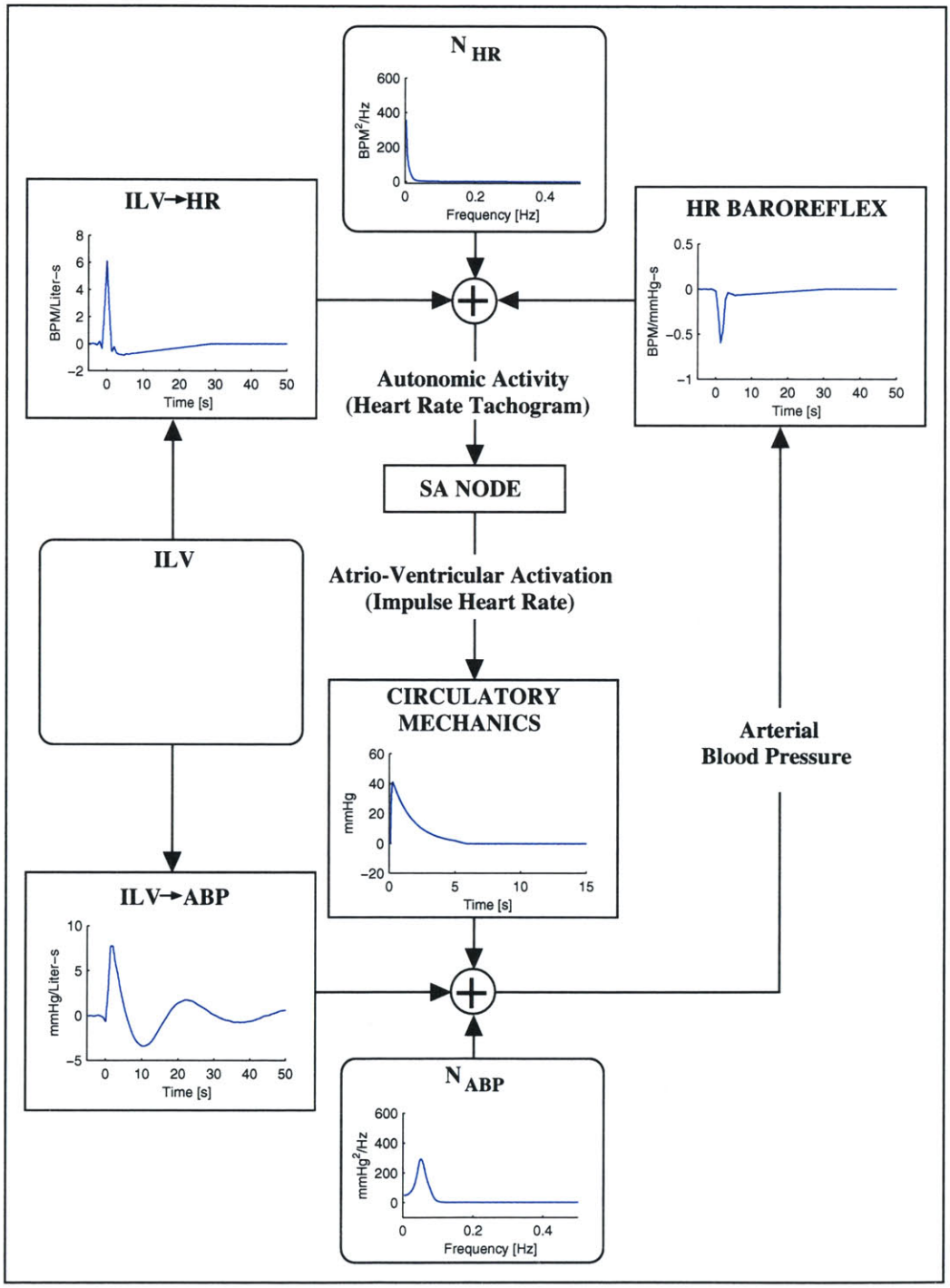

For example, if the estimate were given by x_0 with no uncertainty, then according to the NMSE, there would be 0% deviation between the estimate an gold standard. That is, a perfect estimate with 0% error. If, on the other hand, the estimate were given by a vector of zeros with no uncertainty, then there would be 100% deviation between the estimate and gold standard according to the NMSE. That is, no estimate (impulse response of zeros) would result in 100% error. Note that the NMSE also penalizes the estimate for uncertainty as reflected by Λ_x. In the case of the power spectral estimates in which no measure of uncertainty is available, the matrix Λ_x is assumed to be a matrix of zeros. Hence, the NMSE for the power spectral estimates actually represents a lower bound percentage error.

Although the impulse response estimates include measures of uncertainty in terms of covariance matrices, these uncertainty measures are estimates themselves. Hence, in order to account more accurately for the estimation error variance, in this chapter as well as Chapters 6 and 7, we calculate the NMSE of the estimates for 20 different realizations of forward model generated data and report the resulting mean and standard deviation.

Of course, the cost of the compactness provided by the NMSE statistic, or any other scalar statistic for that matter, is some loss of information. That is, the NMSE does not tell the whole story about how well the estimate matches its gold standard. For example, the NMSE may not be a good indicator of the accuracy of the static gain (the area of the impulse response or equivalently the value of frequency response at the DC frequency) of the impulse response estimate with respect to that of its gold standard. Perhaps, the most comprehensive way to evaluate the estimate is by plotting the mean estimate with its associated standard deviation along side the gold standard as a function of time or frequency. We, in fact, present such plots as well throughout this chapter and the next. Again, in order to account more accurately for the estimation error variance, we report the average estimate over

20 different realizations of forward model generated data along with the associated standard deviation.

5.3 Nominal Forward Model Analysis

We are finally ready to assess the performance of the cardiovascular system identification method against forward model generated data. In this section, we first consider the method with respect to the nominal forward model. Figure 5-5 shows the resulting cardiovascular system identification estimates along with their corresponding gold standard. The results here indicate that the physiologic mechanisms estimated by the cardiovascular system identification method agree quite well with the actual system dynamics of the nominal forward model.

The results of Figure 5-5 are summarized in Table 5.1 in terms of the NMSE of each of the estimates. In comparing the NMSE results with the figure results, we note that the relative NMSE values are a good indicator of which estimates more closely resemble their corresponding gold standard based on visual inspection of the figure. That is, larger NMSE values correspond to deviations between estimates and corresponding gold standards which appear visually larger. However, the absolute NMSE value may be a bit misleading. For example, what one may consider to be a large percentage error (*e.g.*, 51% for HR BAROREFLEX) actually turns out to be quite a reasonable estimate based on visual inspection of the figure. Hence, NMSE results must be considered with some caution. We finally again note that some of the error in the estimates, particularly ILV$\rightarrow$ABP and N_{ABP} may be attributed to the imperfect gold standard (see Section 5.2.1).

Figure 5-5 Cardiovascular system identification estimates (red denotes mean and dashed red denotes standard deviation) with gold standard (blue) as determined from 20 different realizations of data generated by the nominal forward model.

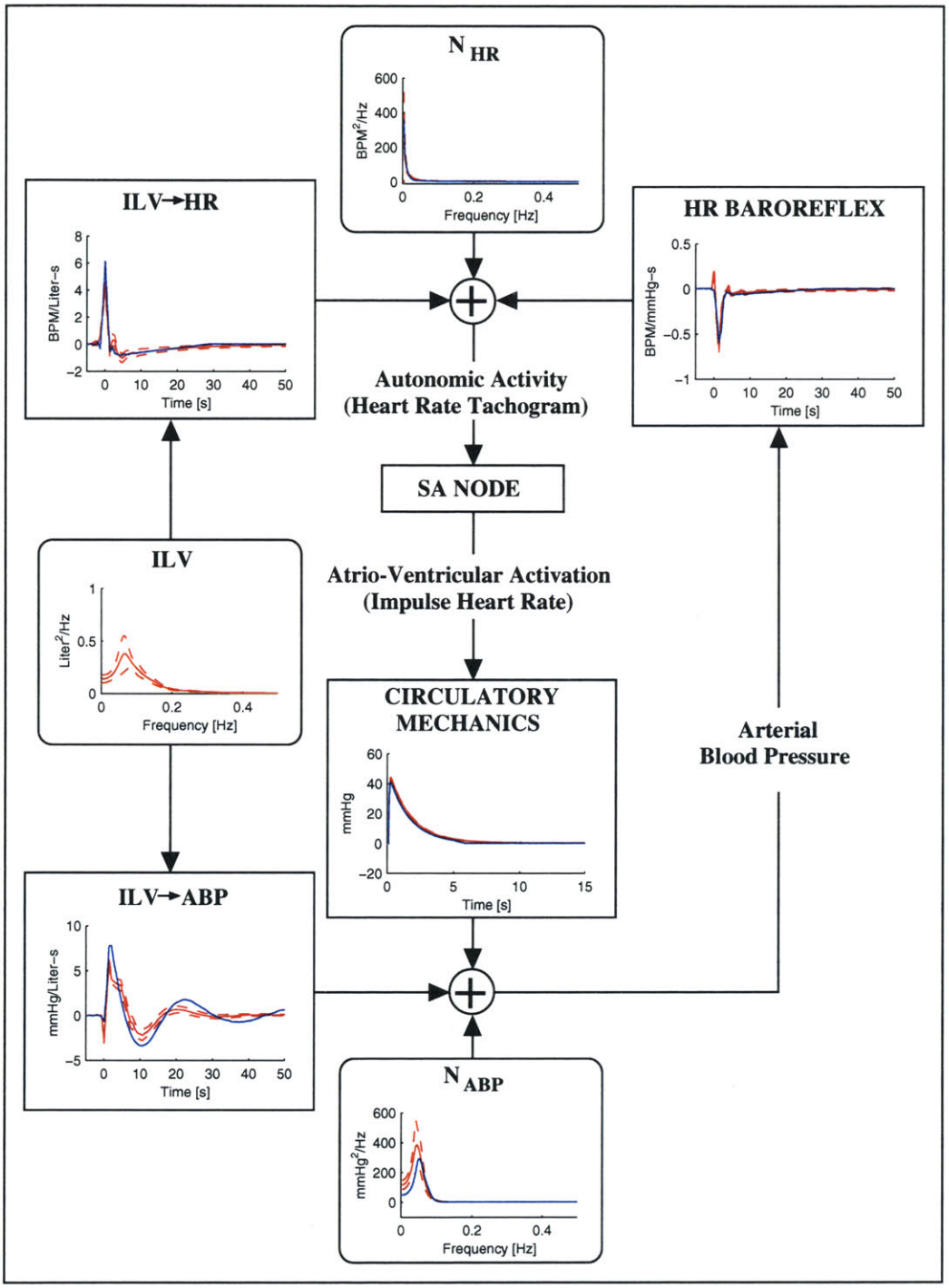

Cardiovascular System Identification Result	NMSE [%]
CIRCULATORY MECHANICS	13±4
HR BAROREFLEX	51±15
ILV→HR	47±11
ILV→ABP	56±7
N_{HR}	55±38
N_{ABP}	65±32

Table 5.1: NMSE results (mean±standard deviation) of the cardiovascular system identification estimates in Figure 5-5.

5.4 Robustness Analysis

The intent of the research described in this chapter is to analyze forward model generated data so as to make some useful inferences about the performance of the cardiovascular system identification method with respect to experimental data. The extent to which the dynamical properties of the forward model resemble those of the actual cardiovascular system determines the validity of any inferences that are made. Although we spent a great deal of effort developing a nominal forward model of the cardiovascular system that is capable of emulating experimental low frequency hemodynamic variability (see Part I), the model cannot possibly be perfect especially when one considers that the dynamical properties of the actual cardiovascular system are not completely understood. Hence, there is some doubt in drawing conclusions about how the cardiovascular system identification method performs on experimental data based only on the nominal forward model analysis of the previous section. In order to attenuate this doubt so as to make more reasonable inferences, we now consider the analysis of the cardiovascular system identification method against a set of robustness models which reflect our uncertainty in the relevant properties of the

nominal forward model. Of course, this analysis is only meaningful provided that the set of robustness models includes the system dynamics of the actual cardiovascular system. That is, the performance of the cardiovascular system identification method over a non-physiologic range does not permit experimental data inferences. Hence, we only consider the robustness of the cardiovascular system identification method against those properties of the forward model in which we have uncertainty but, at the same time, have at least some knowledge based on experimental data of the range of system dynamics or parameter values that characterize it.

Perhaps the major source of uncertainty in the relevant properties of the nominal forward model involves the system dynamics responsible for manipulating heart rate. We particularly have some doubt in the validity of this aspect of the nominal forward model in regards to the omission of the cardiopulmonary heart rate baroreflex, the extent of arterial baroreflex saturation, and the relative contribution of the $1/f$ disturbance to heart rate fluctuations. These properties have been addressed to some extent in the literature; however, uncertainty remains either due to controversial experimental data or great inter-subject variability (see Sections 3.1.2, 3.2.2, and 3.3.3 as well as [17,51,52]). Altering the parameters of the forward model which characterize each of these properties may substantially affect the cardiovascular system identification results of the previous section, especially in regards to HR BAROREFLEX, ILV$\rightarrow$HR, and N_{HR}. We recognize that nonstationarities, other types of nonlinearity excluding baroreflex saturation, and correlated perturbing noise sources (see Section 4.2.4) may also influence the cardiovascular system identification results. However, the stationarity property of the nominal forward model seem quite tenable given that the data are considered over short time periods during stable experimental conditions; other types of system nonlinearities are poorly understood as compared to the ubiquitously reported arterial baroreflex saturation; and there are no experimental data available regarding the extent and manner of correlation between the perturbing noise sources.

In this section, we analyze the robustness of the HR BAROREFLEX, ILV→HR, and N_{HR} estimates against the presence of a cardiopulmonary heart rate baroreflex (Section 3.2.2), the extent of arterial baroreflex saturation (Section 5.4.2), and the size of the $1/f$ heart rate disturbance (Section 5.4.3).

5.4.1 Cardiopulmonary Heart Rate Baroreflex

We now consider the robustness of the HR BAROREFLEX, ILV→HR, and N_{HR} estimates against the inclusion of a cardiopulmonary heart rate baroreflex which is omitted in the nominal forward model by virtue of setting its static gain value to zero (see Table 3.1). Of course, inclusion of this reflex may be achieved by simply adjusting its static gain value to non-zero values. We do not consider any nonlinear interaction with the arterial heart rate baroreflex, because, as discussed in Section 3.2.2, such interaction seems to be insignificant during the relatively stable experimental conditions of cardiovascular system identification data collection.

Before we proceed with this robustness analysis, we note that our gold standard for the N_{HR} power spectrum as established in Section 5.2.1 is no longer valid with the presence of a cardiopulmonary heart rate baroreflex. Recall from this section that the actual N_{HR} perturbing noise source is simply given by the $1/f$ additive heart rate disturbance. However, also recall from Section 5.1 that N_{HR} represents the fluctuations in HR not attributable to ABP and ILV. Hence, the actual N_{HR} in the presence of the cardiopulmonary heart rate baroreflex should encompass fluctuations due to "right atrial" transmural pressure (RATP) as well as the $1/f$ additive heart rate disturbance. We instead experimentally determine the actual N_{HR} power spectrum as follows. In order to keep ABP constant, we consider the forward model with the systemic arterial capacitor replaced by a DC voltage source set to P_a^{sp} (see Table 3.1)[7].

[7] In order to implement this change, we must modify the state-space equations characterizing the heart and circulation. In particular, we remove Equation (2.20) from the state-space equations as

We then execute this modified forward model with $Q_{lu}(t)$ held constant. The resulting nonuniformly sampled $F(t)$ is resampled to 90 Hz and then decimated to 1.5 Hz with its mean removed arriving at the actual N_{HR} perturbing noise source. The power spectrum of this signal is computed analogously to the actual N_{ABP} power spectrum as described in Section 5.2.1. Again note that the procedure here requires alteration of the system dynamics of the forward model.

Figure 5-6a-c shows the NMSE results of the HR BAROREFLEX, ILV→HR, and N_{HR} estimates as a function of the ratio of the static gains of the cardiopulmonary to arterial heart rate baroreflexes. The range of this ratio is chosen based on the discussion in Section 3.2.2. Note that a negative ratio indicates a Bainbridge type of cardiopulmonary baroreflex, while a positive ratio indicates a type of cardiopulmonary baroreflex which contributes to ABP regulation. The results indicate that the ILV→HR impulse response estimate is most significantly and adversely influenced by the presence of the cardiopulmonary heart rate baroreflex. This implies that the almost all the RATP fluctuations are accounted for by ILV. This is not too surprising especially given that intrathoracic pressure, the reference pressure of the "right atrium", precisely follows ILV through the ventilatory model in Figure 3-5. In addition, these respiratory induced intrathoracic pressure fluctuations induce fluctuations to "right atrial" pressure itself.

From Figure 5-6a, we see that the HR BAROREFLEX impulse response estimate is not effected by a positive ratio of the static gains of the cardiopulmonary to arterial heart rate baroreflexes. However, for a negative ratio, the estimate is adversely effected but not as significantly as the ILV→HR impulse response estimate (consider NMSE standard deviation). We believe that this discrepancy between positive and

---

the model is only parametrized by five states now, and replace $P_a(t)$ in Equations (2.25) and (2.26) with P_a^{sp}. In regards to the linear system of equations utilized to determine the initial conditions, we remove Equation (2.37), and replace $P_a(t)$ in Equations (2.31) and (2.32) again with P_a^{sp}.

negative ratios is due to the size of ABP fluctuations. In contrast to the positive ratio which results in tighter ABP regulation, the negative ratio leads to sufficiently large ABP fluctuations such that contribute somewhat to the generation of RATP fluctuations.

Figure 5-6 NMSE results (mean±standard deviation) of the (a) HR BAROREFLEX, (b) ILV→HR, (c) N_{HR}, and (d) redefined ILV→HR estimates as a function of the ratio of the static gains of the cardiopulmonary to arterial heart rate baroreflexes. The results are determined from 20 different realizations of forward model generated data.

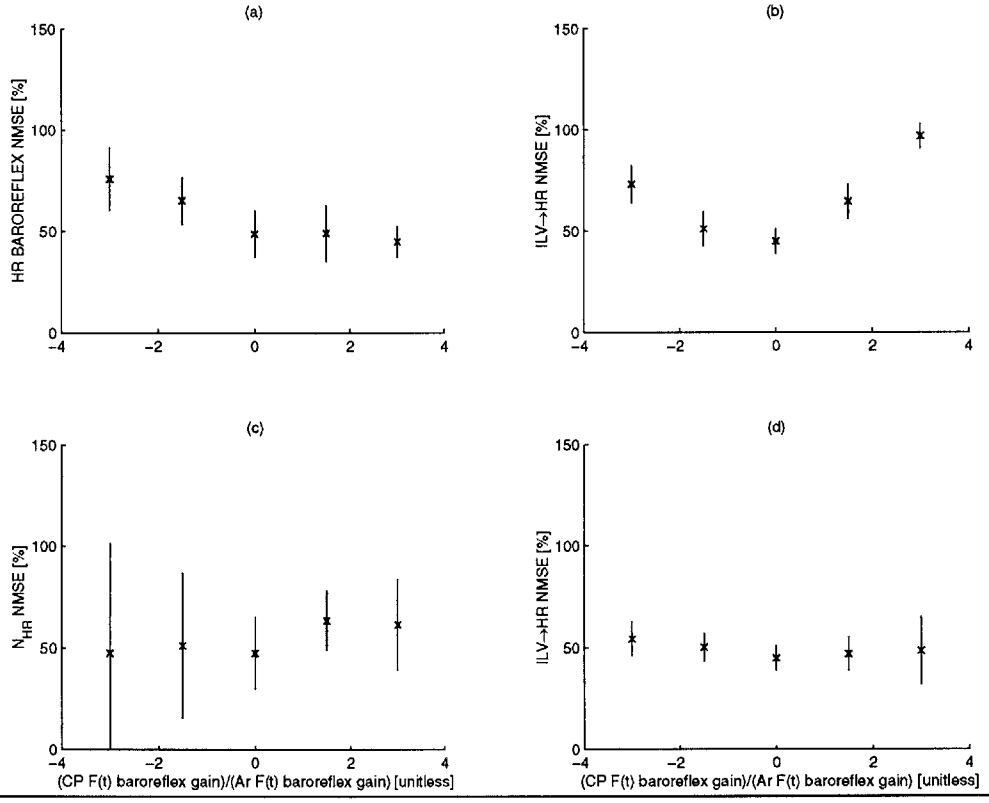

Figure 5-6b illustrates that the ILV→HR estimate becomes progressively worse with respect to its corresponding gold standard as defined in Section 5.2.1 with increasing absolute static gain of the cardiopulmonary heart rate baroreflex. However, this does not necessarily imply that the estimate is less useful for large absolute static gain values. On the contrary, the estimate is quite meaningful regardless of the static gain value of the cardiopulmonary heart rate baroreflex provided that we redefine our gold standard as the heart rate response to an impulse of ILV while ABP is held

constant. This impulse response would not only encompass the direct neural coupling mechanism but the cardiopulmonary heart rate baroreflex as well. We may establish this redefined, actual ILV→HR impulse response as follows. We apply an impulse of $Q_{lu}(t)$ to the forward model with a voltage source in lieu of the systemic arterial capacitor as described previously while $n_F(t)$ and $n_{R_a}(t)$ are set to zero. The actual impulse input is given by Equation (5.10). The resulting nonuniformly sampled $F(t)$ is resampled to 90 Hz, normalized by σ_{ILV}, and then decimated to 1.5 Hz with its mean removed arriving at the redefined actual ILV→HR impulse response.

Figure 5-6d shows the NMSE results of the ILV→HR estimate with respect to this new gold standard again as a function of the ratio of the static gain values of the cardiopulmonary to arterial heart rate baroreflexes. These results demonstrate that the estimate, when considered with respect to the new gold standard, is essentially independent of the static gain of the cardiopulmonary heart rate baroreflex. The results here suggest that when considering the ILV→HR impulse response identified from experimental data, it is probably more accurate to interpret the estimate analogously to the gold standard as redefined here.

5.4.2 Arterial Baroreflex Saturation

The static nonlinear mapping in Equation (3.1) characterizes the degree of arterial baroreflex saturation for the nominal forward model. This mapping provides an upper bound on the deviation between sensed ABP and its setpoint pressure so that the manipulated variables cannot be controlled to arbitrary values. The maximum deviation permitted by this mapping is ~28 mmHg. This pressure is approximately equal to the range of ABP over which the mapping differs from true linearity by only ~10%, that is, the linear ABP range. However, experimental data from one study indicate that the linear ABP range may actually be only ~10 mmHg [51]. The discrepancy between these data and the nominal static saturation mapping, which

was presumably based on experimental data [24], could be due to significant inter-subject variability. This explanation is supported by the experimental data in [51] which suggest that the degree of arterial baroreflex saturation varies, at least to some extent, with setpoint ABP and age. We therefore consider the robustness of the HR BAROREFLEX, ILV→HR, and N_{HR} estimates against more narrow linear ABP ranges. We vary this range simply through the adjustment of the parameter of Equation (3.1) (set to 18 for the nominal model) with the linear range, as defined here, given by the product of the parameter and $\frac{\pi}{2}$.

Figure 5-7 shows the NMSE results of the HR BAROREFLEX, ILV→HR, and N_{HR} estimates as a function of the linear ABP range of the static saturation curve. These results indicate that only the HR BAROREFLEX estimate is significantly and adversely affected by increasing degrees of saturation, a result that was not necessarily obvious prior to the analysis here. Furthermore, the deviation of the NMSE from its nominal value only becomes significant when the extent of saturation is no longer substantiated by the experimental data in [51]. Hence, provided that arterial baroreflex saturation is the only significant nonlinearity, then the assumption that the fluctuations in cardiovascular system identification data are small enough such that the couplings between the fluctuations are related linearly seems quite tenable.

5.4.3 $1/f$ Heart Rate Fluctuations

The unmeasured $1/f$ additive heart rate disturbance $n_F(t)$ represents the noise of the first stage identification problem considered by the cardiovascular system identification method in which the parameters characterizing HR BAROREFLEX, ILV→HR, and N_{HR} are estimated. The relative contribution of this disturbance with respect to the HR fluctuations due to ABP and ILV fluctuations reflects the signal-to-noise ratio (SNR) of this identification problem. This relative contribution, specifically in

Figure 5-7 NMSE results (mean±standard deviation) of the (a) HR BAROREFLEX, (b) ILV→HR, and (c) N_{HR} estimates as a function of the linear ABP range (as defined in the text) of the static saturation curve. This pressure range is approximately equal to the maximum deviation in sensed ABP with respect to its setpoint pressure that is permitted by the static saturation curve. The results are determined from 20 different realizations of forward model generated data.

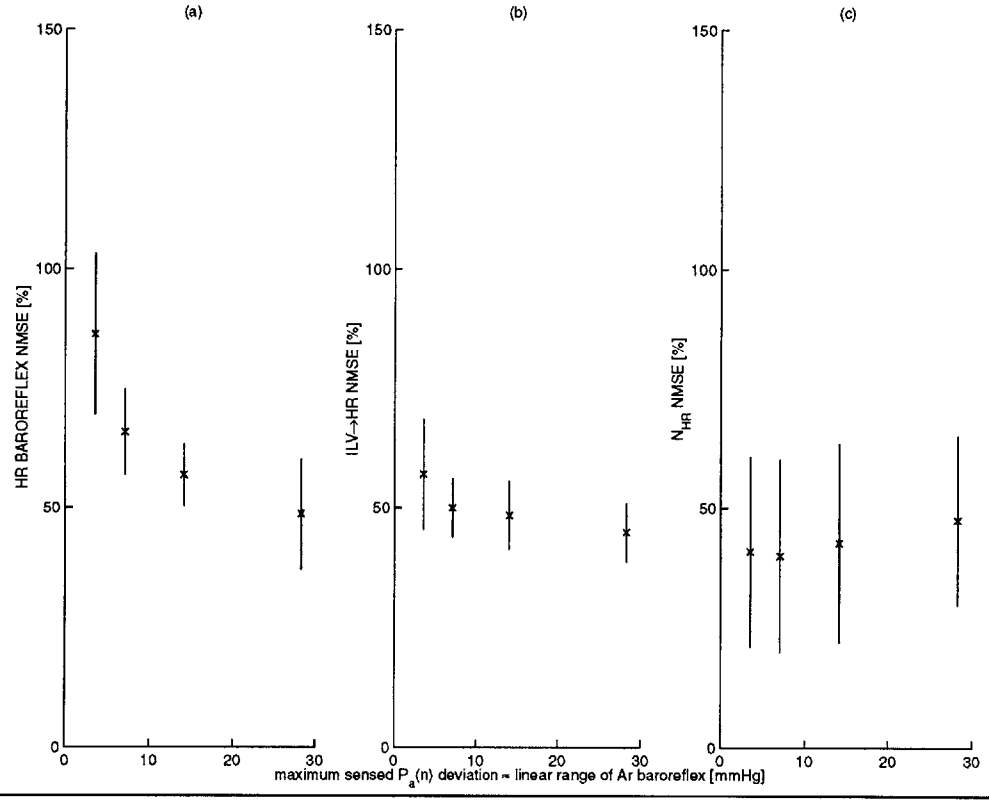

terms of the ratio of the standard deviation of those HR fluctuations not attributed to linear couplings with ABP and ILV to the standard deviation of all HR fluctuations, has been reported to be 0.31±0.14 based on experimental data obtained from humans breathing randomly [17]. However, this value was estimated from only five subjects. Because of the great inter-subject variability in low frequency hemodynamic fluctuations (see Section 3.3.3), there is some uncertainty in this value. Hence, we now consider the robustness of the HR BAROREFLEX, ILV→HR, and N_{HR} estimates against the ratio of the standard deviation of $n_F(t)$ to the standard deviation of $F(t)$ which is varied in the forward model simply through adjustment of λ^2 (see Section 3.3.3).

Figure 5-8 shows the NMSE results of the HR BAROREFLEX, ILV→HR, and N_{HR} estimates as a function of the ratio of the standard deviation of $n_F(t)$ to the standard deviation of $F(t)$. These results indicate that the estimates do not significantly change from the nominal ratio of 0.49±0.07 up to a ratio of ~0.6. That is, the estimates are reliable for a ratio up to the experimentally estimated average ratio plus two standard deviations. Furthermore, we may expect somewhat better reliability in these estimates from experimental data than is indicated by the nominal forward model analysis, since the nominal ratio is over one standard deviation greater than the experimentally estimated average ratio.

Figure 5-8 NMSE results (mean±standard deviation) of the (a) HR BAROREFLEX, (b) ILV→HR, and (c) N_{HR} estimates as a function of the ratio of the standard deviation of $n_F(t)$ to the standard deviation of $F(t)$. The results are determined from 20 different realizations of forward model generated data.

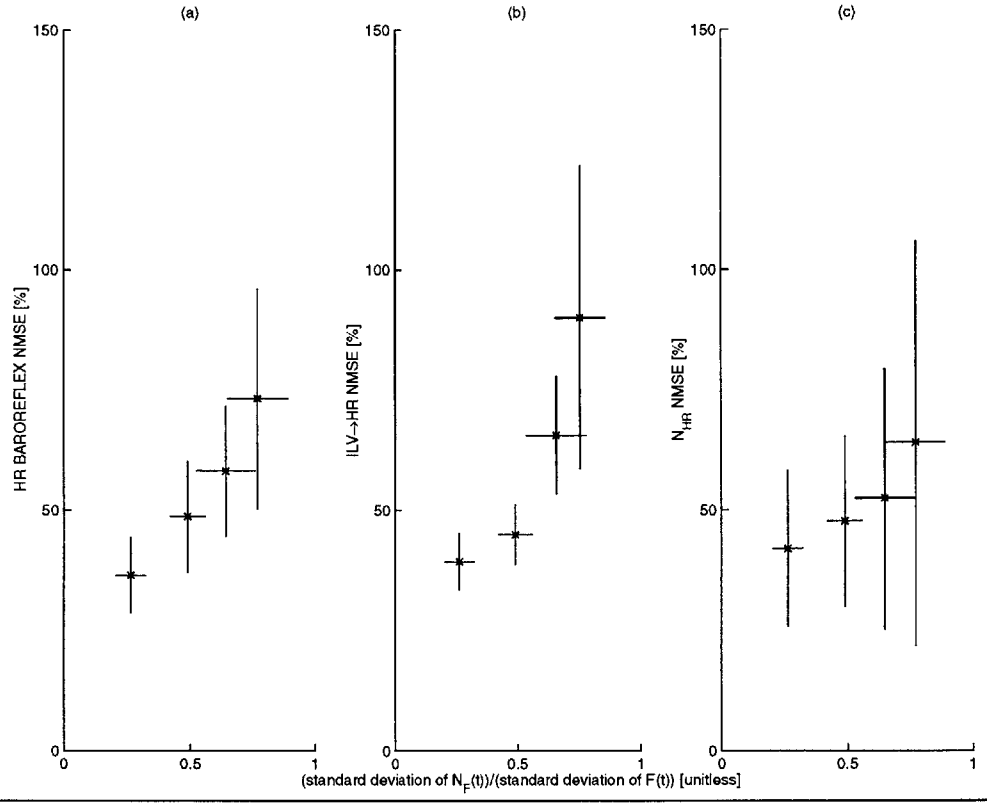

5.5 Sensitivity Analysis

We have repeatedly emphasized throughout this thesis that the ultimate potential of cardiovascular system identification is to provide a clinician with a means to track changes in a patient's cardiovascular state over time so as to guide therapy. An analysis of the sensitivity or resolving power of the method is germane to the realization of this potential. This type of analysis involves determining the extent by which the relevant parameters characterizing the forward model are required to change in order to detect a corresponding change in the cardiovascular system identification estimates. In this section, we specifically consider a sensitivity analysis of the autonomically mediated estimates, HR BAROREFLEX, ILV$\rightarrow$HR, and N_{HR}, in detecting changes in the static gain parameters of the forward model reflecting parasympathetic and β-sympathetic activity (see Table 3.1). It should be noted that we also consider, in Chapter 7, a sensitivity analysis of a modified version of CIRCULATORY MECHANICS in detecting steady-state changes in TPR.

Figure 5-9a and b show the sensitivity results to changes in parasympathetic and β-sympathetic function in terms of the estimated versus actual percentage change in the static gains of the autonomically mediated impulse responses, where percentage change here is with respect to the nominal static gain values[8]. These results indicate that a change of 25% in the static gain of the actual HR BAROREFLEX impulse response is required in order to detect reliably a change in the static gain of the corresponding estimate. On the other hand, a 25% change in the static gain of the actual ILV$\rightarrow$HR impulse response is not sufficient to detect reliably a change in the static gain of the corresponding estimate.

Based on our experience with experimental human data [57, 59], we have found

[8]For simplicity, we neglect the standard deviation of the estimates in establishing the sensitivity results of Figures 5-9, 5-10, and 7-2. However, we account for the error variance by analyzing 20 different realizations of forward model generated data.

that the absolute peak amplitude of the impulse response estimates seems to be quite reliable in detecting changes in autonomic function. Figure 5-9c and d show the sensitivity results in terms of the estimated versus actual percentage change in the absolute peak amplitude of the autonomically mediated impulse responses. Since we vary the static gains of the impulse responses simply via scaling, the actual percentage change in the static gain of the impulse responses is equal to the actual percentage change in the absolute peak amplitude. The results indicate substantial improvement in sensitivity in regards to the ILV→HR estimate and improvement in regards to HR BAROREFLEX. In particular, as small as a 10% change in the absolute peak amplitude of the actual ILV→HR impulse response is sufficient to detect reliably a change in the absolute peak amplitude of the corresponding estimate.

The substantial improvement in the sensitivity of the ILV→HR impulse response here may be explained by considering the spectral content of ILV. It turns out that the ILV fluctuations are not sufficiently broadband to extend to the very low frequencies near DC, a result that is not too surprising when one considers the probability density characterizing the initiation times for a respiratory cycle (see Section 3.3.1). It now becomes evident as to why the static gain of the ILV→HR impulse response estimate, which reflects the DC frequency of the estimate, is not reliable, while the absolute peak amplitude, which reflects the wider bandwidth parasympathetic filter (see Figure 3-3), is quite reliable (see Section 4.2.3). On the other hand, the ABP fluctuations have significant low frequency content due to the system resonance at ~0.07 Hz which explains why the static gain of the HR BAROREFLEX impulse response is reliable.

Figure 5-10 illustrates the sensitivity results in terms of the estimated and actual percentage change in total, low frequency (0-0.15 Hz), and high frequency (0.15-0.4 Hz) power of the N_{HR} spectra. These results emphasize the superior reliability of the high frequency components of the estimates, a result that is not at all surprising when one considers the $1/f$ character of the unmeasured disturbance (see Section 4.2.3).

Figure 5-9 Sensitivity results (red trace; mean±standard deviation) in terms of estimated versus actual percentage change in the (a) static gain of ILV→HR, (b) static gain of HR BAROREFLEX, (c) absolute peak amplitude of ILV→HR, and (d) absolute peak amplitude of HR BAROREFLEX. The percentage change is with respect to the nominal values. The results are determined from 20 different realizations of forward model generated data. The blue trace denotes the identity line.

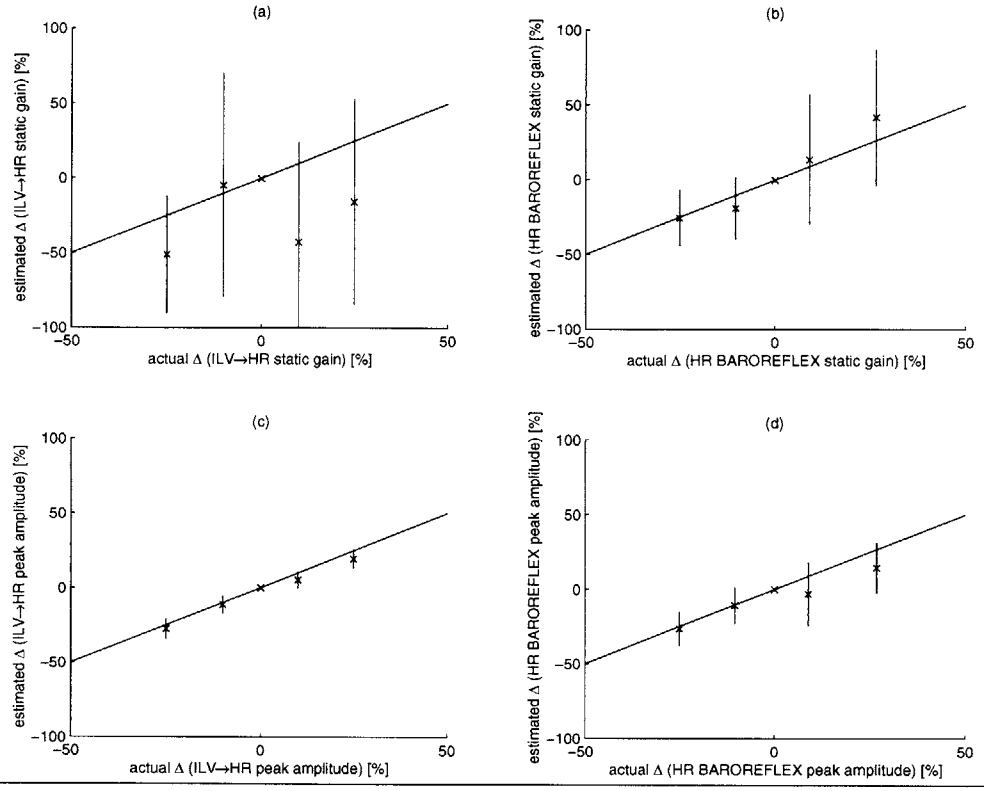

Note that the high frequency power of N_{HR} is just as sensitive a measure of parasympathetic function as the absolute peak amplitude of ILV→HR. However, we believe that this absolute peak amplitude may be a better measure of parasympathetic function, because the perturbing noise source N_{HR}, unlike ILV→HR, is not normalized for inputs (*e.g.*, higher brain center activity).

From experimental human data [57, 59], we have found the absolute peak amplitude of ILV→HR to be the most sensitive measure of autonomic function, followed by the power of the N_{HR} spectra (especially the high frequency power), the absolute peak amplitude of HR BAROREFLEX, and the static gain of HR BAROREFLEX. In contrast, we have never found the static gain of ILV→HR to be predictive of changes

Figure 5-10 Sensitivity results (red trace; mean±standard deviation) in terms of estimated versus actual percentage change in the (a) total power, (b) low frequency power (0.0-0.15 Hz), and (c) high frequency power (0.15-0.4 Hz) of the N_{HR} spectra. The percentage change is with respect to the nominal values. The results are determined from 20 different realizations of forward model generated data. The blue trace denotes the identity line.

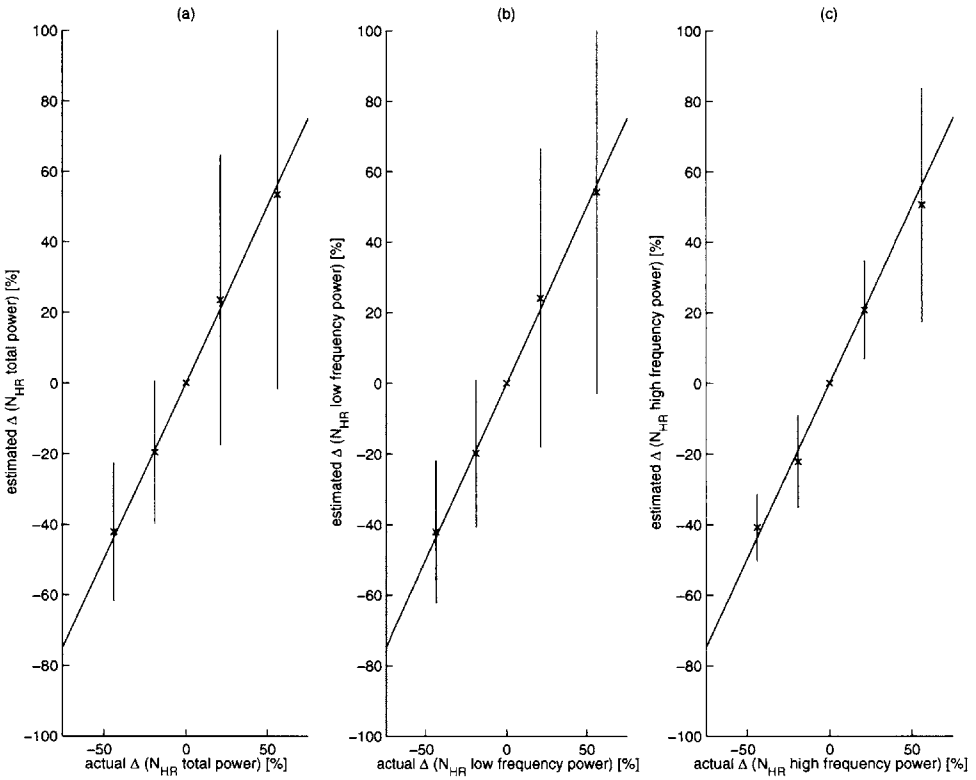

in autonomic function. The fact that the more precise analysis here retrospectively predicts the sensitivity of the estimates determined from experimental human data helps confirm the validity of the low frequency hemodynamic fluctuations generated by the forward model during random-interval breathing.

In addition to the static gain and absolute peak amplitude of the impulse response estimates, a third scalar parameter that we have considered for detecting autonomic changes in experimental human data [57, 59], referred to as the characteristic time parameter, is defined as follows:

$$\frac{\sum_{k=-\infty}^{\infty} kT_s|h(k)|}{\sum_{k=-\infty}^{\infty}|h(k)|}, \tag{5.12}$$

where $h(k)$ is the estimated impulse response and T_s is its sampling period. Changes

in this parameter essentially reflect shifts in balance between parasympathetic and β-sympathetic function. For example, simply scaling the impulse response, as we have done here, does not change the characteristic time because there is no shift in balance in the activity of the two autonomic limbs. Based on the interpretations made here, we expect the ILV→HR impulse response estimate to be unable to measure true shifts in balance through the characteristic time parameter, because only the parasympathetic limb can be estimated accurately. However, we do expect the characteristic time parameter of the HR BAROREFLEX impulse response estimate to be a somewhat sensitive measure of true shifts in balance between parasympathetic and β-sympathetic function. The validity of these expectations is supported by our analysis with experimental human data [57, 59] in which only the characteristic time parameter of the HR BAROREFLEX impulse response estimate was found to be sensitive to changes in autonomic function.

5.6 Summary

Based on the results of the forward model-based analysis of the cardiovascular system identification method in this chapter, we now draw inferences to the performance of the method with respect to experimental data as follows:

1. Each of the cardiovascular system identification estimates is likely to reflect the system dynamics of actual physiologic mechanisms.

2. The ILV→HR impulse response estimate encompasses both direct neural coupling and cardiopulmonary heart rate baroreflex mechanisms.

3. Arterial baroreflex saturation and the relative contribution of the HR fluctuations independent of ABP and ILV fluctuations are unlikely to affect significantly the autonomically mediated estimates.

4. The absolute peak amplitude of the ILV→HR impulse response estimate is a very sensitive measure of parasympathetic function.

5. The HR BAROREFLEX impulse response estimate is a reasonably sensitive measure of both parasympathetic function (through the absolute peak amplitude, static gain) and β-sympathetic function (through the static gain) and consequently, shifts in balance between the two autonomic limbs (through characteristic time).

Chapter 6

TPR Baroreflex Identification From CO and ABP

In Chapter 5, we validated our previously developed cardiovascular system identification method against the forward model of Part I. As a first step towards extending this method, we now consider the practical identification of the total peripheral resistance (TPR) baroreflex. By TPR baroreflex, we refer to the feedback pathways of the arterial and cardiopulmonary baroreflex arcs which respectively couple arterial blood pressure (ABP) fluctuations to TPR fluctuations (arterial TPR baroreflex) and right atrial transmural pressure (RATP) fluctuations to TPR fluctuations (cardiopulmonary TPR baroreflex). In this chapter, we specifically present the analysis of two identification methods which require only left ventricular flow rate (cardiac output, CO) and ABP signals for the quantitative characterization of physiologic coupling mechanisms which encompass TPR baroreflex dynamics.

We begin with a brief review of some of the previously employed approaches for the quantification of the peripheral resistance baroreflex in humans which motivate the research described in this chapter (Section 6.1). We then provide a detailed presentation of the two practical identification methods (Section 6.2). Next, we establish the

gold standard forward model results for the two identification methods (Section 6.3), and based on these results, assess their performance against the forward model (Section 6.4). Finally, we complement this forward model analysis by considering the two identification methods with respect to experimental human data (Section 6.5).

6.1 Previous Approaches

Over the past 40 years, there have been numerous studies which have investigated the role of the arterial and cardiopulmonary peripheral resistance baroreflex systems in humans [51, 52]. These studies have essentially involved perturbing the systems in a highly nonphysiologic manner in order to elicit a reflex peripheral resistance response. Two of the most commonly employed techniques for perturbing the systems have been the neck chamber and lower body negative pressure (LBNP). The neck chamber technique, which is used to study the arterial baroreflex, involves stimulation (or inhibition) of the carotid baroreceptors with suction pressure (or positive pressure) produced by a device placed on the neck. The LBNP technique involves the application of suction pressure to the lower body in order to simulate gravitational shifts of blood. This technique has been used to analyze the cardiopulmonary baroreflex which is considered to be exclusively perturbed when the suction pressure applied to the lower body is small (> -20 mmHg) [52].

Using these types of techniques, many studies have addressed the influence of the arterial and cardiopulmonary baroreflex systems on regional circulations of humans. For example, one study concluded that the arterial baroreflex plays a more important role in modulating peripheral resistance in the splanchnic bed, while the cardiopulmonary baroreflex is more critical in manipulating peripheral resistance in skeletal muscle [39]. Another study demonstrated that significant inhibition of the cardiopulmonary baroreflex actually induces an increase in the gain of arterial barore-

flex system manipulating peripheral resistance in skeletal muscle [86]. That is, the two baroreflex systems are nonlinearly coupled.

Several studies have also analyzed the role of the arterial baroreflex in the manipulation of TPR. Although a significant role has been more clearly demonstrated in animal preparations (*e.g.*, [72,78]), there is some controversy over this role in humans. In particular, some studies have found no change in TPR after stimulating the carotid baroreceptors, while other studies have found a decrease in TPR after stimulation [51]. Nevertheless, arterial baroreflex manipulation of TPR is generally considered to play a significant role in the maintenance of ABP in humans via the α-sympathetic nervous system [32,51].

Unfortunately, most of the previous studies only provide indirect or incomplete evidence of the role of the baroreflex systems in manipulating peripheral resistance in humans. In particular, the conclusions of many of these studies is based on the premise that the baroreceptors under study were exclusively perturbed; this was unlikely to be the case in most, if not all, the studies [51]. Additionally, the previous studies provide little dynamical information, nor do they explain the integrated role of the two baroreflex systems during normal physiologic conditions. However, system identification may provide a viable means to distinguish each baroreflex system as they are being simultaneously perturbed during the near physiologic experimental conditions of random-interval breathing.

6.2 Identification Methods

If the fluctuations in ABP, RATP, and TPR were readily available from measurement, the development of a TPR baroreflex identification method would be straightforward. However, in practice, the direct measurement of TPR fluctuations is not possible. In order to circumvent this limitation, in Section 6.2.1, we describe, at the conceptual

level, two identification strategies which require only CO, ABP, and RATP signals. Although it is possible to obtain RATP in humans via a central venous catheter and esophageal balloon, these measurement techniques are invasive and typically do not reliably account for RATP fluctuations on a beat by beat basis. Consider, for example, the consequences of swallowing with respect to an esophageal balloon measurement. However, it is possible to measure fluctuations in CO and ABP noninvasively and reliably in humans with, for example, Finapres and Doppler ultrasound[1] techniques, respectively (see Sections 1.1 and 1.3). Hence, in Section 6.2.2, we consider left ventricular stroke volume (SV) fluctuations (which may be obtained from the CO measurement [2]) as a surrogate for RATP fluctuations in order to adapt each of the two strategies to require just CO and ABP signals. Finally, in Sections 6.2.3 and 6.2.4, we present the details of two identification methods based on the adapted strategies including the physiologic mechanisms to be identified and data analysis techniques.

6.2.1 Two Identification Strategies

The first strategy that we consider for TPR baroreflex identification is the most obvious. This strategy, which we refer to as direct identification, consists of two steps. The first step deals with the estimation of TPR fluctuations from other measurable signals, namely CO and ABP (see Section 6.2.3). The second step involves the analysis of the fluctuations in ABP, RATP, and estimated TPR ($\widehat{\text{TPR}}$) in order to identify the two TPR baroreflex mechanisms depicted in the model in Figure 6-1. This model is derived from the TPR manipulation scheme of the nominal forward

[1] To be precise, it is possible to measure the *relative* fluctuations in CO with respect to its mean value using a Doppler ultrasound technique [29].

[2] This requires the determination of heart rate fluctuations from the CO measurement. Although this is realizable, in practice, it is easier to determine heart rate fluctuations from the ECG. We, in fact, choose this latter approach in this chapter while maintaining that the identification methods considered here may be implemented with only CO and ABP measurements.

model (see Figure 3-7). Ar TPR BAROREFLEX specifically represents the feedback pathway of the arterial baroreflex arc responsible for coupling ABP fluctuations to TPR fluctuations, while CP TPR BAROREFLEX represents the feedback pathway of the cardiopulmonary baroreflex arc responsible for coupling RATP fluctuations to TPR fluctuations. The model also includes a perturbing noise source N_{TPR} which is not measured and represents the fluctuations in TPR not attributed to the TPR baroreflexes such as autoregulation of local vascular beds.

Figure 6-1 Model depicting the direct identification strategy. The model represents the feedback mechanisms responsible for the couplings between the fluctuations in ABP, RATP, and $\widehat{TPR}$.

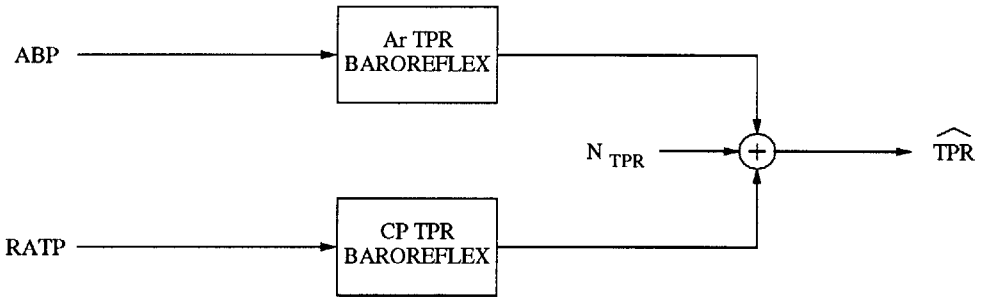

The second strategy that we consider for TPR baroreflex identification, which we refer to as indirect identification, extracts information pertaining to the TPR baroreflex essentially through its correlation with other measurable signals. The advantage of this strategy over the direct identification strategy is that it is not hampered by the imperfect estimation of TPR fluctuations (see Section 6.2.3). However, as described in the next paragraph, in contrast to the direct identification strategy, the physiologic coupling mechanisms of the indirect identification strategy do not isolate TPR baroreflex system dynamics.

The indirect identification strategy specifically involves the analysis of the fluctuations in CO, RATP, and ABP in order to identify the physiologic mechanisms illustrated in the model in Figure 6-2. The model includes two coupling mechanisms, CO→ABP and RATP→ABP. CO→ABP represents the transfer properties relating CO fluctuations to ABP fluctuations which encompass both systemic arte-

rial tree dynamics and the arterial TPR baroreflex. That is, CO fluctuations directly induce ABP fluctuations through the systemic arterial tree which in turn excites the arterial TPR baroreflex arc. RATP→ABP represents the transfer properties relating RATP fluctuations to ABP fluctuations which encompass these two distinct physiologic mechanisms as well as the cardiopulmonary TPR baroreflex. In particular, RATP fluctuations induce TPR fluctuations through the cardiopulmonary TPR baroreflex which in turn induces ABP fluctuations through the systemic arterial tree thus exciting the arterial TPR baroreflex arc. The model also incorporates a perturbing noise source N'_{ABP} which is not measured and represents the fluctuations in ABP not attributed to CO and RATP fluctuations. These fluctuations may be due to, for example, autoregulation of local vascular beds.

Figure 6-2 Model depicting indirect identification strategy. The model relates couplings between the fluctuations in CO, RATP, and ABP. These couplings encompass the arterial and cardiopulmonary TPR baroreflexes as well as systemic arterial tree dynamics.

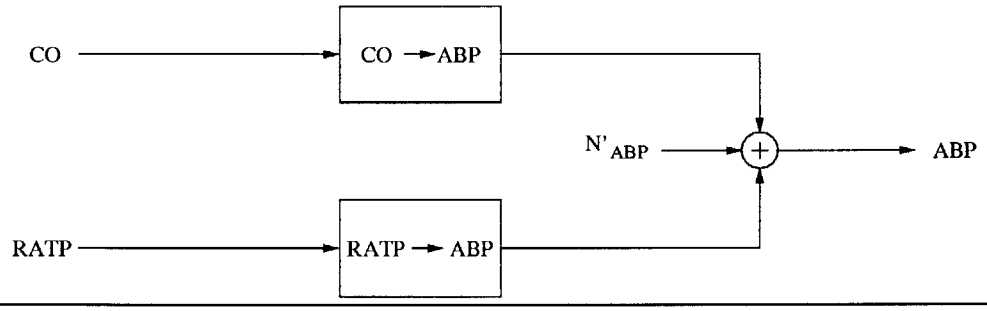

In order to obtain a more precise, quantitative understanding of the system dynamics characterizing each of the physiologic mechanisms in Figure 6-2, we develop a dynamical equation relating the fluctuations in CO, RATP, and ABP based on the governing equations of the nominal forward model as follows. Since C_v in the nominal forward model is large relative to C_a (see Table 2.1), $P_v(t)$ may be assumed to be negligible with respect to $P_a(t)$ (see Figure 2-1). Hence, the model in Figure 6-3 provides an even more simple representation of the systemic circulation of the nominal forward model. The model also includes an ideal current source which represents the outflow

rate of the left ventricle. The following nonlinear, differential equation characterizes this model:

$$\dot{q}_l(t) = C_a \frac{d}{dt} P_a(t) + \frac{P_a(t)}{R_a(t)}. \tag{6.1}$$

Figure 6-3 Simple RC circuit model of the systemic circulation assuming that $C_v >> C_a$. The ideal current source represents the left ventricle.

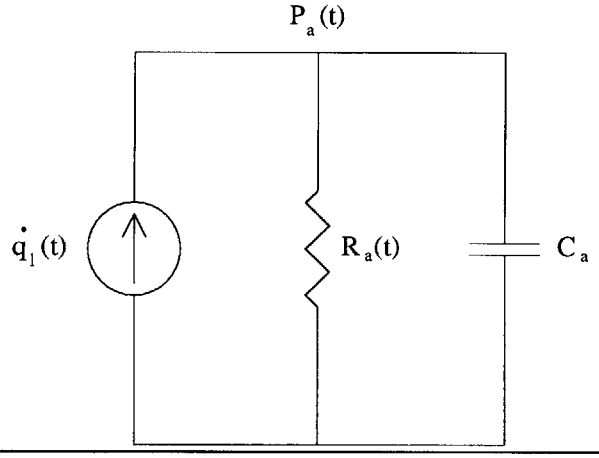

By removing mean values from this equation, normalizing it by the mean left ventricular flow rate, and neglecting second order terms, the following linear, dynamical equation results:

$$\frac{\Delta \dot{q}_l(t)}{\overline{\dot{q}_l}} = \overline{R_a} C_a \frac{d}{dt} \frac{\Delta P_a(t)}{\overline{P_a}} + \frac{\Delta P_a(t)}{\overline{P_a}} - \frac{\Delta R_a(t)}{\overline{R_a}}, \tag{6.2}$$

where, if we let $X(t)$ represent any of the three signals in Equation 6.1, then $\overline{X}$ and $\frac{\Delta X(t)}{\overline{X}}$ respectively denote the mean value of $X(t)$ and its relative fluctuations with respect to its mean value. This linear, constant coefficient differential equation may be equivalently written as a sum of convolutions as follows:

$$\frac{\Delta P_a(t)}{\overline{P_a}} = \int_0^\infty h(\tau) \frac{\Delta \dot{q}_l(t-\tau)}{\overline{\dot{q}_l}} d\tau + \int_0^\infty h(\tau) \frac{\Delta R_a(t-\tau)}{\overline{R_a}} d\tau, \tag{6.3}$$

where

$$h(t) = \frac{1}{\overline{R_a} C_a} e^{\frac{-t}{\overline{R_a} C_a}} \quad t \geq 0 \tag{6.4}$$

and completely characterizes the systemic arterial tree dynamics. We may discretize this equation by choosing the sampling interval T_s such that the two inputs of the equation are essentially constant over the interval. The following sum of discrete-time convolutions results:

$$\frac{\Delta P_a(k)}{\overline{P_a}} = \sum_{i=0}^{\infty} h_{T_s}(i) \frac{\Delta \dot{q}_l(k-i)}{\overline{\dot{q}_l}} + \sum_{i=0}^{\infty} h_{T_s}(i) \frac{\Delta R_a(k-i)}{\overline{R_a}}, \tag{6.5}$$

where k is discrete-time and $h_{T_s}(k)$ is given by

$$h_{T_s}(k) = \int_{kT_s}^{(k+1)T_s} h(\tau) d\tau. \tag{6.6}$$

We may rewrite Equation (6.5) more compactly with the delay operator notation introduced in Section 4.1 as follows:

$$\frac{\Delta P_a(k)}{\overline{P_a}} = H(q^{-1}) \frac{\Delta \dot{q}_l(k)}{\overline{\dot{q}_l}} + H(q^{-1}) \frac{\Delta R_a(k)}{\overline{R_a}}, \tag{6.7}$$

where

$$H(q^{-1}) = h_{T_s}(0) + h_{T_s}(1) q^{-1} + h_{T_s}(2) q^{-2} + \cdots \tag{6.8}$$

and is referred to as the transfer function operator reflecting systemic arterial tree dynamics.

From Figure 3-7, the equation governing the manipulation of the relative fluctuations in TPR in the nominal forward model may be given as follows:

$$\frac{\Delta R_a(k)}{\overline{R_a}} = \frac{\overline{P_a}}{\overline{R_a}} A(q^{-1}) \frac{\Delta P_a(k)}{\overline{P_a}} + \frac{\overline{P^{tr}_{\text{“}ra\text{”}}}}{\overline{R_a}} C(q^{-1}) \frac{\Delta P^{tr}_{\text{“}ra\text{”}}(k)}{\overline{P^{tr}_{\text{“}ra\text{”}}}} + \frac{n_{R_a}(k)}{\overline{R_a}}, \tag{6.9}$$

that is, provided that the fluctuations in the signals are sufficiently small. In this equation, the transfer function operators $A(q^{-1})$ and $C(q^{-1})$ respectively characterize the arterial and cardiopulmonary TPR baroreflexes defined in terms of impulse responses in Figure 3-3 and Table 3.1, while $n_{R_a}(k)$ represents the additive TPR disturbance as defined in Section 3.3.2. Note that the two transfer function operators

and TPR disturbance as defined in Sections 3.2 and 3.3 must be resampled here in order to accommodate the different sampling interval.

By substituting this equation into Equation (6.7) and rearranging terms, the following dynamical equation relating the relative fluctuations in CO, RATP, and ABP results:

$$\frac{\Delta P_a(k)}{\overline{P_a}} = H_1(q^{-1})\frac{\Delta \dot{q}_l(k)}{\overline{\dot{q}_l}} + H_2(q^{-1})\frac{\Delta P^{tr}_{\text{“}ra\text{”}}(k)}{\overline{P^{tr}_{\text{“}ra\text{”}}}} + H_1(q^{-1})\frac{n_{R_a}(k)}{\overline{R_a}}, \tag{6.10}$$

where

$$H_1(q^{-1}) = \frac{H(q^{-1})}{1 - \frac{\overline{P_a}}{\overline{R_a}}A(q^{-1})H(q^{-1})} \tag{6.11}$$

$$H_2(q^{-1}) = \frac{\frac{\overline{P^{tr}_{\text{“}ra\text{”}}}}{\overline{R_a}}C(q^{-1})H(q^{-1})}{1 - \frac{\overline{P_a}}{\overline{R_a}}A(q^{-1})H(q^{-1})}. \tag{6.12}$$

The transfer function operators, $H_1(q^{-1})$ and $H_2(q^{-1})$, precisely reveal the interconnections of the systemic arterial tree dynamics and the arterial and cardiopulmonary TPR baroreflexes which characterize CO→ABP and RATP→ABP in Figure 6-2, respectively. Note that the last term in Equation (6.10) represents the perturbing noise source $\mathrm{N}'_{\mathrm{ABP}}$ in Figure 6-2.

Equations (6.10)-(6.12) not only provide us with a precise, quantitative understanding of the system dynamics characterizing the physiologic mechanisms in Figure 6-2, but they also indicate the recipe for recovering information pertaining to the arterial and cardiopulmonary TPR baroreflexes from the transfer function operators representing these physiologic mechanisms. In particular, the transfer properties characterizing the cardiopulmonary TPR baroreflex may be completely recovered as follows:

$$C(q^{-1}) = \frac{\overline{R_a}}{\overline{P^{tr}_{\text{“}ra\text{”}}}}\frac{H_2(q^{-1})}{H_1(q^{-1})}. \tag{6.13}$$

The static gain of the arterial TPR baroreflex ($A(q^{-1}=1)$) may be determined as follows:

$$A(q^{-1}=1)=\frac{\overline{R_a}}{\overline{P_a}}\frac{H_1(q^{-1}=1)-1}{H_1(q^{-1}=1)}, \tag{6.14}$$

where, from Equations (6.4) and (6.6), $H(q^{-1}=1)$=1. It may be possible to recover dynamical information characterizing the arterial TPR baroreflex by assuming, for example, that the bandwidth of $H(q^{-1})$ is much greater than the bandwidth of $A(q^{-1})$[3]. That is, $H(q^{-1})\approx 1$ over the bandwidth of $A(q^{-1})$.

6.2.2 SV as a Surrogate for RATP

We now consider SV fluctuations as a surrogate for RATP fluctuations so as to adapt the direct and indirect identification strategies to require only CO and ABP signals. This consideration is motivated by the experimental result in Figure 2-9 which demonstrates that, in the steady-state, SV is determined exclusively by RATP provided that mean ABP is less than ~180 mmHg. Moreover, we hypothesize that the fluctuations in RATP are largely responsible for the fluctuations in SV as well. That is, SV fluctuations are largely indicative of RATP fluctuations. This hypothesis is based on the following arguments. Since ventricular contractility changes little during stable experimental conditions (see Table 3.1), the two major determinants of SV fluctuations are fluctuations in left atrial pressure (preload) and ABP (afterload). However, left

[3]It should be noted that Equation (6.10) may also be formulated as an AutoRegressive Moving Average eXogenous input (ARMAX) equation [47,79]. This equation is more sophisticated than an ARMA equation in that it models the unobserved output disturbance with moving average as well as autoregressive parameters. It turns out that both $A(q^{-1})$ and $C(q^{-1})$ may be completely recovered from the parameters of this formulation. Hence, one may consider identification of the physiologic mechanisms in Figure 6-2 based on an ARMAX formulation. However, in contrast to the identification of ARMA parameters, the estimation here is not analytic and requires a numerical search.

atrial transmural pressure fluctuations are largely determined by RATP fluctuations, since the diastolic filling time effects on venous return are small (see Figure 2-12) and pulmonary ABP is essentially constant (see Section 2.2.2). Hence, SV fluctuations may be considered to be essentially determined by ABP and RATP fluctuations.

Provided that the fluctuations in these three signals are sufficiently small, we may relate these fluctuations with the following discrete-time, LTI equation:

$$\Delta SV(k) = \sum_{i=1} b(i)\Delta P^{tr}_{\text{“ra”}}(k-i) + \sum_{i=0} d(i)\Delta P_a(k-i), \tag{6.15}$$

where $SV(k)$ may be thought of as a sampled step-wise continuous process whose value is the SV of the current inter-beat interval for a duration of that interval. The impulse responses $b(t)$ and $d(t)$ respectively reflect the heart-lung unit and left ventricular systolic dynamics. Provided that $\overline{P_a} < 180$ mmHg, the static gains of $b(t)$ and $d(t)$ are respectively $\sim C_r^{ed}$ and ~ 0. A measure of the size of $d(t)$ may be obtained from its absolute peak amplitude which is given by C_l^{es}, as the impulse response *immediately* drops to $-C_l^{es}$ at time zero. However, C_l^{es} actually represents an upper bound on the absolute peak amplitude since this value becomes significantly smaller when low sampling rates are considered which is the case here due to smoothing effects.

We may rewrite Equation (6.15) more compactly with delay operator notation (see Section 4.1) as follows:

$$\frac{\Delta SV(k)}{\overline{SV}} = \frac{\overline{P^{tr}_{\text{“ra”}}}}{\overline{SV}} B(q^{-1}) \frac{\Delta P^{tr}_{\text{“ra”}}(k)}{\overline{P^{tr}_{\text{“ra”}}}} + \frac{\overline{P_a}}{\overline{SV}} D(q^{-1}) \frac{\Delta P_a(k)}{\overline{P_a}}, \tag{6.16}$$

where we have also normalized the signals by their mean values and scaled the transfer function operators to offset the normalization. Importantly, the static gain relating relative fluctuations in RATP to relative fluctuations in SV is normalized to one. Assuming that $B(q^{-1})$ is invertible, we may solve this equation for the relative fluc-

tuations in RATP as follows:

$$\frac{\Delta P^{tr}_{\text{“ra”}}(k)}{\overline{P^{tr}_{\text{“ra”}}}} = \frac{\overline{SV}}{\overline{P^{tr}_{\text{“ra”}}}} \frac{1}{B(q^{-1})} \frac{\Delta SV(k)}{\overline{SV}} - \frac{\overline{P_a}}{\overline{P^{tr}_{\text{“ra”}}}} \frac{D(q^{-1})}{B(q^{-1})} \frac{\Delta P_a(k)}{\overline{P_a}}. \tag{6.17}$$

Since the absolute peak amplitude of $d(t) << 1$ for low sampling rates (see Table 3.1) and the standard deviation of the relative fluctuations in SV and ABP are about the same, we neglect the last term of this equation arriving at the following LTI equation which suggests that the relative fluctuations in SV are indicative of the relative fluctuations in RATP:

$$\frac{\Delta P^{tr}_{\text{“ra”}}(k)}{\overline{P^{tr}_{\text{“ra”}}}} \approx \frac{\overline{SV}}{\overline{P^{tr}_{\text{“ra”}}}} \frac{1}{B(q^{-1})} \frac{\Delta SV(k)}{\overline{SV}}. \tag{6.18}$$

We note that the transfer function operator relating the relative fluctuations in this equation is noncausal with a static gain of one.

6.2.3 Direct Identification Method

We are now ready to present the details of two methods for TPR baroreflex identification which are based on the two identification strategies adapted to utilize SV fluctuations in lieu of RATP fluctuations. We first describe, in this section, the method based on the adapted direct identification strategy which we will henceforth refer to as the direct identification method. Figure 6-4 illustrates the model upon which the method is based. The model includes two physiologic coupling mechanisms, Ar TPR BAROREFLEX and SV→TPR, and a perturbing noise source N_{TPR}. SV→TPR reflects the transfer properties relating SV fluctuations to TPR fluctuations which encompass two distinct physiologic coupling mechanisms, INVERSE HEART-LUNG UNIT and CP TPR BAROREFLEX, according to the block diagram in Figure 6-5 derived from the substitution of Equation (6.18) into Equation (6.9). INVERSE HEART-LUNG UNIT specifically reflects the transfer properties relating SV fluctuations to RATP fluctuations which encompass what may be thought of as the inverse

left ventricular, pulmonary, and right ventricular dynamics. Although the dynamics of SV→TPR do not isolate CP TPR BAROREFLEX, the static gain of SV→TPR is equivalent to that of CP TPR BAROREFLEX provided that relative fluctuations in the input and output signals with respect to their mean values are being considered. For a description of the remaining physiologic mechanisms of the model in Figure 6-4, see Section 6.2.1.

Figure 6-4 Direct identification model depicting the feedback mechanisms responsible for the couplings between the fluctuations in ABP, SV, and $\widehat{\text{TPR}}$.

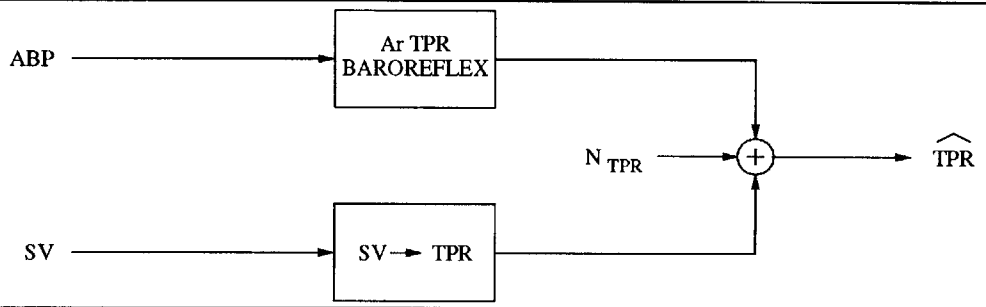

Identification of the transfer properties of the two coupling mechanisms and the power spectrum of the perturbing noise source in Figure 6-4 is performed similarly to the first stage of the previously developed cardiovascular system identification method (see Section 5.1). In particular, the model in Figure 6-4 is mathematically represented by the following linear, dual-input ARMA difference equation:

$$\widehat{TPR}(t) = \sum_{i=1}^{p} d_i \widehat{TPR}(t-i) \sum_{i=1}^{q} e_i ABP(t-i) + \sum_{i=0}^{r} f_i SV(t-i) + W_{TPR}(t), \quad (6.19)$$

where W_{TPR} is the residual error term. The AR and MA parameters completely specify the impulse responses characterizing the two coupling mechanisms (see Section 4.1) and are estimated with the ARMA parameter reduction algorithm (maximal model: p=5, q=5, r=5; see Section 4.3.2). From Equation (4.2), the perturbing noise source is completely characterized by the residual error term and the AR parameters and may be computed as follows:

$$N_{TPR}(t) = \sum_{i=1}^{p} d_i N_{TPR}(t-i) + W_{TPR}(t). \quad (6.20)$$

The power spectrum of the perturbing noise source may be determined according to Equation (4.28). The analysis here utilizes six minute segments of zero-mean ABP, SV, and $\widehat{\text{TPR}}$ normalized by their mean values and sampled at 0.5 Hz. This sampling frequency is chosen based on the bandwidths of the arterial and cardiopulmonary TPR baroreflexes of the forward model (see Figure 3-3). The three signals utilized for identification here are obtained from continuous records of CO and ABP signals at a nonuniform sampling frequency (mean of ~200 Hz; see Section 3.2.1) for forward model data and a uniform 100 Hz sampling frequency for experimental human data as follows.

Figure 6-5 Block diagram of SV→TPR indicating the distinct physiologic mechanisms that it encompasses and their interconnection.

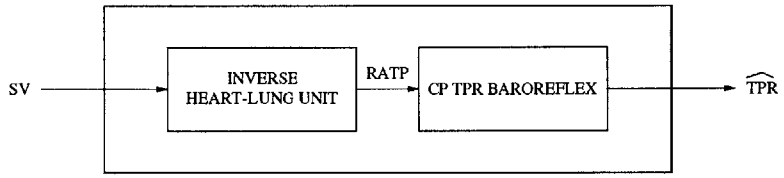

The method that we consider for determining $\widehat{\text{TPR}}$ from CO and ABP signals is based on the simplified systemic circulation model of Figure 6-3. By integrating Equation (6.1), the governing differential equation of this model, over intervals ($t_1 \leq t < t_2$) in which $R_a(t)$ varies little, we may obtain $R_a(t)$ as a function of $P_a(t)$, $\dot{q}_l(t)$, and C_a as follows:

$$R_a(t) = \frac{\frac{1}{t_2-t_1}\int_{t_1}^{t_2} P_a(\tau)d\tau}{\frac{1}{t_2-t_1}\int_{t_1}^{t_2} \dot{q}_l(\tau)d\tau - \frac{C_a}{t_2-t_1}(P_a(t_2) - P_a(t_1))} \quad t_1 \leq t < t_2. \tag{6.21}$$

Note that the numerator of this equation represents the average ABP over the integration interval, while the denominator represents the average flow rate through $R_a(t)$ – the difference in average left ventricular flow rate and the average flow rate through C_a – over the integration interval. Since C_a is assumed to be unknown, $R_a(t)$ may not be accurately determined for arbitrary integration intervals. However, by choosing the integration interval such that the average flow rate through C_a is small,

it may be possible to recover adequately $R_a(t)$ through the following equation:

$$R_a(t) \approx \frac{\frac{1}{t_2-t_1}\int_{t_1}^{t_2} P_a(\tau)d\tau}{\frac{1}{t_2-t_1}\int_{t_1}^{t_2} \dot{q}_l(\tau)d\tau} \quad t_1 \leq t < t_2. \tag{6.22}$$

This may be achieved by choosing the integration interval such that $t_2 - t_1 >> C_a$[4]. Since the bandwidth of $R_a(t)$ is small with respect to the bandwidth of the systemic circulation, we expect that it is possible to choose integration intervals in this manner in which $R_a(t)$ varies little.

Choosing the specific integration interval is a trade-off between keeping the average flow rate through C_a small (large integration interval) and recovering relatively higher frequency information in $R_a(t)$ (small integration interval). For approximately fixed integration intervals, we may attenuate the average flow rate through C_a by specifically considering integration over an integer number of cardiac cycles. In this way, $P_a(t_1)$ is more likely to be near $P_a(t_2)$ in Equation (6.21). In contrast, consider the average flow rate through C_a for this approximately fixed interval if $P_a(t_1)$ happens to be the systolic pressure of a cardiac cycle and $P_a(t_2)$ happens to be the diastolic pressure of another cardiac cycle. Hence, our specific procedure for implementation is as follows. We first estimate a value for TPR for each cardiac cycle by performing the integration in Equation (6.22) (numerical trapezoidal integration) over the interval which includes the five previous and five subsequent cardiac cycles[5].

[4]A second method could be based on choosing the integration interval such that $P_a(t_1) = P_a(t_2)$ which would precisely zero out the average flow rate through C_a [6]. However, based on a forward model analysis, we have found this method to perform significantly better than the first method only when the ABP and CO signals are obtained at the same site in the arterial system. That is, the second method would not improve the estimation of TPR fluctuations when flow rate and ABP are respectively made available from the left ventricle and the finger as in Section 6.5. Furthermore, in practice, we expect the second method to be less robust to measurement noise as compared to the first method. Based on these considerations, we do not consider the second method here.

[5]In the nominal forward model, this integration interval is on average ~9 s, while C_a is 1.6 ml/mmHg.

We then form a step-wise continuous process whose value corresponds to the estimated TPR value of the current cardiac cycle for the time period of that cycle (see formation of HR in Figure 5-2). We finally sample the step-wise continuous process to 0.5 Hz with an anti-aliasing filter whose impulse response is a unit-area boxcar of 4 s duration arriving at the $\widehat{\text{TPR}}$ utilized for identification. The ABP and SV signals that are utilized for identification are similarly processed. In particular, the signals are determined for each cardiac cycle by respectively averaging and integrating the finely sampled ABP and CO signals over the five previous and five subsequent cardiac cycles. Then step-wise continuous processes are analogously formed and sampled to 0.5 Hz.

6.2.4 Indirect Identification Method

We now describe the details of the method based on the similarly adapted indirect identification strategy which we will henceforth refer to as the indirect identification method. Figure 6-6 illustrates the model upon which the method is based. The model includes two physiologic mechanisms, CO→ABP and SV→ABP, and a perturbing noise source N'_{ABP}. SV→ABP reflects the transfer properties relating SV fluctuations to ABP fluctuations which encompass four physiologic coupling mechanisms, INVERSE HEART-LUNG UNIT, SYSTEMIC ARTERIAL TREE, Ar TPR BAROREFLEX, and CP TPR BAROREFLEX, according to the block diagram in Figure 6-7a derived from the substitution of Equation (6.18) into Equation (6.10). SYSTEMIC ARTERIAL TREE specifically reflects the transfer properties coupling CO fluctuations to ABP fluctuations as well as TPR fluctuations to ABP fluctuations. The dynamics of SV→ABP do not isolate RATP→ABP; however, provided that relative fluctuations in the input and output signals with respect to their mean values are being considered, the static gain of SV→ABP is equivalent to that of RATP→ABP. Hence, the static gains of the Ar TPR BAROREFLEX and CP TPR

BAROREFLEX may still be recovered from the physiologic coupling mechanisms in Figure 6-6. We also include in Figure 6-7b a block diagram depicting the interconnection of the distinct physiologic mechanisms encompassed by CO→ABP which is based on Equations (6.11). For a description of N'_{ABP}, see Section 6.2.1 as well as Equation (6.10).

Figure 6-6 Indirect identification model relating couplings between fluctuations in CO, SV, and ABP.

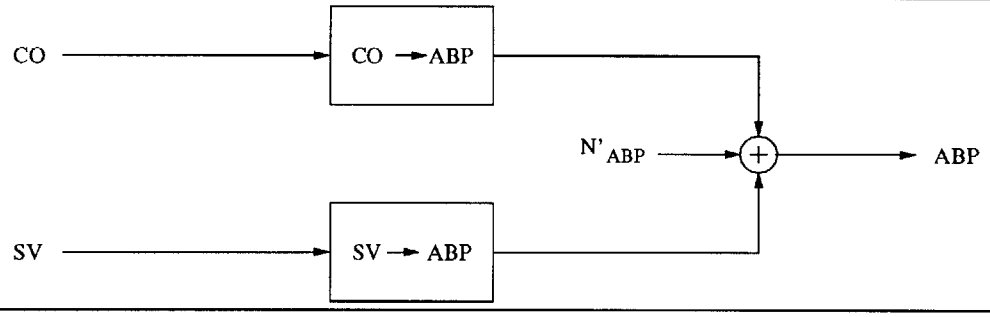

The transfer properties of the two coupling mechanisms and the power spectrum of the perturbing noise source in the model in Figure 6-6 are identified according to the following linear, dual-input ARMA difference equation:

$$ABP(t) = \sum_{i=1}^{s} g_i ABP(t-i) \sum_{i=0}^{u} h_i CO(t-i) + \sum_{i=0}^{v} j_i SV(t-i) + W''_{ABP}(t) \quad (6.23)$$

where W''_{ABP} is the residual error term. Parameter estimation and signal processing here are performed similarly to the direct identification method including the choice of maximal model order (see Section 6.2.3).

6.3 Actual Identification Results

In order to evaluate the direct and indirect identification methods against the forward model, we must first establish their gold standard results in a manner independent of system identification. We first consider the establishment of the actual direct and indirect identification impulse responses (Ar TPR BAROREFLEX, SV→TPR,

Figure 6-7 Block diagram of (a) SV→ABP and (b) CO→ABP indicating the interconnections of the distinct physiologic mechanisms that they encompass.

(a)

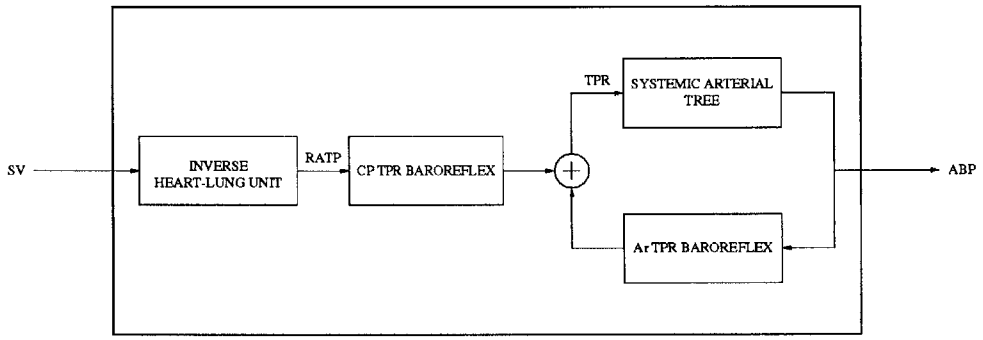

(b)

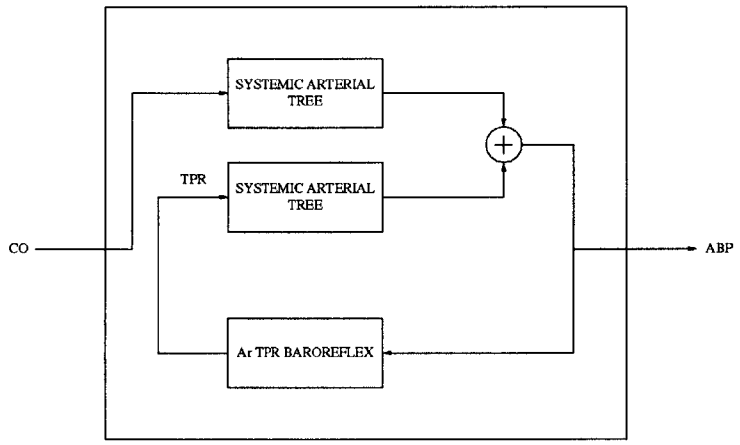

CO→ABP, and SV→ABP). To this end, we define the impulse responses characterizing each of the four sub-blocks in the block diagrams of Figures 6-5 and 6-7 for the forward model. These four sub-blocks include: Ar TPR BAROREFLEX, CP TPR BAROREFLEX, SYSTEMIC ARTERIAL TREE, and INVERSE HEART-LUNG UNIT. We may then establish the actual SV→TPR, CO→ABP, and SV→ABP impulse responses by simply interconnecting the four defined impulse responses according to the block diagrams. In the following paragraph, we describe the specific procedures (see Section 5.2.1) for establishing the actual impulse responses charac-

terizing each of the sub-blocks.

The actual Ar TPR BAROREFLEX and CP TPR BAROREFLEX impulse responses are established analogously to the actual HR BAROREFLEX impulse response as described in Section 5.2.1. However, the actual impulse responses here are decimated to 0.5 Hz from 16 Hz and scaled for the consideration of relative fluctuations (see Equation (6.9)). The actual SYSTEMIC ARTERIAL TREE impulse response is defined essentially by virtue of forward model implementation. In particular, the continuous-time version of this impulse response is defined in Equation (6.4). This continuous-time impulse response is simply sampled to 90 Hz according to Equation (6.6) and then decimated to 0.5 Hz to arrive at the actual SYSTEMIC ARTERIAL TREE impulse response. The actual INVERSE HEART-LUNG UNIT impulse response is established based on Equation (6.17). We first determine the actual impulse response $b(t)$ (reflected by the transfer function operator $B(q^{-1})$ in this equation) from the uncontrolled, unperturbed heart-lung model in Figure 2-10. This model permits the fluctuations in ABP to be set to zero through the voltage source P_a as well as the application of an approximate impulse or step of RATP through the voltage source P_v. The voltage source P_a is simply set to the mean ABP of the identification data, while the voltage source P_v is initially set to a value which achieves the mean RATP of the identification data. The value of P_v is then stepped up to a value which achieves the mean RATP plus one standard deviation as determined from the identification data. The appropriate values of P_v are determined from the bisection method as described in Section 2.4.3. We measure the response of $\dot{q}_l(t)$ to this step input and integrate this signal over each cardiac cycle in order to obtain an SV beat sequence which is converted into a uniformly sampled time series at 0.5 Hz through the formation of a step-wise continuous process. The zero-mean, uniformly sampled signal is then normalized by the standard deviation of RATP as determined from the identification data and differentiated so as to arrive at the desired $b(t)$. We

next invert this impulse response and scale it according to Equation (6.18) arriving at the actual INVERSE HEART-LUNG UNIT impulse response.

Figure 6-8 Actual direct identification results characterizing the nominal forward model. These results are determined independently of system identification.

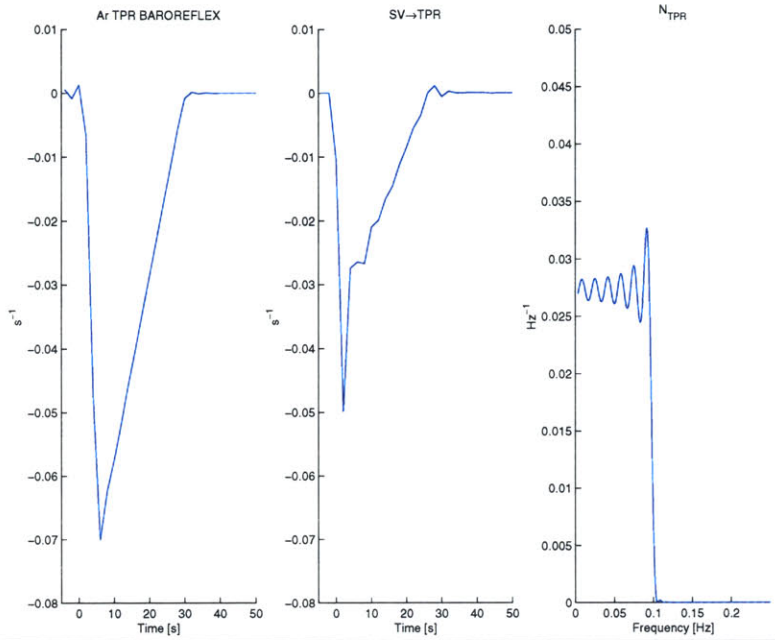

We now consider the establishment of the actual direct and indirect identification power spectra of the perturbing noise sources (N_{TPR} and N'_{ABP}). The actual N_{TPR} perturbing noise source of the forward model is simply $n_{R_a}(t)$. The forward model generates $n_{R_a}(t)$ by passing a Gaussian white noise process of zero-mean and variance σ^2 through the LTI filter in Equation (3.10). Hence, the actual power spectrum is given by the product of the magnitude squared frequency response of this filter and σ^2 normalized for relative fluctuations (see Equation (6.9)). The actual N'_{ABP} perturbing noise source is defined according to Equation (6.10) as the actual N_{TPR} perturbing noise source passed through the actual CO→ABP impulse response. Hence, the actual power spectrum of N'_{ABP} may be determined simply from the product of the magnitude squared frequency response of the actual CO→ABP impulse response and the actual power spectrum of N_{TPR}. Figures 6-8 and 6-9 illustrate the resulting actual direct and indirect identification results for the nominal forward model.

Figure 6-9 Actual indirect identification results characterizing the nominal forward model. These results are determined independently of system identification.

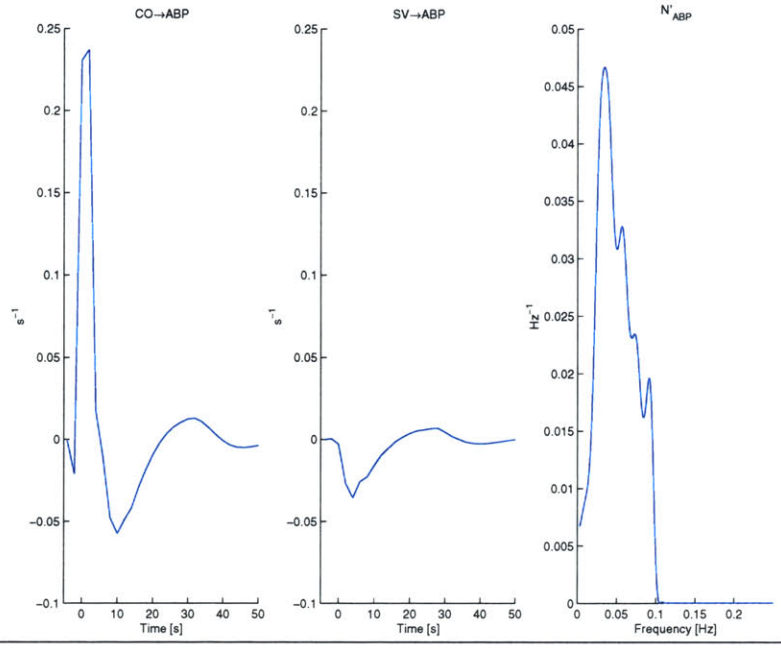

6.4 Forward Model Analysis

With the gold standard results established, we may now analyze the performance of the direct and indirect identification methods against forward model generated data. However, before we proceed with this analysis, we first reconsider the validity of two properties of the nominal forward model which play a critical role in the performance of the identification methods.

The first property is the signal-to-noise ratio (SNR) of TPR fluctuations which is defined to be the ratio of the standard deviation of the actual TPR fluctuations due to the baroreflexes to the standard deviation of the actual TPR fluctuations due to the unobserved TPR disturbance. It turns out that the value of this property is only $\sim$0.25 for the nominal forward model. That is, for every part of TPR fluctuations due to the baroreflexes, there are about four parts due to the unobserved TPR disturbance. This SNR value is sufficiently small such that reliable identification is not possible even when the fluctuations in ABP, RATP, and the *actual* TPR signals

from the nominal forward model are considered for analysis. As we discussed in Section 3.3.2, the standard deviation of the TPR disturbance is chosen such that the model spectra resembles spectra of experimental human data, particularly at the low frequency range (0.04-0.15 Hz). However, it is possible to set the standard deviation of this disturbance, and consequently the SNR of TPR fluctuations, to arbitrary values, while maintaining reasonable spectra, through the introduction of a disturbance to $Q_v^0(t)$ which may reflect systemic venous dead volume fluctuations due to, for example, fast acting hormonal systems. In the nominal forward model, this disturbance may, for example, induce ABP fluctuations, and consequently heart rate fluctuations, through SV fluctuations. This is consistent with experimental findings which have hypothesized TPR fluctuations, but have not precluded SV fluctuations, in the genesis of low frequency ABP and heart rate fluctuations (see Section 3.1). It is also possible to alter the SNR and maintain reasonable spectra by adjusting other parameters of the forward model including, for example, the static gains of the arterial and cardiopulmonary TPR baroreflexes. Although experimental data do exist suggesting, at least to within some range, the values of these static gains [23], there are no experimental data indicating the size of the unobserved TPR disturbance and hence the SNR of TPR fluctuations.

The second property is measurement noise which is neglected in the nominal forward model. This seems more reasonable for the analysis of the cardiovascular system identification method in Chapter 5, because the signals which the method analyzes are obtained easily and reliably in practice. However, the direct and indirect identification methods require the beat by beat measurement of CO which is somewhat difficult to obtain in practice. Consequently, measurement noise is an important factor here.

Based on these considerations, we assess the performance of the direct and indirect identification methods against data generated from the forward model with the

following adjustments. We arbitrarily set the SNR of TPR fluctuations to a value of ~ 5[6] by decreasing the nominal standard deviation of the TPR disturbance. In order to maintain realistic spectra, we introduce a disturbance to $Q_v^0(t)$ whose power spectrum is the same as that of the TPR disturbance except with a standard deviation of 3.125 ml. Finally, we add zero-mean, white noise to the CO and ABP beat sequences determined by averaging the $\dot{q}_l(t)$ and $P_a(t)$ signals generated by the forward model over each cardiac cycle. The standard deviation of the additive CO noise is set to 25% of the standard deviation of the CO beat sequence, while the standard deviation of the additive ABP noise is set to 12.5% of the standard deviation of the ABP beat sequence. We also add zero-mean, white noise to the effective RR interval sequence with a standard deviation of 12.5% of the standard deviation of the effective RR intervals.

Figures 6-10 and 6-11 respectively illustrate the direct and indirect identification estimates along with their corresponding gold standards from the forward model generated data. We present the coupling mechanisms in terms of their step responses in order to indicate the performance of the estimates in terms of static gains (asymptotic values of the step responses) as well.

Figure 6-10 illustrates striking deviations between the direct identification estimates and their respective gold standards. In particular, the estimated dynamics are much faster than the gold standard dynamics and the estimated Ar TPR BAROREFLEX step response indicates a positive feedback arterial TPR baroreflex. That is, TPR increases in response to an increase in ABP. These deviations prompt us to reconsider the direct identification method. The intent of this method is to analyze the

[6]It turns out that an SNR value $>\sim 3$ is sufficient for reliable identification when ABP, RATP, and the actual TPR of the forward model are considered for analysis. The validity of the SNR value of ~ 5 may be evaluated, at least to some extent, by applying the identification methods to experimental data (see Section 6.5) and examining the standard deviation of the resulting estimates which are indicative of the SNR.

Figure 6-10 Direct identification estimates (red denotes mean and dashed red denotes standard deviation) with gold standard (blue). The coupling mechanisms are shown in terms of their step responses. The estimates are determined from 20 different realizations of forward model generated data.

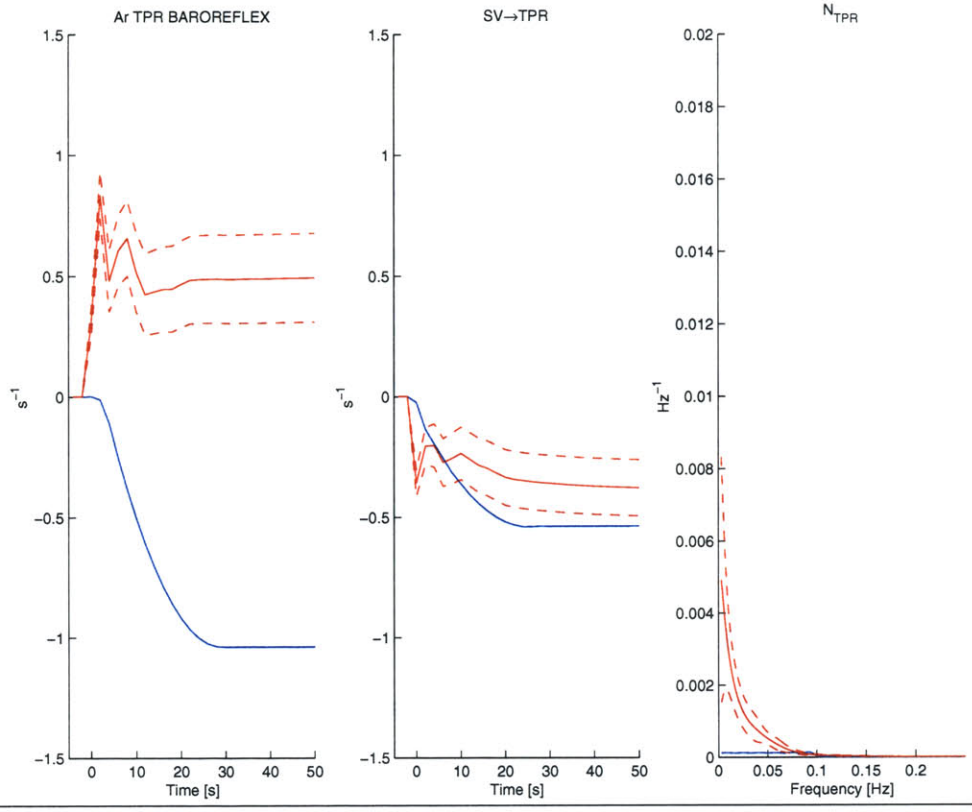

relative fluctuations in ABP, SV, and $\widehat{\text{TPR}}$ in order to characterize the physiologic mechanisms responsible for coupling these signals. The relative fluctuations in these signals are related in the forward model according to the following relationship:

$$\frac{\Delta\widehat{R_a}(k)}{\overline{\widehat{R_a}}} = \frac{\overline{P_a}}{\overline{\widehat{R_a}}} A(q^{-1}) \frac{\Delta P_a(k)}{\overline{P_a}} + \frac{\overline{SV}}{\overline{\widehat{R_a}}} \frac{C(q^{-1})}{B(q^{-1})} \frac{\Delta SV(k)}{\overline{SV}} + \frac{n_{R_a}(k)}{\overline{\widehat{R_a}}}, \tag{6.24}$$

which is derived from the substitution of Equation (6.18) into Equation (6.9), However, from Equation (6.22), the fluctuations in TPR are essentially estimated according to the following equation:

$$\widehat{R_a}(k) = \frac{P_a(k)}{SV(k) \cdot F(k)}. \tag{6.25}$$

By removing mean values from this equation, normalizing it by $\overline{\widehat{R_a}}$, and neglecting

second order terms, the following relationship results:

$$\frac{\Delta\widehat{R_a}(k)}{\overline{\widehat{R_a}}} = \frac{\Delta P_a(k)}{\overline{P_a}} - \frac{\Delta SV(k)}{\overline{SV}} - \frac{\Delta F(k)}{\overline{F}}. \tag{6.26}$$

Hence, the method for the estimation of TPR fluctuations imposes a nonphysiologic relationship between the relative fluctuations in ABP, SV, and $\widehat{\text{TPR}}$. That is, this equation would erroneously suggest that the Ar TPR BAROREFLEX and SV→TPR step responses are step functions scaled by one and minus one, respectively.

Hence, the direct identification problem essentially has two solutions as indicated by Equations (6.24) and (6.26). Therefore, one may assume that this problem is ill-conditioned. However, this is not the case here due to the inclusion of measurement noise which tends to favor the solution of Equation (6.26). In fact, as the size of the measurement noise is increased, the estimated Ar TPR BAROREFLEX and SV→TPR asymptotic step response values respectively tend towards one and minus one. This tendency is less marked for SV→TPR perhaps due to the fact that relative fluctuations in SV deviate from the relative fluctuations in CO by the relative fluctuations in heart rate. On the other hand, when measurement noise is excluded (which is not a realistic scenario as discussed above), reliable estimation of the static gains of Ar TPR BAROREFLEX and SV→TPR is achieved. This indicates that $\widehat{\text{TPR}}$ is more reliable at very low frequencies which is as expected[7] (see Section 6.2.3). However, if we increase the maximal model order of the ARMA parameter reduction algorithm when there is no measurement noise, the direct identification problem becomes ill-conditioned. We explain this different result as follows. Equation (6.26) is not quite an adequate second solution here due to the heart rate fluctuations which are not considered by the direct identification method. However, when the maximal model order is large, there are enough past values of ABP and SV to account for these heart rate fluctuations which renders Equation (6.26) to be an adequate solution. Although

[7]The relative fluctuations in $\widehat{\text{TPR}}$ deviate by $56 \pm 4\%$ from the relative fluctuations in the actual TPR generated by the nominal forward model.

the asymptotic value of the estimated SV→TPR step response seems to be fairly reliable even in the presence of measurement noise, consider the consequences if the very low frequency heart rate fluctuations were relatively small as might be the case if the data were collected while the subject was in the supine posture.

Figure 6-11 Indirect identification estimates (red denotes mean and dashed red denotes standard deviation) with gold standard (blue). The coupling mechanisms are shown in terms of their step responses. The estimates are determined from 20 different realizations of forward model generated data.

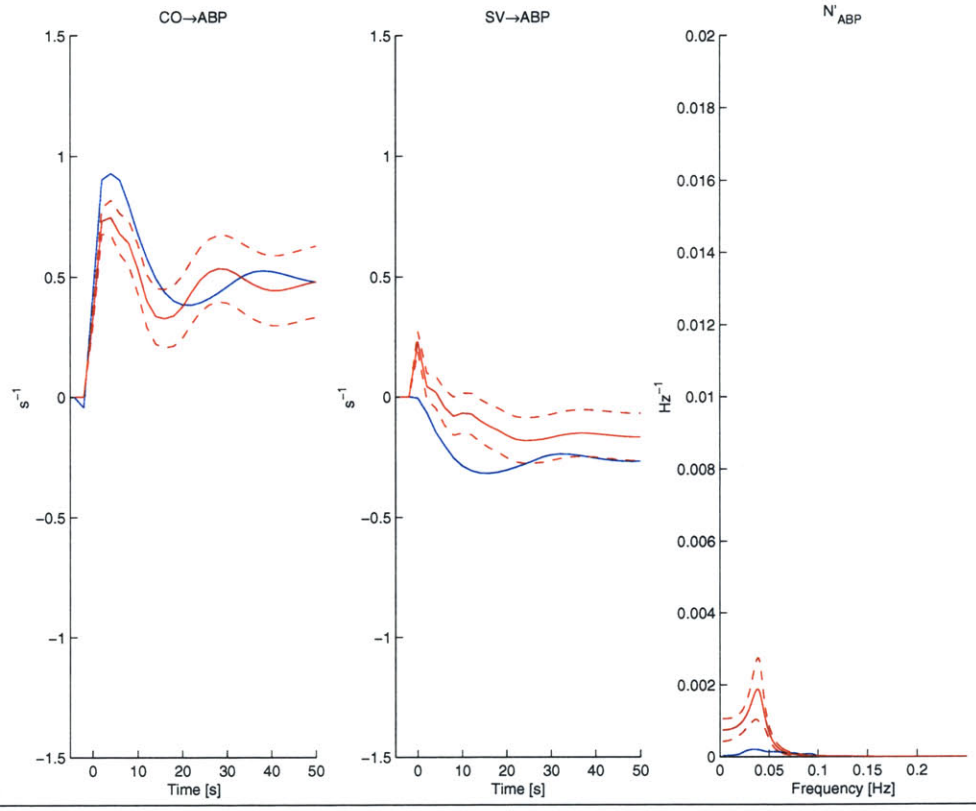

On the other hand, Figure 6-11 demonstrates that reliable indirect identification is generally achieved. We provide in Table 6.1 the corresponding NMSE results for the indirect identification estimates. The table includes the NMSE for the asymptotic step response value (static gain) estimates as well which is defined as follows. Again let us refer to the impulse response estimate as vector x with mean vector $\hat{x}$ and covariance matrix Λ_x and its corresponding gold standard as vector x_0. Then, the static gain for the estimate and gold standard are respectively given by $y = T_s \sum_i x_i$

and $y_0 = T_s \sum_i x_{0,i}$, where T_s is the sampling period, and the NMSE is defined here as follows:

$$\begin{aligned} NMSE(y, y_0) &= \sqrt{\frac{E(y - y_0)^2}{E y_0^2}} \cdot 100\% \\ &= \sqrt{\frac{T_s^2 sum(\Lambda_x)}{y_0^2} + \frac{(\hat{y} - y_0)^2}{y_0^2}} \cdot 100\%, \end{aligned} \tag{6.27}$$

where $E(\cdot)$ is again the expectation operator and $sum(\cdot)$ is defined to be the operator which sums the elements of its matrix argument.

Indirect Identification Results	Impulse Response/Power Spectrum NMSE [%]	Static Gain NMSE [%]
CO→ABP	47±7	30±10
SV→ABP	238±44	47±18
N'_{ABP}	651±222	—

Table 6.1: NMSE (mean±standard deviation) results of the indirect identification estimates in Figure 6-11.

The results of the figure and table indicate that the estimated SV→ABP step response, and perhaps as a consequence N'_{ABP}, do not resemble adequately their respective gold standard in terms of dynamics. We hypothesize that this is due to the no delay property of the closed-loop relationship between SV fluctuations and ABP fluctuations. That is, SV fluctuations influence ABP fluctuations through the compliance properties of the aorta, while ABP fluctuations *simultaneously* influence SV fluctuations through afterload effects. As discussed in Section 4.2.4, reliable identification is not possible when the data are obtained in closed-loop with no delay in both the feedforward and feedback pathways. However, importantly, this simultaneous interaction between ABP and SV fluctuations is an immediate, high frequency effect (see Figure 6-11). Consequently, the static gain of the estimate is relatively

unaffected. We also note that some of the discrepancy between the SV→ABP estimate and its gold standard may be attributed to the fact that SV fluctuations are not perfectly determined by RATP fluctuations (see Section 6.2.2). This may explain, at least to some extent, why the downward deflection of the estimated step response is somewhat underestimated. We also note that the low frequency relative fluctuations considered by the indirect identification method are sufficiently small such that the results here are robust against all the nonlinear arterial compartments of Figure 2-14.

6.5 Experimental Data Analysis

We now present the application of the direct and indirect identification methods to experimental data. The data analyzed here specifically include approximately five minute segments of noninvasively measured CO (Doppler ultrasound technique) and ABP (Finapres) signals obtained from ten healthy human subjects in the supine posture during random-interval breathing.

Figure 6-12 illustrates the resulting group average direct identification estimates. Importantly, the estimates here are similar to the direct identification estimates obtained from data generated by the forward model (see Figure 6-10). Without the forward model analysis of the previous section, one might have been tempted to interpret the estimate of the Ar TPR BAROREFLEX step response as a positive feedback mechanism perhaps representing the cumulative effects of the autoregulation of local vascular beds. However, because of the forward model analysis, we consider this estimate, along with the estimate of the SV→TPR step response, to be artifactual as a consequence of the method for estimating TPR fluctuations. Based on the experimental results here together with the forward model-based results in the previous section, we conclude that quantification of the arterial and cardiopulmonary TPR baroreflexes is not reliable with the direct identification method as described in

Section 6.2.3. However, if the relative fluctuations in TPR could be estimated with a different approach (see Section 7.2), then reliable estimation may be possible.

Figure 6-12 Direct identification estimates (red denotes mean and dashed red denotes standard deviation) from experimental human data. The coupling mechanisms are shown in terms of their step responses. The estimates are determined from ten healthy subjects.

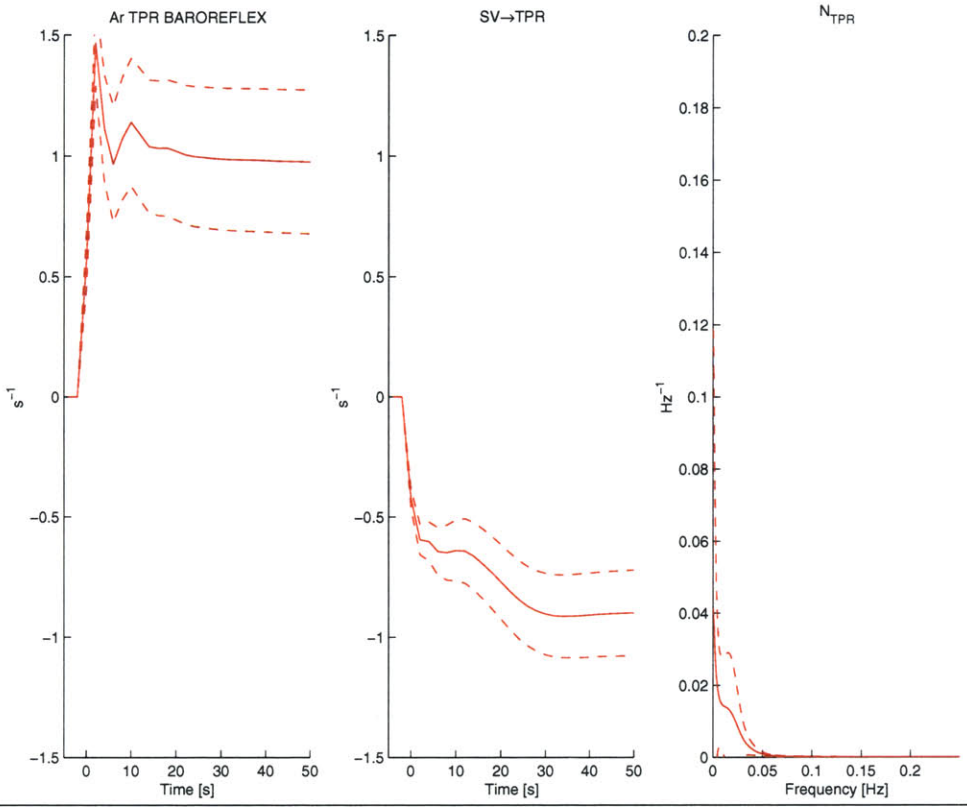

Figure 6-13 illustrates the resulting group average indirect identification estimates which are also similar to the corresponding estimates obtained from data generated by the forward model (see Figure 6-11). The static gain values of the Ar TPR BAROREFLEX and CP TPR BAROREFLEX, as determined from the indirect identification estimates (see Section 6.2.1) are respectively -1.79 and -1.56. These values indicate that a 10% increase in ABP would result in a steady-state decrease in TPR of 17.9% due to the arterial TPR baroreflex, while a 10% increase in RATP would result in a steady-state decrease in TPR of 15.6% due to the cardiopulmonary TPR baroreflex. In the forward model, the static gains of the Ar TPR BAROREFLEX and CP TPR

BAROREFLEX are set to -1.09 and -0.56, respectively. The duration of time for the estimated CO→ABP step response to reach its asymptotic value is ∼30 s, while this time duration is ∼40 s for the forward model. However, we do not hold much stock in the estimated dynamics of the SV→ABP step response which initially appear to be faster than expected somewhat like the corresponding estimate from forward model generated data. Hence, the estimates derived from the application of the indirect identification method to experimental human data compare favorably to the dynamics of the forward model which are based on independent experimental data. Because the indirect identification method is generally reliable with respect to the forward model generated data as well, we conclude that this method may provide a relatively convenient tool for obtaining quantitative information pertaining to the arterial and cardiopulmonary TPR baroreflexes in humans. Therefore, we believe that it would be worthwhile to explore the experimental validation of the indirect identification method (see Chapter 8).

Figure 6-13 Indirect identification estimates (red denotes mean and dashed red denotes standard deviation) from experimental human data. The coupling mechanisms are shown in terms of their step responses. The estimates are determined from ten healthy subjects.

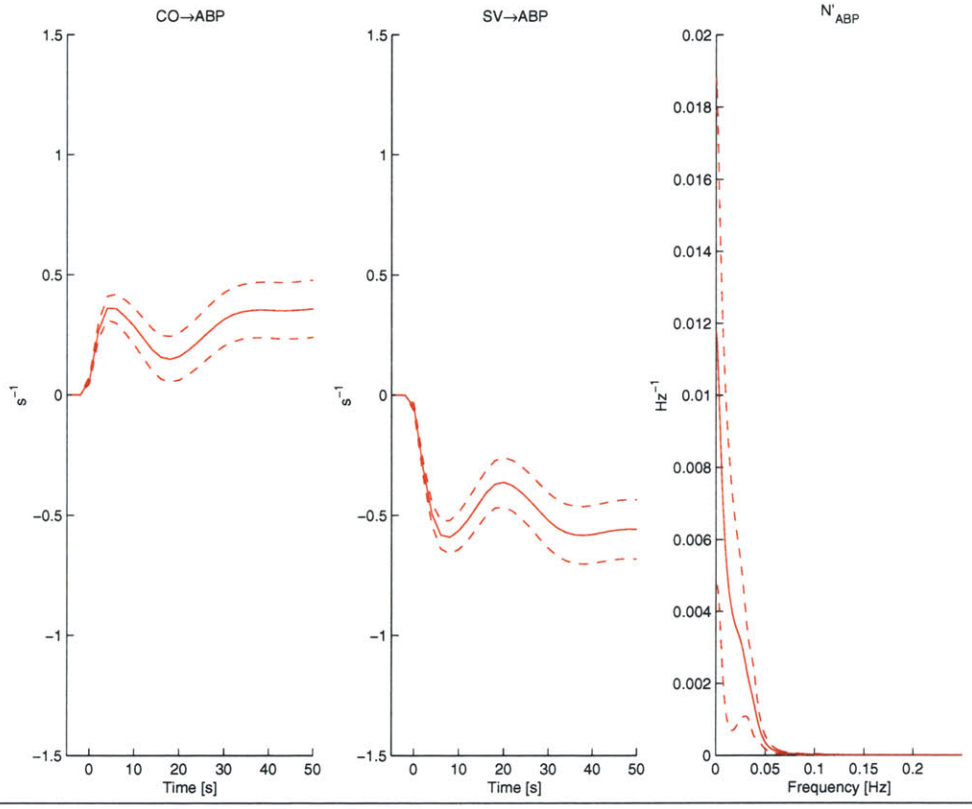

Chapter 7

TPR Estimation From ABP Waveform

In Chapter 6, we developed a promising total peripheral resistance (TPR) baroreflex identification method that requires beat by beat measurements of left ventricular flow rate (cardiac output, CO) and arterial blood pressure (ABP) which may be obtained noninvasively in humans via Doppler ultrasound and Finapres techniques, respectively. With these measurements, steady-state changes in TPR may also be conveniently monitored through the ratio of mean ABP to mean CO. However, as discussed in Section 1.2, the Doppler ultrasound technique requires an expert operator and may not always be available. On the other hand, reliable, beat by beat measurement of CO is not necessary for tracking steady-state changes in TPR. In fact, TPR is usually monitored clinically with a CO measurement obtained from thermodilution which essentially involves the injection of cold saline in the right atrium and the measurement of temperature downstream in the pulmonary artery [10]. CO may then be calculated by applying the conservation of mass principle. However, this technique requires a venous puncture, assumes that the cold saline has been thoroughly mixed with the blood, and is implemented over a relatively short time interval such that

mean CO may not be adequately determined. Due to the difficulties in the measurement of CO, investigators have attempted to monitor TPR from only the ABP waveform by fitting an exponential to the diastolic decay portion of an ABP wavelet (*e.g.*, [12,46]). The time constant estimated from this fit is assumed to represent the dominant time constant of the systemic arterial tree (τ_D) – the product of mean TPR and the lumped arterial compliance – which would permit the monitoring of TPR, provided that arterial compliance is relatively static. However, the diastolic decay portion of the peripheral ABP wavelet is significantly corrupted by pulse reflections (see Section 2.5.2) such that an exponential decay is usually impossible to discern visually. Although the diastolic decay portions of the central ABP wavelet are relatively free of pulse reflections, they are also somewhat corrupted due to the dicrotic notch denoting aortic valve closure. Consequently, an exponential fit here may only be possible for sufficiently low heart rates such that the dynamics responsible for the dicrotic notch have vanished. Furthermore, central ABP may only be obtained by invasive measurement techniques.

In this chapter, we analyze a novel method based on system identification which may permit the reliable estimation of τ_D from an ABP waveform obtained at any point in the arterial system despite the presence of pulse reflections (or the dicrotic notch). We begin by describing the method at the conceptual level and then present some of the details of data analysis (Section 7.1). We next evaluate the performance of the method against data generated from the forward model (Section 7.2) as well as a preliminary set of experimental data (Section 7.3).

7.1 Identification Method

As we have discussed, pulse reflections corrupt the peripheral ABP waveform such that an exponential decay during diastole is usually impossible to discern visually.

However, since pulse reflections largely corrupt the waveform on short time scales within about a cardiac cycle (high frequencies), the waveform on longer time scales (low frequencies) is relatively unscathed thus reflecting only τ_D. Hence, it should be possible to estimate accurately τ_D by analyzing the ABP waveform over long time scales. To this end, we have developed a method which is based on the identification of the CIRCULATORY MECHANICS impulse response (see Section 5.1). Recall that this impulse response represents the ABP wavelet that would result from a *single* ventricular contraction. Hence, the tail end of the diastolic decay of the estimated CIRCULATORY MECHANICS impulse response resembles an exponential from which τ_D may be determined as the faster pulse reflections have vanished.

The CIRCULATORY MECHANICS identification method was originally designed to provide a means to remove the pulsatile component from ABP while preserving ABP variation due to instantaneous lung volume (ILV). We modify the identification method in order to tailor it to the purpose here of estimating τ_D. In particular, we consider a single-input identification problem where the input is the PHR signal[1] (see Section 5.1) adjusted such that the area of each of its impulses is set to the pulse pressure (PP) of the ensuing beat (PHR_{PP}), and the output remains as ABP. This modification improves the fit between PHR_{PP} and ABP which would presumably provide a more accurate estimate of τ_D. It is not necessary to include ILV as an additional identification input here, because its influence on ABP is completely encompassed by PHR_{PP}. Figure 7-1 provides a pictorial representation of the modified identification problem and the subsequent exponential fit. Note that the peak amplitude of the impulse response here, referred to as CIRCULATORY MECHANICS', is approximately equal to one. This is in contrast to the peak amplitude of the CIRCULATORY MECHANICS impulse response estimate determined from the

[1] Although we construct PHR from the ECG (see Figure 5-2), it is possible to derive a PHR signal from the ABP waveform.

original method which is approximately equal to the mean PP (see Figure 5-3).

Figure 7-1 Pictorial representation of identification method for determining τ_D from an ABP waveform obtained at any point in the arterial system. The data illustrated here are generated from the forward model with the third-order systemic arterial compartment of Figure 2-15.

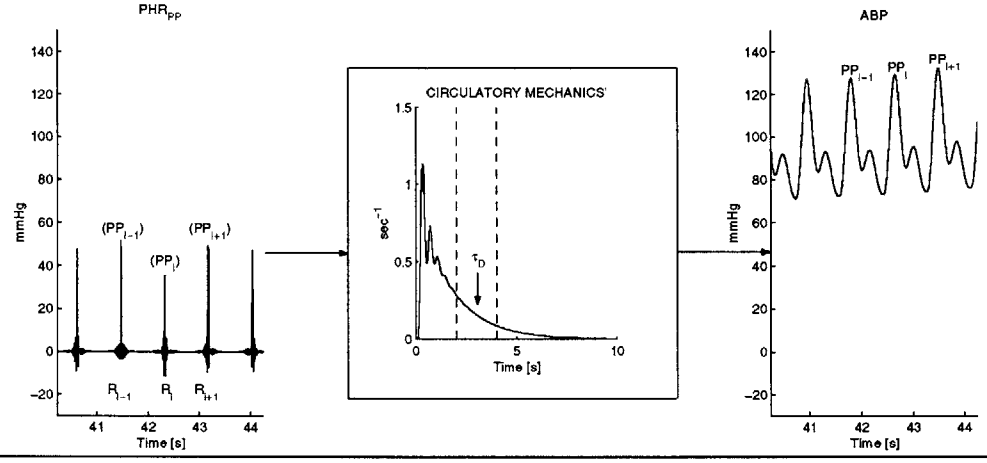

The CIRCULATORY MECHANICS' impulse response may be identified according to the following linear, single-input ARMA difference equation:

$$ABP(t) = \sum_{i=1}^{m} a_i ABP(t-i) + \sum_{i=1}^{n} b_i PHR_{PP}(t-i) + W'''_{ABP}(t) \qquad (7.1)$$

where W'''_{ABP} is the residual error term. The parameters, which completely characterize the impulse response, are estimated from 90 second segments of PHR_{PP} and ABP signals sampled at 90 Hz (see Section 5.1) with the ARMA parameter reduction algorithm of Section 4.3.2[2]. The maximal model is given as follows: m=10 and n=42/$\overline{HR}$, where $\overline{HR}$ is in units of bps. The value of n here is determined empirically based on a forward model analysis. This value indicates that, for higher heart rates, fewer MA parameters are required to characterize reliably the CIRCULATORY MECHANICS' impulse response.

[2]Since the longer time scale information in ABP almost exclusively reflects τ_D, it may be worthwhile to consider prefiltering the signals in order to amplify its energy at the lower frequencies. In theory, this would essentially weight the least squares identification problem such that the fit between the identification input and output at these frequencies would be favored.

We estimate τ_D by fitting an exponential to the identified impulse response over the interval from two to four seconds as depicted in Figure 7-1. We choose to start the interval at two seconds, because the faster pulse reflections are sufficiently attenuated by this time. On the other hand, the diastolic portions of the ABP waveform also include an infinite time constant. That is, if the heart were stopped, ABP would not decay to zero but rather to the mean systemic pressure (see Section 2.4.2). The contribution of this time constant, which is initially small, becomes increasingly significant with time. Consequently, we limit the interval to four seconds. In Appendix B, we describe the details for the determination of the mean and standard deviation of the τ_D estimate.

Before we proceed with the forward model analysis, we consider the identification problem here at the conceptual level for the case in which the heart rate is fixed. In theory, there would be two impulse responses which solve the identification problem in this case. One of the solutions is depicted in Figure 7-1 and is the impulse response that we desire. The other impulse response solution is essentially a single ABP wavelet with two discontinuities, one from zero to about the diastolic pressure at time zero and the other from about the diastolic pressure to zero at the time of end-diastole. Fortunately, the former impulse response is the unique solution when the identification problem is solved with linear least squares estimation. Since this estimation technique can only identify dynamics at frequencies present in the input *and* output data, the high frequency discontinuities of the latter impulse response solution cannot be identified. Hence, linear least squares identification here is a well conditioned problem. We further note that if the means of PHR_{PP} and ABP were removed, in theory, there would be an infinite number of impulse response solutions. However, linear least squares estimation again provides a unique impulse response solution which is approximately a single ABP wavelet minus its diastolic pressure (that is, no discontinuities; see [57,59]). This, of course, is *not* the solution that we

desire.

7.2 Forward Model Analysis

We are now ready to assess the performance of the identification method against ABP waveforms generated by the forward model. We specifically evaluate the method in terms of its ability to estimate τ_{D} as well as steady-state changes in TPR. We also consider a preliminary analysis of the method in terms of its potential to measure changes in TPR on short time scales.

The gold standard value of τ_{D} in the forward model may be simply determined from the product of the average $R_a(t)$ over the segment of analyzed data and C_a. In order to quantify how closely the τ_{D} estimate derived from the identification method matches its gold standard value, we again call upon the NMSE which was first introduced in Section 5.2.2. Let τ_D denote the estimate with mean $\widehat{\tau_D}$ and standard deviation σ_{τ_D}, while $\tau_{D,0}$ represent the corresponding gold standard. Then, the NMSE may be defined here as follows:

$$\begin{aligned} NMSE(\tau_D, \tau_{D,0}) &= \sqrt{\frac{E(\tau_D - \tau_{D,0})^2}{E\tau_{D,0}^2}} \cdot 100\% \\ &= \sqrt{\frac{\sigma_{\tau_D}^2}{\tau_{D,0}^2} + \frac{(\widehat{\tau_D} - \tau_{D,0})^2}{\tau_{D,0}^2}} \cdot 100\%. \end{aligned} \tag{7.2}$$

The NMSE result (mean±standard deviation) as determined from 20 different realizations of the ABP waveform generated from the nominal forward model during random-interval breathing is 4.9±0.5%. The estimate here slightly overestimates its gold standard perhaps due to the small contribution of the infinite time constant in the ABP waveform (see Section 7.1). Although the method performs quite well, the nominal model does not include pulse reflections, the dicrotic notch, or any other system dynamics which emulate such corruptions to the diastolic portions of the ABP waveform. Hence, we heretofore consider the method against the ABP

waveform generated from the forward model with the nominal systemic arterial compartment replaced by the third-order systemic arterial compartment of Figure 2-15. Figure 2-16 demonstrates that the latter compartment emulates the peripheral ABP waveform. The resulting NMSE value (mean±standard deviation), determined again with random-interval breathing for 20 different realizations of the ABP waveform, is 4.3±0.5%. This result demonstrates the potential efficacy of the method in teasing out τ_D from the longer time scale information in the ABP waveform despite the presence of higher frequency dynamics corrupting the diastolic decay of each ABP wavelet.

Although the systemic arterial compliance decreases with increasing ABP and age (see Figures 2-13 and 2-14), it is believed to be essentially constant over a fairly wide range of ABP and on the time scale of hours to days. Hence, the following equality holds to the extent that this belief is true:

$$\frac{TPR_2 - TPR_1}{TPR_1} = \frac{\tau_{D,2} - \tau_{D,1}}{\tau_{D,1}}, \tag{7.3}$$

where TPR_i and $\tau_{D,i}$ denote steady-state values determined from the i^{th} segment of data. This equation indicates that tracking τ_D is equivalent to tracking TPR in terms of steady-state, relative changes. For example, an estimated 10% steady-state increase in τ_D would indicate the same percentage increase in TPR.

We now evaluate the sensitivity of the identification method in detecting steady-state, relative changes in TPR when the equality here holds (constant arterial compliance). We again consider the analysis of the ABP waveform generated from the forward model during random-interval breathing in which the steady-state value of TPR is adjusted by increasing and decreasing the parameter R_a^{sp} (see Table 3.1) by 5% and 10% with respect to its nominal value. Figure 7-2 illustrates the results in terms of the estimated steady-state percentage change in TPR as determined from the τ_D estimate versus the actual steady-state percentage change in TPR. The figure demonstrates that the identification method is quite sensitive, able to detect steady-

state changes in TPR $< 5\%$. Note that the identification method appears to be more accurate in terms of estimating relative changes in TPR than in estimating τ_D. The reason for this is that the overestimation of τ_D due to the presence of the infinite time constant in the ABP waveform is essentially canceled out when considering relative changes (see Equation (7.3)).

Figure 7-2 Sensitivity results (red trace, mean±standard deviation) in terms of estimated versus actual percentage change in steady-state TPR with respect to the nominal values. The results are determined from 20 different realizations of data generated by the forward model with the third-order systemic arterial compartment of Figure 2-15. The blue trace denotes the identity line.

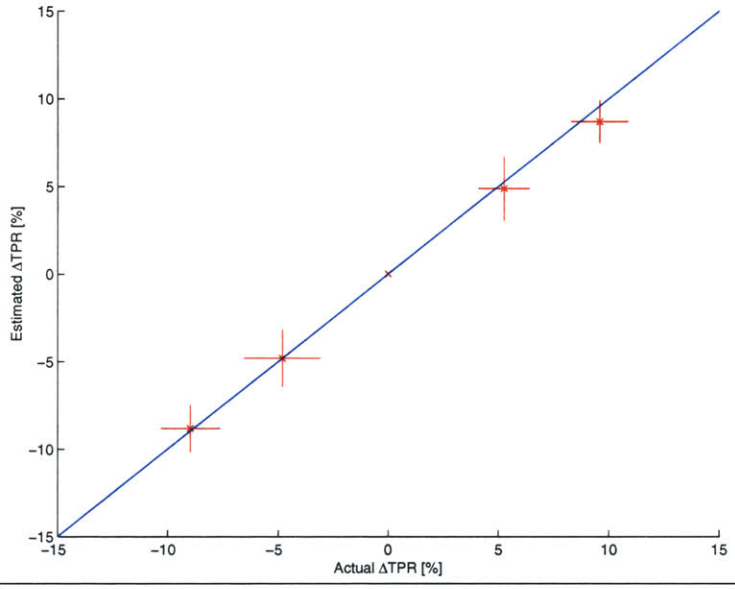

Certainly, the results of Figure 7-2 would be adversely affected if there were a change in the systemic arterial compliance as well. The extent of such a change, which may be due to a multitude of factors (*e.g.*, disease, change in mean ABP, degree of systemic arterial compliance nonlinearity), is highly variable, and its influence on the performance of the identification method in predicting steady-state relative changes in TPR may be best addressed with experimental data (see Section 7.3).

It turns out that, in the forward model, pulsatile variability alone is sufficient for obtaining a good estimate of τ_D provided that the heart rate is not too close to the resonant frequency of the third-order systemic arterial compartment ($\sim$150 bpm). As

a consequence, the τ_D estimate is quite reliable even when only ten second segments of data are considered for analysis. This may signify the importance of the role of the DC component (more precisely, a continuum of frequencies near DC as finite data records are considered) of the ABP waveform in the reliable estimation of τ_D. Since this component is relatively large in terms of energy, least squares identification will accurately estimate the CIRCULATORY MECHANICS' impulse response at the DC frequency so as to minimize the energy of the residual error. Hence, we may expect, through continuity arguments, that the low frequency range of the impulse response is also accurately modeled including $\sim$0.1 Hz which is the half-power bandwidth reflected by the gold standard τ_D.

We have demonstrated with the forward model that it is possible to tease out τ_D from long time scale information in an ABP waveform which is mostly corrupted on shorter time scales. However, the third-order systemic arterial compartment of the forward model provides only a first-order approximation of the distributed effects of the arterial tree. Consequently, it may not be reasonable, for example, to conclude that ten seconds of the ABP waveform are sufficient to estimate reliably τ_D from experimental data. Hence, it is important to evaluate the identification method against data generated from experimental data or data generated from a forward model which more accurately reflects the distributed effects of the systemic arterial tree (*e.g.*, [63]). The latter data may be necessary when considering the identification method in terms of estimating relative changes in TPR on short time scales (*e.g.*, $<$ 10 seconds) as there are no experimental means to measure such rapid changes directly.

Before we proceed with an assessment of the identification method against a preliminary set of experimental data, we propose another approach based on the identification method here for estimating the relative changes in TPR on short time scales which may be more accurate and computationally efficient than simply considering the analysis of short segments of the ABP waveform. The motivation here stems

from system identification applications. Consider, for example, the potential of this approach in regards to the direct identification method of Section 6.2.3.

Figure 7-3 Power spectrum of N''_{ABP} determined from the application of the identification method to the ABP waveform generated from the forward model with the third-order systemic arterial compartment in which $R_a(t)$ is varied sinusoidally at 0.05 Hz.

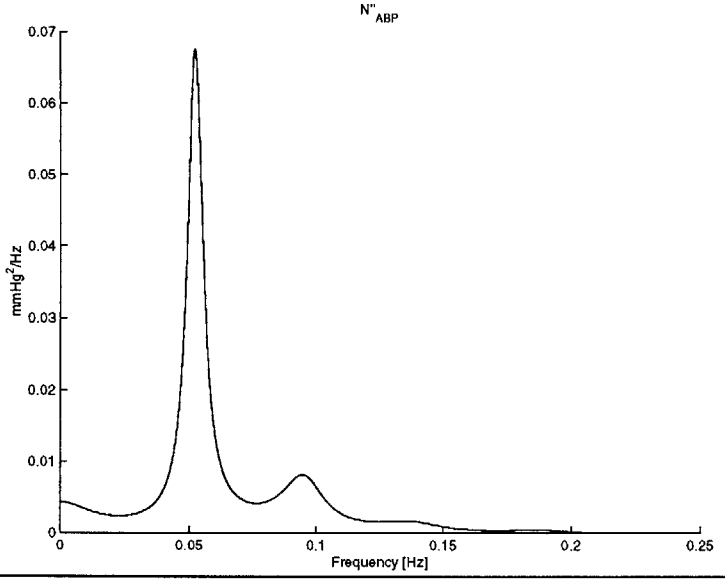

The method specifically considers the actual error resulting from the application of the identification method to long segments of the ABP waveform. From Equation (4.2), the actual error (N''_{ABP}) is defined as follows:

$$N''_{ABP}(t) = \sum_{i=1}^{m} a_i N''_{ABP}(t-i) + W'''_{ABP}(t). \tag{7.4}$$

Since PHR_{PP} essentially encompasses all the variability in ABP due to CO, we claim that the low frequency content (< 0.1 Hz) of N''_{ABP} represents ABP fluctuations due only to TPR fluctuations. This claim assumes that the arterial compliance and the systolic portion of each ABP wavelet is essentially constant over this frequency range. In order to test this claim, we introduced a sinusoidal variation to $R_a(t)$ at a frequency of 0.05 Hz (while all other mechanisms manipulating $R_a(t)$ were set to zero) in the forward model and computed the resulting power spectrum of N''_{ABP} (see Equation (4.28)) which is illustrated in Figure 7-3. The fact that most of the power

of the N''_{ABP} spectrum is centered at 0.05 Hz supports our claim. Now consider the block diagram in Figure 7-4 which is based on Equations (6.3) and (6.4). Based on this block diagram, it may be possible to recover the relative fluctuations in TPR by deconvolving the low frequency fluctuations in N''_{ABP} with $\frac{1}{\tau_D}e^{\frac{-t}{\tau_D}}$.

Figure 7-4 Block diagram depicting potential method for recovering relative fluctuations in TPR from N''_{ABP} and CIRCULATORY MECHANICS'.

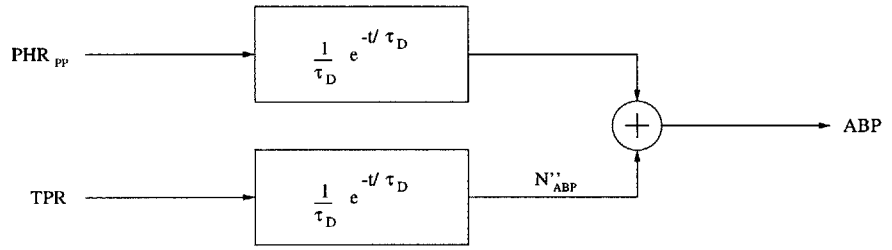

7.3 Experimental Data Analysis

In order to evaluate the performance of the identification method against experimental data, we must first establish a gold standard result. It may be somewhat difficult to obtain an independent, experimental measurement of τ_D; however, it is relatively easy to determine independently steady-state TPR through the ratio of mean ABP to mean CO. Hence, we evaluate the identification method against experimental data in terms of estimating steady-state, relative changes in TPR.

We first consider evaluation against a preliminary set of experimental data obtained from six intensive care patients. For each of the patients, an ABP waveform obtained from the insertion of a catheter in the radial artery and a CO measurement obtained from thermodilution are available for two different time periods in which the steady-state value of TPR has been altered. Figure 7-5 illustrates the estimated steady-state change in TPR as predicted by the identification method versus the gold standard steady-state change in TPR as determined by the ratio of mean ABP to CO. The results indicate a positive correlation (line of best fit: y = 0.8x+2.8) between the

Figure 7-5 Comparison of the estimated steady-state change in TPR as predicted by the identification method with the gold standard steady-state change in TPR as determined by the ratio of mean ABP to thermodilution CO for six intensive care patients (red x). The dashed red trace denotes the line of best fit, while the blue trace denotes the identity line.

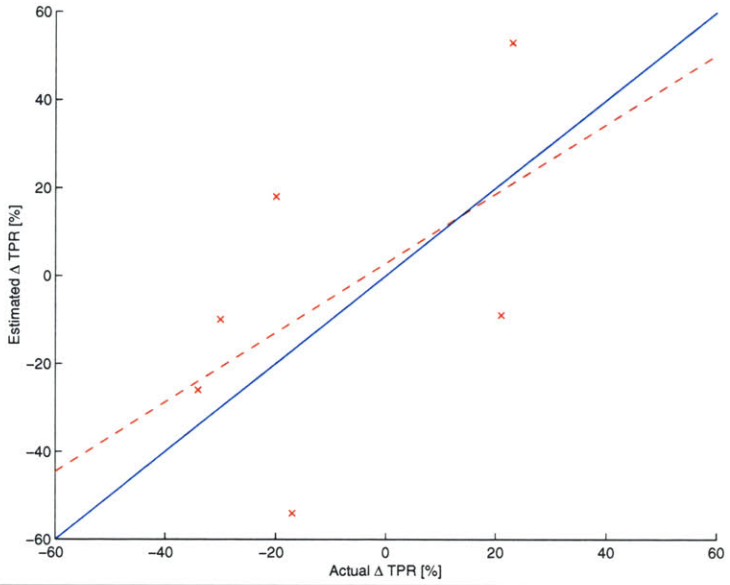

estimated and gold standard steady-state TPR change. Since the reliability of the measurement of mean CO through thermodilution is questionable, it is possible that much of the discrepancy here may be attributed to the imperfect gold standard.

Therefore, it is necessary to compare the identification method with data that includes the gold standard CO measurement which is obtained by applying a flowmeter to the aorta. Certainly, this measurement technique can only be considered for animals. Figure 7-6 illustrates such data obtained from a single dog in the control condition and after the administration of phenylephrine – a pharmacological vasoconstrictor which increases steady-state TPR. The ABP waveform here is obtained from the insertion of a catheter in the brachial artery, while CO is specifically obtained with an electromagnetic flowmeter applied to the aorta. Table 7.1 provides the results as determined from the gold standard and the identification method. The identification method not only compares quite favorably to the gold standard in terms of predicting the steady-state change in TPR due to the phenylephrine administration, but

Figure 7-6 Experimental ABP and CO data obtained from a single dog during control conditions and after the administration of phenylephrine. The ABP data is obtained from the insertion of a catheter in the brachial artery, while CO is obtained from an electromagnetic flowmeter applied to the aorta.

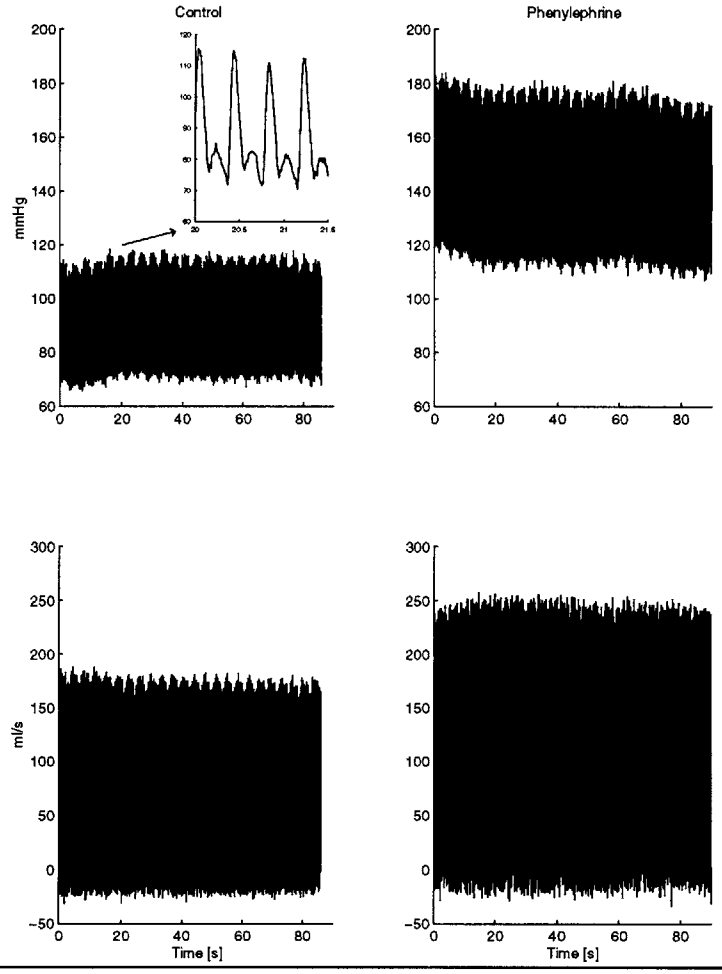

also provides values of τ_D which are consistent with those reported in the literature (*e.g.*, [12,46]). The promising preliminary results here, as well as in Section 7.2, motivate a full scale experimental study for the evaluation of the identification method in which the procedure outlined in Figure 7-6 is repeated for a large set of animals.

Method	First Data Segment	Second Data Segment	$\frac{\Delta TPR}{TPR}$
$\frac{\overline{ABP}}{\overline{CO}}$	2.4 $\frac{mmHg-s}{ml}$	2.8 $\frac{mmHg-s}{ml}$	+17%
τ_D	0.9±0.0 s	1.1±0.0 s	+22%

Table 7.1: Comparison between the estimated steady-state change in TPR as predicted by the identification method with the gold standard steady-state change in TPR as determined by the ratio of mean ABP to CO for the dog data in Figure 7-6.

Chapter 8

Conclusions

Cardiovascular system identification is a potentially powerful approach for intelligent patient monitoring of cardiovascular function. Rather than merely recording hemodynamic signals, the signals are mathematically analyzed so as to provide a dynamical characterization of the physiologic mechanisms responsible for generating them. The research presented in this thesis deals with the development and evaluation of practical cardiovascular system identification methods based on data generated by a forward model of the cardiovascular system whose dynamical properties are precisely known. In this chapter, we summarize the major results of this research (Section 8.1) and present potential future studies that stem from these results (Section 8.2).

8.1 Summary

In Part I (Chapters 2 and 3), we presented a computer model of the human cardiovascular system geared towards the accurate representation of those signals that are analyzed by the identification methods considered in Part II. The model includes three major components: a heart and circulation, a short-term regulatory system, and resting physiologic perturbations.

In Chapter 2, we described the heart and circulation which is a lumped parameter

model consisting of six compartments representing the left and right ventricles, the systemic arteries and veins, and the pulmonary arteries and veins. We demonstrated that this model is capable of reasonably emulating experimental data in terms of steady-state pulsatile, limiting static, and dynamical behaviors.

In Chapter 3, we presented models of the short-term regulatory system and resting physiologic perturbations. The short-term regulatory system consists of arterial and cardiopulmonary baroreflex systems as well as a direct neural coupling mechanism between respiration and heart rate. The arterial baroreflex system maintains arterial blood pressure (ABP) through the control of heart rate, contractility, total peripheral resistance (TPR), and systemic venous dead volume, while the cardiopulmonary baroreflex system senses the effective right atrial transmural pressure (RATP) of the heart and circulation and manipulates TPR and systemic venous tone. The resting physiologic perturbations include fixed-rate or random-interval respiratory activity, a stochastic disturbance to TPR reflecting autoregulation of local vascular beds, and a $1/f$ stochastic disturbance to heart rate representing variability not attributable to the arterial baroreflex system or respiration (*e.g.*, higher brain center activity). We demonstrated that these two models in concert with the heart and circulatory model emulate experimental hemodynamic variability at frequencies below the mean heart rate on short time scales of seconds to minutes.

In Part II (Chapters 4-7), we considered data generated from the forward model of Part I as a test bed for the evaluation of a previously developed cardiovascular system identification method and the development and analysis of novel, practical identification methods for quantifying the TPR baroreflex and monitoring steady-state changes in TPR. In Chapter 4, we described the data analysis techniques that are employed by these identification methods.

In Chapter 5, we evaluated the performance of the previously developed cardiovascular system identification method against forward model generated data. This

method involves the analysis of the fluctuations in heart rate, ABP, and instantaneous lung volume in order to characterize quantitatively two autonomically mediated coupling mechanisms, two mechanically mediated coupling mechanisms and two perturbing noise sources which are responsible for generating these fluctuations. Based on the forward model-based evaluation, we inferred that the cardiovascular system identification estimates obtained from experimental data are likely to reflect the actual system dynamics of underlying physiologic mechanisms and provide a very sensitive measure of parasympathetic function and a reasonably sensitive measure of β-sympathetic function.

In Chapter 6, we introduced two identification methods which require only left ventricular flow rate (cardiac output, CO) and ABP signals for the quantitative characterization of physiologic coupling mechanisms that reveal arterial and cardiopulmonary TPR baroreflex dynamics. The first method, referred to as the direct identification method, involves estimating TPR fluctuations from essentially the ratio of ABP to CO. The second method, referred to as the indirect identification method, involves extracting information pertaining to the TPR baroreflex essentially through its correlation with CO and ABP. We evaluated the performance of these two identification methods against forward model generated data. We found that the direct identification estimates were corrupted by a nonphysiologic relationship between the identification inputs and output imposed by the TPR estimation method. However, we found the indirect identification estimates to reveal useful information pertaining to TPR baroreflex dynamics. We also considered a complementary analysis of the two identification methods with respect to experimental human data. The estimates from this analysis appeared similar to those derived from forward model generated data. We therefore concluded that only the indirect identification estimates may truly reveal the TPR baroreflex.

In Chapter 7, we presented a novel method for monitoring steady-state changes

in TPR from only the ABP waveform. The method involves estimating the diastolic decay time constant from long time scale information in the ABP waveform via system identification. This method circumvents problems associated with measuring the time constant directly from the diastolic portion of an ABP wavelet (*e.g.*, pulse reflections corrupting peripheral ABP). We demonstrated that the method could accurately estimate the diastolic decay time constant from the ABP waveform generated from the forward model despite the presence of short time scale dynamics in the waveform emulating pulse reflections. We also included a preliminary investigation of the performance of the method in predicting steady-state changes in TPR against experimental data in which simultaneous measurements of CO and peripheral ABP were available. The results of this investigation were promising.

8.2 Future Studies

A principal motivating factor for the forward model-based analysis considered in this thesis is to initiate carefully thought out experimental studies which have a reasonable chance for success. We list the potential future studies that we consider to be most important as follows.

1. *Experimental validation of indirect TPR baroreflex identification method.* Although it would be very difficult to establish experimentally gold standard indirect identification step responses, the asymptotic step response values in terms of the static gains of the arterial and cardiopulmonary TPR baroreflexes may be obtained according to a relatively straightforward animal experiment described in [72]. The experiment involves perturbing mean ABP and mean RATP over a narrow range by varying ventricular pacing rate through a pacemaker and atrioventricular block and blood volume through hemorrhage or saline infusion. Provided that ABP, RATP, and CO are obtained from measurement, the static

gains may then be established from a multiple regression analysis in which mean ABP and mean RATP are regressed on mean TPR as determined from the ratio of mean ABP to mean CO. The CO and ABP signals required by the indirect identification method may be obtained prior to this experiment during conditions of sinus rhythm and normal blood volume while the animal is ventilated with a manual resuscitation bag according to the random-interval breathing protocol (see Section 3.3.1). Then, the asymptotic step response values estimated from the indirect identification method may be evaluated against their corresponding gold standard values. As discussed in Section 1.2, the experimental procedure proposed here assumes that the cardiovascular state and/or operating point has not been altered from one experimental condition to the next.

2. *Modification of indirect identification method to require only ABP.* Since a beat by beat CO measurement is not always available, it would be useful to develop a TPR baroreflex identification method that requires only ABP. It may be possible to modify the indirect identification method to require only ABP by considering the relative fluctuations in PP as a surrogate for relative fluctuations in SV. This modified indirect identification method may be most effectively and conveniently evaluated against experimental human data (see Section 6.5) by considering the estimates determined from the original indirect identification method as the gold standard.

3. *Validation of identification method for monitoring TPR from ABP waveform.* The ideal experimental protocol for evaluating the identification method in terms of monitoring steady-state TPR changes would require an animal preparation in which measurements of a peripheral ABP waveform and flowmeter CO are obtained before and after the administration of a pharmacologic inter-

vention that alters mean TPR. In a preliminary investigation, we evaluated the identification method based on data obtained from such an experiment protocol for a single dog (see Section 7.3). However, this protocol needs to be repeated for a larger set of animals. In Section 7.2, we described two potential methods for estimating TPR changes on relatively short time scales from the ABP waveform. Since it is not possible to measure directly TPR fluctuations, these two methods must be evaluated with respect to a forward model in which the distributed nature of the systemic arterial tree has been more accurately modeled. It may also be possible to modify the direct TPR baroreflex identification method to incorporate either of these time constant-based methods which would circumvent the problem related to estimating TPR fluctuations from essentially the ratio of ABP to CO. However, it is possible that systemic arterial compliance nonlinearity could preclude reliable direct identification. Note that this modification may also be conveniently evaluated against experimental human data (see Section 6.5) in which the static gains of the indirect identification estimates are considered to be the gold standards.

It is our hope that the research presented in this thesis stimulates the realization of such experimental validation studies and ultimately leads to the establishment of system identification as a clinical approach for intelligent patient monitoring of cardiovascular function.

Appendix A

Nonlinear Ventricular Pressure-Flow Rate Relationship

In this appendix, we present the pressure-flow rate relationship of the nonlinear, time-varying ventricular model in Section 2.2.3. This relationship is determined simply from the derivative of the pressure-volume relationships characterizing the nonlinear model with respect to time. However, the pressure-flow rate relationship that results from differentiation is quite involved and is thus included here.

We may rewrite the ventricular pressure-volume relationship in terms of normalized pressure ($y(t)$) and volume ($x(t)$) which is given in Section 2.2.3 as follows:

$$y(t) = \alpha(t)x(t) + \beta(t)\gamma(x(t), t), \tag{A.1}$$

where $\alpha(t)$ and $\beta(t)$ are defined in Equations (2.16) and (2.12) and

$$\gamma(x(t), t) = x(t) + \frac{1}{k}\ln\left\{\frac{a(x(t), t)}{b(t)}\right\}. \tag{A.2}$$

Note that we omit the subscripts l, r here and henceforth for the clarity. The functions $a(x(t), t)$ and $b(t)$ are defined as follows:

$$a(x(t), t) = 1 + \mathrm{e}^{-k(x(t)-x^0(t))}, \tag{A.3}$$

$$b(t) = 1 + \mathrm{e}^{kx^0(t)}. \tag{A.4}$$

Applying the product rule for differentiation to Equation (A.1) results in the following equation:

$$\frac{dy(t)}{dt} = \alpha(t)\frac{dx(t)}{dt} + \frac{d\alpha(t)}{dt}x(t) + \beta(t)\frac{d\gamma(x(t),t)}{dt} + \frac{d\beta(t)}{dt}\gamma(x(t),t), \tag{A.5}$$

where

$$\frac{dx(t)}{dt} = \frac{1}{Q^{max} - Q^o}\frac{dQ(t)}{dt} \tag{A.6}$$

$$\frac{d\alpha(t)}{dt} = \frac{Q^{max} - Q^0}{\Delta P^{max}}\frac{dE(t)}{dt} \tag{A.7}$$

$$\frac{d\gamma(x(t),t)}{dt} = \frac{dx(t)}{dt} + \frac{b(t)\frac{da(x(t),t)}{dt} - a(x(t),t)\frac{db(t)}{dt}}{ka(x(t),t)b(t)} \tag{A.8}$$

$$\frac{d\beta(t)}{dt} = \frac{-\frac{d\alpha(t)}{dt}\gamma(1,t) - (1-\alpha(t))\frac{d\gamma(1,t)}{dt}}{\gamma(1,t)^2}. \tag{A.9}$$

The derivatives in Equation (A.8) not previously defined are given as follows:

$$\frac{da(x(t),t)}{dt} = -k\left\{\frac{dx(t)}{dt} - \frac{dx^0(t)}{dt}\right\}\mathrm{e}^{-k(x(t)-x^0(t))} \tag{A.10}$$

$$\frac{db(t)}{dt} = k\frac{dx^0(t)}{dt}\mathrm{e}^{kx^0(t)}, \tag{A.11}$$

with

$$\frac{dx^0(t)}{dt} = \frac{-1}{(1+\alpha(t))^2}\frac{d\alpha(t)}{dt}. \tag{A.12}$$

The unnormalized pressure-flow rate relationship is then given as follows:

$$\frac{dP(t)}{dt} = \Delta P^{max}\frac{dy(t)}{dt} + \frac{dP_{th}(t)}{dt}. \tag{A.13}$$

By defining

$$f(Q(t) - Q^0, \frac{dQ(t)}{dt}, \frac{1}{E(t)}, \frac{dE(t)}{dt}, Q^{max} - Q^0, \Delta P^{max}) = \Delta P^{max}\frac{dy(t)}{dt}, \tag{A.14}$$

we may rewrite Equation (A.13) as follows:

$$\frac{dP(t)}{dt} = f(Q(t) - Q^0, \frac{dQ(t)}{dt}, \frac{1}{E(t)}, \frac{dE(t)}{dt}, Q^{max} - Q^0, \Delta P^{max}) + \frac{dP_{th}(t)}{dt}. \tag{A.15}$$

Appendix B

Estimation of τ_D

In this appendix, we describe the calculation for the mean and standard deviation of the τ_D estimate from the CIRCULATORY MECHANICS' impulse response estimate (see Section 7.1). Let $h(t)$ denote the mean of this impulse response estimate. Then, the mean τ_D estimate may be determined from the least squares fit of an exponential to $h(t)$ according to the following equation:

$$h(t) = Ae^{\frac{-t}{\tau_D}} + w(t) \quad 2 \leq t < 4, \tag{B.1}$$

where A and τ_D are parameters to be estimated by minimizing the energy of $w(t)$. This equation is nonlinear in its parameters and consequently, the minimization may only be achieved with a numerical search method. However, since $h(t) > 0$, we may log transform this equation as follows:

$$\ln(h(t)) = \ln(A) - \frac{t}{\tau_D} + e(t), \tag{B.2}$$

where $w(t)$ is assumed to be small with respect to $Ae^{\frac{-t}{\tau_D}}$. Now, by letting $\alpha = \frac{1}{\tau_D}$ and $\beta = \ln(A)$, the following equation results:

$$\ln(h(t)) = \beta - \alpha t + e(t), \tag{B.3}$$

where α and β are now the parameters to be estimated by minimizing the energy of $e(t)$. This equation is linear in its parameters, and the least squares solution may be

determined analytically. To this end, we rewrite Equation (B.3) in vector product form as follows:

$$\ln(h(t)) = \phi^T(t)\theta + e(t), \tag{B.4}$$

where

$$\phi^T(t) = [1 \quad -t] \tag{B.5}$$

$$\theta^T = [\beta \quad \alpha]. \tag{B.6}$$

Then, from Equation (4.14), the least squares solution ($\hat{\theta}$) here is given as follows:

$$\hat{\theta} = \left\{ \sum_t \phi(t)\,\phi^T(t) \right\}^{-1} \sum_t \phi(t) \ln(h(t)), \tag{B.7}$$

with the mean of the τ_D estimate equal to $\frac{1}{\hat{\theta}(2)}$.

We now derive the standard deviation of the τ_D estimate as follows. Suppose $h(t)$ is perturbed by a small quantity $\Delta h(t)$. Then, according to a Taylor series approximation, we may rewrite Equation (B.7) as follows:

$$\hat{\theta} = \left\{ \sum_t \phi(t)\,\phi^T(t) \right\}^{-1} \sum_t \phi(t) \left\{ \ln(h(t)) + \frac{\Delta h(t)}{h(t)} \right\}. \tag{B.8}$$

Now, assume that the true solution to Equation (B.4) is given by $\theta = \theta_0$ and the resulting error ($e_0(t)$) is a zero-mean, white noise process with standard deviation σ_e which may be determined as follows:

$$e_0(t) = \ln(h(t)) - \phi^T(t)\theta_0. \tag{B.9}$$

Then, after substituting this equation into Equation (B.8) and rearranging terms, the following equation results:

$$\hat{\theta} - \theta_0 = \left\{ \sum_t \phi(t)\,\phi^T(t) \right\}^{-1} \sum_t \phi(t) \left\{ e_0(t) + \frac{\Delta h(t)}{h(t)} \right\}. \tag{B.10}$$

Assuming that $e_0(t)$ is orthogonal to $\frac{\Delta h(t)}{h(t)}$, the covariance matrix of this vector may be given as follows:

$$\begin{aligned}\Lambda_\theta &= E(\hat{\theta}-\theta_0)(\hat{\theta}-\theta_0)^T \qquad \text{(B.11)}\\ &= \left\{\sum_t \phi(t)\,\phi^T(t)\right\}^{-1} \sum_t \sum_s \phi(t)\frac{E(\Delta h(t)\Delta h(s))}{h(t)h(s)}\phi(s)^T \left\{\sum_t \phi(t)\,\phi^T(t)\right\}^{-1}\\ &+ \sigma_e^2 \left\{\sum_t \phi(t)\,\phi^T(t)\right\}^{-1},\end{aligned}$$

where $E(\cdot)$ denotes the expectation operator. This equation indicates that the uncertainty in the τ_{D} estimate is due to the uncertainty in the CIRCULATORY MECHANICS' impulse response estimate and the uncertainty in the exponential fit. From another Taylor series approximation, $\Delta\tau_D \approx \frac{-\Delta\alpha}{\alpha^2}$. Hence, the standard deviation of the τ_{D} estimate may be given by $\frac{1}{\alpha^2}\sqrt{\Lambda_\theta(2,2)}$. Note that $E(\Delta h(t)\Delta h(s))$ may be determined from the covariance matrix of $h(t)$ (see Section 4.2.2), while σ_e may be estimated from the standard deviation of the process obtained by substituting $\hat{\theta}$ for θ_0 in Equation (B.9).

Bibliography

[1] Solange Akselrod, David Gordon, Jeffrey B. Madwed, Nancy C. Snidman, Daniel C. Shannon, and Richard J. Cohen. Hemodynamic regulation: Investigation by spectral analysis. *American Journal of Physiology*, 249(18):H867–H875, 1985.

[2] Solange Akselrod, David Gordon, F. Andrew Ubel, Daniel C. Shannon, A. Clifford Barger, and Richard J. Cohen. Power spectrum analysis of heart rate fluctuation: A quantitative probe of beat-to-beat cardiovascular control. *Science*, 213:220–222, 1981.

[3] Marvin L. Appel. Closed loop identification of cardiovascular regulatory mechanisms, June 1992.

[4] Marvin L. Appel, Ronald D. Berger, J. Phillip Saul, Joseph M. Smith, and Richard J. Cohen. Beat-to-beat variability in cardiovascular variables: Noise or music? *Journal of American College of Cardiology*, 14:1139–1148, 1989.

[5] J. E. W. Beneken and B. Dewit. A physical approach to hemodynamic aspects of the human cardiovascular system. In E. B. Reeve and Arthur C. Guyton, editors, *Physical Bases of Circulatory Transport: Regulation and Exchange*, pages 1–45, Philadelphia, PA, 1967. W. B. Saunders Company.

[6] Ronald D. Berger. Analysis of the cardiovascular control system using broadband stimulation, June 1987.

[7] Ronald D. Berger, J. Phillip Saul, and Richard J. Cohen. An efficient algorithm for spectra analysis of heart rate variability. *IEEE Transactions in Biomedical Engineering*, 33(9):900–904, 1986.

[8] Ronald D. Berger, J. Phillip Saul, and Richard J. Cohen. Assessment of autonomic response by broad-band respiration. *IEEE Transactions in Biomedical Engineering*, 36(11):1061–1065, 1989.

[9] Ronald D. Berger, J. Phillip Saul, and Richard J. Cohen. Transfer function analysis of autonomic regulation i. canine atrial rate response. *American Journal of Physiology*, 256(25):H142–H152, 1989.

[10] Robert M. Berne and Matthew N. Levy. *Cardiovascular Physiology.* The C. V. Mosby Company, St. Louis, MO, 1986.

[11] R. Beyar, Y. Kishon, S. Sideman, and U. Dinnar. Computer studies of systemic and regional blood flow mechanisms during cardiopulmonary resuscitation. *Medical and Biological Engineering and Computing*, 22:499–506, 1984.

[12] Maurice J. Bourgeois, Barry K. Gilbert, D. E. Donald, and Earl H. Wood. Characteristics of aortic diastolic pressure decay with application to the continuous monitoring of changes in peripheral resistance. *Circulation Research*, 35:56–66, 1974.

[13] R. Burattini, G. Gnudi, N. Westerhof, and s. Fioretti. Total systemic arterial compliance and aortic characteristic impedance in the dog as a function of pressure: A model based study. *Computers and Biomedical Research*, 20:154–165, 1987.

[14] D. Burkhoff, S. Sugiura, D.T. Yue, and K. Sagawa. Contractility-dependent curvilinearity of end-systolic pressure-volume relations. *American Journal of Physiology*, 252:H1218–H1227, 1987.

[15] G. Cevenini, P. Barbini, A. Cappello, and G. Avanzolini. Three-element model for total systemic circulation: Emphasis on the accuracy of parameter estimates. *Journal of Biomedical Engineering*, 9(4):374–378, 1987.

[16] Ki H. Chon, Ramakrishna Mukkamala, Karin Toska, Thomas J. Mullen, Antonis A. Armoundas, and Richard J. Cohen. Linear and nonlinear system identification of autonomic heart-rate modulation. *IEEE Engineering in Medicine and Biology*, pages 96–105, September/October 1997.

[17] Ki H. Chon, Thomas J. Mullen, and Richard J. Cohen. A dual-input nonlinear system analysis of autonomic modulation of heart rate. *IEEE Transactions on Biomedical Engineering*, 43:530–544, 1996.

[18] Kevin Patrick Clark. Extracting new information from the shape of the blood pressure pulse. Master's thesis, Massachusetts Institute of Technology, Cambridge, MA 02139, February 1990.

[19] B. F. Clarke, D. J. Ewing, and I. W. Campbell. Diabetic autonomic neuropathy. *Diabetologia*, 17:195–212, 1979.

[20] Richard J. Cohen. Cardiac mechanics. MIT HST 090 Course Notes.

[21] Giovanni Corsini and Roberto Saletti. Design of a digital $1/f^{\gamma}$ noise simulator. In *Noise in Physical Systems and* $1/f$ *Noise*, pages 82–86, Singapore, 1987.

[22] E. C. Cross, P. A. Rieben, and P. F. Salisbury. Influence of coronary perfusion and myocardial edema on pressure-volume diagram of left ventricle. *American Journal of Physiology*, 201:102–108, 1961.

[23] Timothy L. Davis. Teaching physiology through interactive simulation of hemodynamics. Master's thesis, Massachusetts Institute of Technology, Cambridge, MA 02139, February 1991.

[24] Roelf Willem de Boer. Beat-to-beat blood-pressure fluctuations and heart-rate variability in man: Physiological relationships, analysis techniques and a simple model, November 1985.

[25] Tushar H. Desai, Jerry C. Collins, Marie Snell, and Rogelio Mosqueda-Garcia. Modeling of arterial and cardiopulmonary baroreflex control of heart rate. *American Journal of Physiology*, 272(41):H2343–H2352, 1997.

[26] B. Deswysen, A. A. Charlier, and M. Gevers. Quantitative evaluation of the systemic arterial bed by parameter estimation of a simple model. *Medical and Biological Engineering and Computing*, 18:153–166, 1980.

[27] G. Diamond, J. S. Forrester, J. Hargis, W. W. Parmley, R. Danzig, and J. J. C. Swan. Diastolic pressure-volume relationship in the canine left ventricle. *Circulation Research*, 29:267–275, 1971.

[28] Alvin W. Drake. *Fundamentals of Applied Probability Theory.* McGraw Hill, Inc., New York, 1988.

[29] Morten Eriksen and Lars Walloe. Improved method for cardiac output determination in man using ultrasound doppler technique. *Medical and Biological Engineering and Computing*, 28:555–560, 1990.

[30] R. Fogliardi, M. Di Donfrancesco, and R. Burattini. Comparison of linear and nonlinear formulations of the three-element windkessel model. *American Journal of Physiology*, 271(6):H2661–2668, 1996.

[31] Arthur C. Guyton, Thomas G. Coleman, and H. J. Granger. Circulation: Overall regulation. *Annual Review of Physiology*, 34:13–46, 1972.

[32] Arthur C. Guyton and John E. Hall. *Textbook of Medical Physiology.* W. B. Saunders Company, Philadelphia, 1996.

[33] Arthur C. Guyton, Arthur W. Lindsey, Berry Abernathy, and Travis Richardson. Venous return at various right atrial pressures and the normal venous return curve. *American Journal of Physiology*, 189(3):809–815, 1957.

[34] P Hallock and I. C. Benson. *Journal of Clinical Investigation*, 16:595, 1937.

[35] Thomas Heldt, Eun B. Shim, Roger D. Kamm, and Roger G. Mark. Computational model of the cardiovascular system and its response to orthostatic stress. In Preparation.

[36] Caleb W. Herndon and Kiichi Sagawa. Combined effects of aortic and right atrial pressures on aortic flow. *American Journal of Physiology*, 217(1):65–72, 1969.

[37] B. W. Hyndman, R. I. Kitney, and B. McA. Sayers. Spontaneous rhythms in physiologic control systems. *Nature*, 233:339–341, 1971.

[38] Ben P. M. Imholz, Wouter Wieling, Gert A. van Montfrans, and Karel H. Wesseling. Fifteen years experience with finger arterial pressure monitoring: Assessment of the technology. *Cardiovascular Research*, 38:605–616, 1998.

[39] J. M. Johnson, L. B. Rowell, M. Niederberger, and M. M. Eisman. Human splanchnic and forearm vasoconstrictor responses to reductions of right atrial and aortic pressures. *Circulation Research*, 34:515–524, 1974.

[40] J. Thomas Bigger Jr, Richard C. Steinman, Linda M. Rolnitzky, Joseph L. Fleiss, Paul Albrecht, and Richard J. Cohen. Power law behavior of rr-interval variability in healthy middle-aged persons, patients with recent acute myocardial infarction, and patients with heart transplants. *Circulation*, 93:2142–2151, 1996.

[41] David A. Kass, Rafael Beyar, Edward Lankford, Maurice Heard, W. Lowell Maughan, and Kiichi Sagawa. Influence of contractile state on curvilinearity of in situ end-systolic pressure-volume relations. *Circulation*, 79(1):167–178, 1989.

[42] Marvin S. Keshner. $1/f$ noise. *Proceedings of the IEEE*, 70(3):212–218, 1982.

[43] R. I. Kitney. Entrainment of the human rr interval by thermal stimuli. *Journal of Physiology*, 252:37–38, 1975.

[44] M. Kobayashi and T. Musha. 1/f fluctuation of heartbeat period. *IEEE Transactions on Biomedical Engineering*, 29(6):456–457, 1982.

[45] Christian J. Lambertsen. Physical and mechanical aspects of respiration. In Vernon B. Mountcastle, editor, *Medical Physiology*, pages 1361–1371, St. Louis, MO, 1974. The C. V. Mosby Company.

[46] John K.-J. Li, Ting Cui, and Gary M. Drzewiecki. A nonlinear model of the arterial system incorporating a pressure-dependent compliance. *IEEE Transactions on Biomedical Engineering*, 37(7):673–678, 1990.

[47] Lennart Ljung. *System Identification: Theory for the User*. PTR Prentice Hall, Englewood Cliffs, NJ, 1987.

[48] K. Lossius, M Eriksen, and L Walloe. Thermoregulatory fluctuations in heart rate and blood pressure in humans: Effect of cooling and parasympathetic blockade. *Journal of the Autonomic Nervous System*, 47(3):245–254, 1994.

[49] Jeffrey B. Madwed, Paul Albrecht, Roger G. Mark, and Richard J. Cohen. Low-frequency oscillations in arterial pressure and heart rate: a simple computer model. *American Journal of Physiology*, 256(25):H1573–H1579, 1989.

[50] Jeffrey B. Madwed and Richard J. Cohen. Heart rate response to hemorrhage-induced 0.05 hz oscillation in arterial pressure in conscious dogs. *American Journal of Physiology*, 260(29):H1248–H1253, 1991.

[51] Guiseppe Mancia and Allyn L. Mark. Arterial baroreflexes in humans. In *Handbook of Physiology, Section 2: The Cardiovascular System, Vol. III, Part 2*, pages 755–793, Bethesda, MD, 1983. American Physiological Society.

[52] Allyn L. Mark and Giuseppe Mancia. Cardiopulmonary baroreflexes in humans. In *Handbook of Physiology, Section 2: The Cardiovascular System, Vol. III, Part 2*, pages 795–813, Bethesda, MD, 1983. American Physiological Society.

[53] Lawrence S. Marple. *Digital Spectral Analysis: with Applications.* Prentice-Hall, Englewood Cliffs, NJ, 1987.

[54] W. L. Maughan and David A. Kass. The use of the pressure-volume diagram for measuring ventricular pump function. *Automedica*, 11:317–342, 1989.

[55] Francois M. Melchior, R. Srini Srinivasan, and John B. Charles. Mathematical modeling of human cardiovascular system for simulation of orthostatic response. *American Journal of Physiology*, 262(31):H1920–H1933, 1992.

[56] Ramakrishna Mukkamala. Closed-loop system identification of cardiovascular control mechanisms in diabetic autonomic neuropathy. Master's thesis, Massachusetts Institute of Technology, Cambridge, MA 02139, June 1995.

[57] Ramakrishna Mukkamala, Joanne M. Mathias, Thomas J. Mullen, Richard J. Cohen, and Roy Freeman. System identification of closed-loop cardiovascular control mechanisms: Diabetic autonomic neuropathy. *American Journal of Physiology*, 276:R905–R912, 1999.

[58] Thomas J. Mullen. A system identification approach to characterizing intermediate term hemodynamic variability, February 1998.

[59] Thomas J. Mullen, Marvin L. Appel, Ramakrishna Mukkamala, Joanne M. Mathias, and Richard J. Cohen. System identification of closed-loop cardio-

vascular control: Effects of posture and autonomic blockade. *American Journal of Physiology*, 272:H448–H461, 1997.

[60] Abraham Noordergraaf. *Circulatory System Dynamics.* Academic Press, New York, 1978.

[61] Task Force of the European Society of Cardiology, the North American Society of Pacing, and Electrophysiology. Heart rate variability: Standards of measurement, physiological interpretation, and clinical use. *Circulation*, 93:1043–1065, 1996.

[62] Alan V. Oppenheim and Ronald W. Schafer. *Discrete-Time Signal Processing.* Prentice Hall, Englewood Cliffs, NJ, 1989.

[63] Edwin T. Ozawa. A numerical model of the cardiovascular system for clinical assessment of the hemodynamic state, February 1996.

[64] James A. Pawelczyk and Peter B. Raven. Reductions in central venous pressure improve carotid baroreflex responses in conscious men. *American Journal of Physiology*, 257(26):H1389–H1895, 1989.

[65] S. Permutt, B. Bromberger-Barnea, and H. N. Bane. Alveolar pressure, pulmonary venous pressure, and the vascular waterfall. *Medical Thoracalis*, 19:239–260, 1962.

[66] S. Permutt and R. L. Riley. Hemodynamics of collapsible vessels with tone: the vascular waterfall. *Journal of Applied Physiology*, 18(5):924–932, 1963.

[67] Michael H. Perrott and Richard J. Cohen. An efficient approach to arma modeling of biological systems with multiple inputs and delays. *IEEE Transactions on Biomedical Engineering*, 43(1):1–14, 1996.

[68] Bruce Pomeranz, Robert J. B. Macaulay, Margaret A. Caudill, Ilan Kutz, Daniel C. Shannon, Richard J. Cohen, and Herbert Benson. Assessment of autonomic function in humans by heart rate spectral analysis. *American Journal of Physiology*, 248(17):H151–H153, 1985.

[69] William H. Press, Brian P. Flannery, Saul A. Teukolsky, and William T. Vetterling. *Numerical Recipes in C: The Art of Scientific Computing.* Cambridge University Press, New York, 1992.

[70] E. Raaijmakers, T. J. Faes, R. J. Scholten, H. G. Goovaerts, and R. M. Heethaar. A meta-analysis of published studies concerning the validity of thoracic impedance cardiography. *Annals of the New York Academy of Sciences*, 873:121–127, 1999.

[71] Craig D. Ramsdell, Grete H. Sundby, Derin Sherman, Ming Maa, Jacquelyn L. Baskin, Gordon H. Williams, and Richard J. Cohen. Non-invasive assessment of alterations in cardiovascular regulation and function and susceptibility to ventricular arrhythmias resulting from microgravity exposure. In M. S. El-Genk, editor, *Space Technology and Applications International Forum-2000*, pages 281–294. 2000 American Institute of Physics, 2000.

[72] Henry Raymundo, Allen M. Scher, Donal S. O'Leary, and Paul D. Sampson. Cardiovascular control by arterial and cardiopulmonary baroreceptors in awake dogs with atrioventricular block. *American Journal of Physiology*, 257(26):H2048–H2058, 1989.

[73] Kiichi Sagawa. Comparative models of overall circulatory mechanics. In *Advances in Biomedical Engineering*, volume 3, pages 1–95, New York, 1973. Academic Press.

[74] Roberto Saletti. A comparison between two methods to generate $1/f^{\gamma}$ noise. *Proceedings of the IEEE*, 74(11):1595–1596, 1986.

[75] J. Philip Saul, Ronald D. Berger, Paul Albrecht, , Stephen P. Stein, Ming Hui Chen, and Richard J. Cohen. Transfer function analysis of the circulation: Unique insights into cardiovascular regulation. *American Journal of Physiology*, 261(30):H1231–H1245, 1991.

[76] J. Philip Saul, Ronald D. Berger, Ming Hui Chen, and Richard J. Cohen. Transfer function analysis of autonomic regulation ii. respiratory sinus arrhythmia. *American Journal of Physiology*, 256(25):H153–H161, 1989.

[77] J. Phillip Saul, Paul Albrecht, Ronald D. Berger, and Richard J. Cohen. Analysis of long-term heart rate variability: Methods, 1/f scaling and implications. In *Computers in Cardiology*, pages 419–422, Silver Spring, MD, 1987. IEEE Computer Society Press.

[78] Robert M. Schmidt, Manoru Kumada, and Kiichi Sagawa. Cardiac output and total peripheral resistance in carotid sinus reflex. *American Journal of Physiology*, 221(2):480–487, 1971.

[79] Torsten Soderstrom and Petre Stoica. *System Identification.* Prentice Hall, Englewood Cliffs, NJ, 1989.

[80] Hiroyuki Suga and Kiichi Sagawa. Instantaneous pressure-volume relationships and their ratio in the excised, supported canine left ventricle. *Circulation Research*, 35:117–126, 1974.

[81] Hiroyuki Suga, Kiichi Sagawa, and Artin A. Shoukas. Load independence of the instantaneous pressure-volume ratio of the canine left ventricle and effects of epinephrine and heart rate on the ratio. *Circulation Research*, 32:314–322, 1973.

[82] Hiroyuki Suga, Osamu Yamada, Yoichi Goto, and Yiuchiro Igarashi. Peak isovolumic pressure-volume relation of puppy left ventricle. *American Journal of Physiology*, 250(19):H167–H172, 1986.

[83] John K. Triedman, Michael H. Perrott, Richard J. Cohen, and J. Philip Saul. Respiratory sinus arrhythmia: Time domain characterization using autoregressive moving average analysis. *American Journal of Physiology*, 268(37):H2232–H2238, 1995.

[84] Mauro Ursino. Interaction between carotid baroregulation and the pulsating heart: A mathematical model. *American Journal of Physiology*, 275(44):H1733–H1747, 1998.

[85] Arthur J. Vander, James H. Sherman, and Dorothy S. Luciano. *Human Physiology*. McGraw Hill, Inc., New York, 1994.

[86] Ronald G. Victor and Allyn L. Mark. Interaction of cardiopulmonary and carotid baroreflex control of vascular resistance in humans. *Journal of Clinical Investigation*, 76:1592–1598, 1985.

[87] P.E. Wellstead and J.M. Edmunds. Least-squares identification of closed-loop systems. *International Journal of Control*, 21(4):689–699, 1975.